Molecular Orientation at Biological Interfaces

Water and lipids studied
through surface-specific vibrational spectroscopy

ACADEMISCH PROEFSCHRIFT

ter verkrijging van de graad van doctor
aan de Universiteit van Amsterdam
op gezag van de Rector Magnificus
prof. dr. D. C. van den Boom
ten overstaan van een door het college voor promoties
ingestelde commissie,
in het openbaar te verdedigen in de Agnietenkapel
op vrijdag 28 juni 2013, te 10:00 uur

door

Ruben Eric Pool

geboren te Amstelveen

Cover picture: Amazon rainforest, Suriname

PUBLICATIONS COVERED IN THIS THESIS

R. E. Pool, J. Versluis, E. H. G. Backus and M. Bonn. Comparative Study of Direct and Phase-Specific Vibrational Sum-Frequency Generation Spectroscopy: Advantages and Limitations. *J. Phys. Chem. B 115*, 15362 (2011).

R. E. Pool*, Y. Nagata*, E. H. G. Backus and M. Bonn. Nuclear Quantum Effects Affect Bond Orientation of Water at the Water-Vapor Interface. *Phys. Rev. Lett. 109*, 226101 (2012).

R. E. Pool, L. M. A. Driessen and M. Bonn. . A Molecular View of the Interaction of Carbon Nanotubes with Lipid Membranes *Submitted*.

R. E. Pool, Y. Nagata, E. H. G. Backus, J. M. Ruysschaert and M. Bonn. Ordered Water around Zwitterionic Lipids: Vibrational Sum-Frequency Generation Spectroscopy of Stepwise Methylation of the Phospholipid Head Group. *In preparation*.

R. E. Pool, R. K. Campen and M. Bonn. Charged Nanoparticles induce Reorganization of Lipids and the Surrounding Water. *In preparation*.

CONTENTS

1   INTRODUCTION

1.1   THE DEVELOPMENT OF MODERN SPECTROSCOPY

The primary goal of science is the exploration of the frontiers of our knowledge. By enlarging the domain of what we know and understand we hope to obtain more tools to solve practical and philosophical problems, or simply satisfy our curiosity. The boundaries shift, but never disappear; there is always more to explore. These boundaries of what is known to us can be seen as barriers that deny us direct observation of what lies beyond. One of these barriers, one which has been relevant for as long as people have had scientific interest, is the barrier of size.

As human beings, we have always had difficulty observing and understanding things that exceed the scale of our own size by too far. In everyday life, this does not pose any problem. It is often said that our senses deceive us, since they cannot truthfully teach us all about the physical world. In fact, this limitation is a desirable and logical consequence of the optimal adaptation of our body to its living environment through evolution. However, our species uniquely has the cognitive tools to imagine scenarios beyond direct observation, and herein lies the source of our scientific interest. We cannot help but wonder what reality exists beyond the limited hints that we are granted of the nature of atoms, molecules, stars, and universes. Still, we must rely on observations to test the hypotheses we formulate and satisfy our curiosity. But how can we see what is too small, too large or too complex for our senses to perceive? The answer is that we use a combination of our senses and our intellect to learn about the external world by means of indirect observations.

In this thesis we focus on particles and structures that are too small to observe with the naked eye. This frontier of size was first crossed with the development of microscopes in the 17th century. In microscopy, the only intermediate step between object and image is a linear magnification M. When interpreting the data, the only rational step that needs to be taken is the realization that the actual object is a factor M smaller than the perceived image. At the end of the 19th century, the age of modern physics was introduced by James Clerk Maxwell, who combined and refined the knowledge on electricity and magnetism in his 1873 textbook *A Treatise on Electricity and Magnetism.* He first described the origins and behavior of electromagnetic radiation, and realized that visible light, too, is an electromagnetic wave. Figure 1.1 shows that visible light comprises only a tiny part of the full electromagnetic spectrum. This, again, is an example of our senses having evolved to match our everyday environment: the range of light that is visible to us, of wavelengths between 400

and 700 nm, corresponds to the maximum intensity of the emission spectrum of the sun.

The wave nature of light was soon questioned when it failed to describe black body radiation, the emission spectrum of a perfectly emitting physical body. A correct description was postulated around 1900 by Max Planck, who predicted that light could only exist in certain quantities of energy, i.e. that electromagnetic radiation is quantized. Although he may not have foreseen the implications of his work and at first even saw his postulate as "a purely formal assumption", it laid the foundation for the development of quantum mechanics. The particle behavior of light was further proven experimentally by Albert Einstein in his description of the photoelectric effect. He showed that emission of electrons occurred only if light had a minimum frequency. This finding implies that it is not the total energy of the radiation that matters, but rather the energy of the quantized light packages, the photons. Soon, the physics community accepted that some phenomena of light should be explained by treating it as a wave, while others can only be understood in terms of photons. This particle-wave duality persists to this day, and has been shown to exist not only for light, but for anything that can be treated as either a particle or a wave.
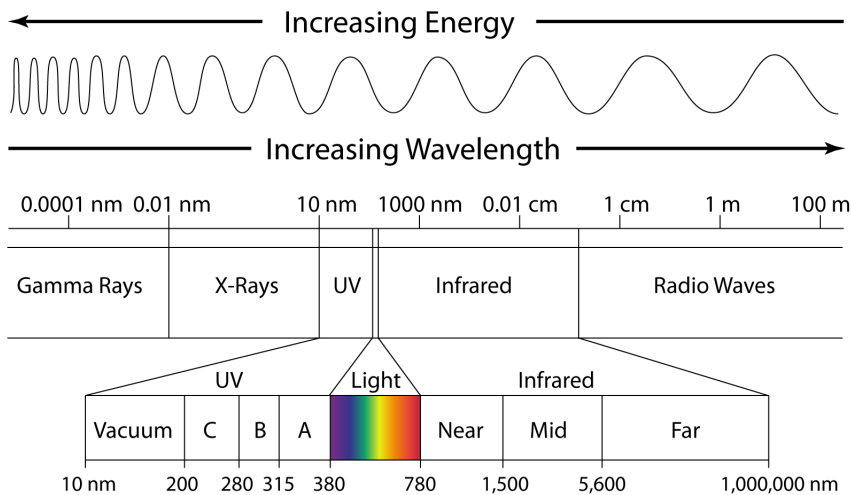
FIGURE 1.1. The electromagnetic spectrum. Visible light only comprises a tiny fraction of the known spectrum [1].

During the same time that Max Planck and Albert Einstein discovered that electromagnetic radiation could only exist in quantized form, the American physicist William Coblentz studied the absorption of infrared (IR) radiation by various materials. It had longer been known that many chemicals displayed sharp and distinct absorption lines in the IR region, which means that they

absorbed electromagnetic radiation of lower frequencies than visible light only at specific, well-defined frequencies. By measuring a range of materials and meticulously documenting the absorption spectra, Coblentz was the first to provide convincing evidence that the absorption lines belonged to specific chemical groups. Although at the time they may not have been given their due appreciation, the implications of this discovery were tremendous. Now, details of the structure of an unknown substance could be revealed by means of their spectral signature. In other words, the physical and chemical properties of the material could now be revealed systematically and on a submicroscopic scale. The rational step that we need to take to deduce object properties from observables is not as simple as a linear magnification anymore: to understand the origins of the spectrum we must at least have a reference spectrum to know what frequencies belong to which chemical structures, and preferably also a theoretical understanding of the physics behind absorption and emission of radiation.

infrared excitation

symmetric stretch   asymmetric stretch   bend
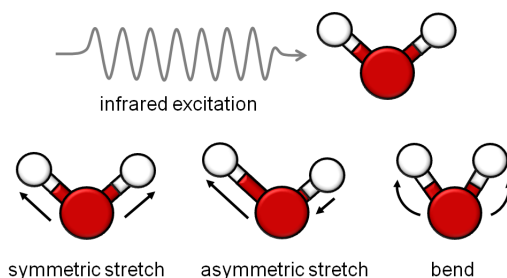
FIGURE 1.2. The three vibrational modes of the water molecule, H_2O. Depending on its frequency, absorption of an IR photon may induce a stretch or bend vibration.

This understanding was obtained in the course of the 20th century, when the theoretical framework of quantum mechanics was developed. Quantum mechanics describes how quantization of energy is not only true for radiation (in photons), but also for the energy states of atoms and molecules. For atoms, these quantum states largely correspond to electronic transitions, meaning that they match the energy needed to put an electron in the next spin-orbit state. For molecules, these molecular energy states are dominated by both the electronic states and the energies of the possible vibrational modes between the atoms of the molecule. Both for atomic and molecular quantum states, a transition to another state may occur by absorption or emission of a photon that matches the energy difference between the initial and final state. Photons matching the electronic transition typically have energies in the visible region of the electromagnetic spectrum, while photons matching the fundamental vibrational transitions are mid-IR, with wavelengths between 2.5 and 25 μm, although overtones and bending modes may lie outside this range. Figure 1.2 schematically shows the possible vibrations of the water molecule.

Skipping ahead to the early 1960s, the development of LASER (light amplification by stimulated emission of radiation) technology revolutionized the field of spectroscopy. Now so commonly known that the abbreviation is used as a

noun, the laser enabled the development of many optical techniques. All key characteristics of laser light coherence, well-defined frequency and high intensity greatly increased the possibilities of spectroscopic research. For the first time, physicists were able to explore the field of nonlinear optics.

1.2 SECOND HARMONIC GENERATION AND SUM-FREQUENCY GENERATION

In 1961, shortly after the invention of the laser, scientists of the University of Michigan demonstrated a curious new phenomenon. When sending a 694 nm laser beam through a quartz crystal, a spectrometer on the other side displayed not only this frequency, but also a much fainter spot at 347 nm, half the wavelength of the original light [2]. For the first time, a two-photon process was recorded: at high intensities of coherent light, the energy of two identical photons may be combined into a new photon of double the energy. This process is called second-harmonic generation (SHG), in analogy to overtone generation in acoustics.

In the decades after its discovery, SHG was shown to occur in many different materials with a quasi-crystalline structure, ranging from cat retinal cells to carbohydrates to glass fibers [3–12]. The reason why such chemically diverse materials are all SHG active, is that in many crystal-like structures a strong nonresonant response can be induced, provided that symmetry is broken on both molecular and macroscopic scales. A more thorough mathematical description is presented in chapter 2. Thus, an isotropic bulk medium is not SHG active, but the interface between two such media is, as long as the interfacial molecules are not centrosymmetric themselves. This property of SHG makes it a powerful tool for interface-specific spectroscopy. The often distinct optical properties of surfaces and interfaces can then be probed with a specificity of only a few molecular layers [13]. In contrast, linear spectroscopic methods do not distinguish between bulk and interface, causing the interfacial signal to be lost in the generally much larger bulk signal. Another advantage of SHG spectroscopy is that it is background free: the SHG signal is of a frequency that is not present in the excitation beam, effectively suppressing the background noise.

When applying SHG spectroscopy nonresonantly, the information that can be gained is limited: the magnitude of the signal tells us something about the symmetry of the system, but there are no line shapes present to reveal signatures of the chemical structure. When applying SHG resonantly, the detected signal is twice the frequency of the resonance. For vibrational spectroscopy, the resulting SHG signal is typically near-IR, a spectral region for which detectors are inefficient. With linear vibrational (absorption) spectroscopy this loss is acceptable because signal intensities are high. But for the low second-order SHG signal, it may easily result in a signal-to-noise ratio (SNR) that is problematically low. This technical limitation can be overcome by using a different two-photon process, in which we combine two photons of different energies rather than two

identical ones. This kind of nonlinear process is called sum-frequency generation spectroscopy (SFG). SFG can be seen as a generalized form of SHG in which the summed frequencies do not need to be equal. The first laser can be tuned to be on resonance with a vibration at the sample surface, while the second has a nonresonant frequency, upconverting the resonant signal to a higher energy.

In figure 1.3 the energy diagrams of IR absorption, SHG and SFG are shown. A vibrational mode of a molecule is said to be IR active when it can be excited by IR radiation. Illumination with photons of an energy matching the transition is not sufficient: the criterion for IR activity is that excitation of the mode induces a change in the molecular dipole moment. For carbon dioxide (CO_2) for instance, the symmetric stretch vibration does not change the direction of the dipole because of its linearity and symmetry, and thus is IR inactive, while the asymmetric stretch vibration is IR active. For SFG to occur, molecules need to be IR active, since the vibrational resonances are probed by IR radiation. Additionally, the molecules need to be Raman active, meaning that the vibration needs to induce a change in the molecule's polarizability. Raman activity follows from molecular symmetry in a rather complex way, and is generally listed in textbooks of quantum chemistry [14].

If the criteria of IR and Raman activity are both satisfied and symmetry is broken, an SFG spectrum can be generated with features similar to those obtained with linear spectroscopic techniques, while retaining interface specificity and background-free detection. More specifically, the resonant beam can be a tunable or broadband mid-IR laser source to excite vibrational modes. If the second beam is then chosen to have a frequency in the red part of the visible spectrum or in the near-IR, the SFG, which necessarily has a higher frequency, will lie nicely in the visible spectral region. With this configuration, an added possible advantage of SFG spectroscopy over linear IR spectroscopy is that the upconverted vibrational spectrum can be detected using standard charge coupled device (CCD) technology with much higher sensitivity than that of a typical IR detector. Sometimes SFG is therefore simply used as a method to enable more sensitive detection of an IR signal [15].

SFG spectroscopy was first applied by the group of Yuen-Ron Shen at Berkeley in 1987 [16]. The studied system was an octadecyltrichlorosilane (OCT) monolayer, prepared at several different air/solid and liquid/solid interfaces. It was shown that the CH bonds of the long alkyl chains of OCT give rise to a distinct SFG signal, confirming that they are oriented perpendicular to the surface. The CH spectral region was further investigated for the methanol vapor/liquid interface [17]. A later study by Geraldine Richmond described how the ratio between CH_3 and CH_2 modes is a reliable indicator of the order of carbohydrates at the interface [18]. This practice is explained in more detail in the next section.

Throughout the last two decades, SFG studies have been used to reveal detailed properties of the air/water interface [19–24]. Uniquely, SFG spectroscopy is able to reveal the dangling or free OH bond at hydrophobic interfaces [25,26]. This resonance is spectrally separated from the bulk water contribution because
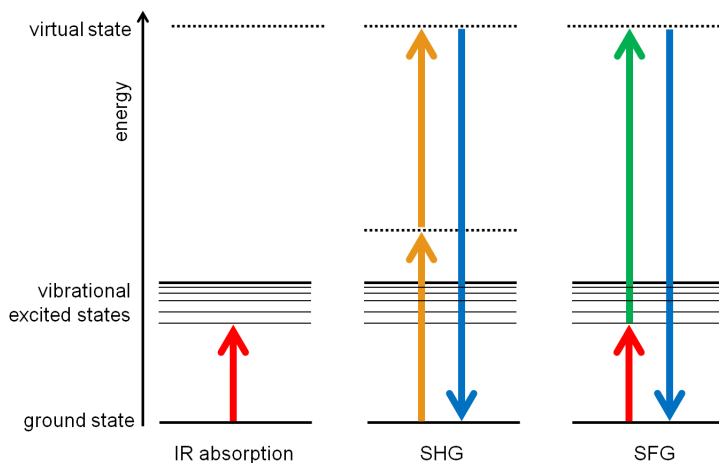
FIGURE 1.3. Energy diagrams comparing IR absorption, nonresonant SHG and resonant SFG.

it is not hydrogen bonded. Undampened by hydrogen bonds, the free OH vibration has a higher energy and frequency than the hydrogen bonded bulk. From the SFG spectrum it was concluded that at the air/water interface about 20% of the interfacial water molecules have a free OH bond sticking out of the bulk. Chapter 4 of this thesis explores the free OH bond in more detail, including the effect of isotopic dilution of OH to OD.

SFG being a relatively new, powerful spectroscopic technique, the range of applications of SFG spectroscopy is still growing. The number and diversity of recent SFG studies is too great to adequately summarize here, but several excellent recent review papers are recommended to the interested reader. These include an older overview of SFG applied to liquid interfaces [26], a general overview of possible applications [27], summaries of solid/liquid SFG studies [28,29], recapitulations of SFG data on the air/water interface [20,21,23], and an overview of SFG spectroscopy on self-assembled organic (Langmuir) monolayers [30].

The basic technique of SFG spectroscopy has remained the same since its first use, but certain developments, such as polarization-dependent measurements [31] and novel experimental geometries [29] have increased the potential of application. Another development that is seeing increasingly more use is phase-specific SFG (PS-SFG) spectroscopy. This interferometric technique enables the detection of the absolute orientation of interfacial molecules [20,32–36]. In chapter 5 the theoretical and experimental details of this technique are described in detail. Furthermore, the development of higher-power, shorter-pulsed and more stable laser sources has made effective time-resolved measurements possible [37–42]. During the last decade, much progress has been made in this field, including two-dimensional techniques [43–45]. Using these advanced methods, the hydrogen bonding and molecular environment of interfacial water

species was probed through their vibrational relaxation. This promising field is quickly developing, but lies outside the scope of this work.

1.3 SFG SPECTROSCOPY OF BIO-INTERFACES

In this thesis, I describe a series of experiments in the field of biochemical physics. Perhaps it seems needlessly confusing, or even presumptuous, to combine three major fields of science in one term. However, all three approaches of the natural sciences are important to the current topic. Biology, firstly, provides the context. The system that inspires our research is the cell membrane, which forms the boundary of all living cells and provides the environment for many of the biochemical processes that enable an organism to live. The questions we address are often derived from issues in medicine or biology, like: can nanomaterials be toxic? Why do proteins function in one lipid environment but not in another? Whenever possible, we choose to work with materials that are biologically relevant. In this field of research the focus is on molecular mechanisms, but often the discussion is introduced and concluded with a view of the physiological context.

Secondly, a chemistry approach is necessary to provide the link between the macroscopic and atomic world. In every choice of materials and in every discussion, the chemical structure and behavior should be considered. Only if we understand the influence of factors like hydrophobicity, reactivity and pH-dependence of the studied system or interaction can we draw valid conclusions from our spectral observations.

The experiments start and end with physics. We apply a very specific non-linear spectroscopic technique, which cannot be efficiently used without proper understanding of the optical processes involved. To overcome technical difficulties, which are all too common in advanced science, and to optimize IR generation and data collection, an experimental physicists approach is necessary. Finally, when quantitatively analyzing the spectra, we consider what laws of physics drive the studied system. Electrostatics, entropic forces and heating effects are all relevant to the samples described in this work. Although we do not presume that the entire system can be described by a quantitatively correct and complete model, we aim to explain the origins of the system's behavior on the most fundamental level possible.

A biological cell membrane is very complex. It is composed of different kinds of phospholipids, glycolipids and cholesterol, which are all amphiphilic molecules, meaning that they are partly hydrophilic (water-loving; the polar head group) and partly hydrophobic (water-fearing; the fatty alkyl chains). Figure 1.4 shows the chemical structure of one such molecule, the phospholipid DPPC. Because of this amphiphilic structure, it is energetically favorable for these lipids to stay at an interface between an aqueous and apolar environment. Because of this tendency, a high concentration of lipids will self-assemble into an ordered monolayer at such an interface. Within a purely aqueous environment, and depending on the lipid concentration, they tend to form bilayer structures,

with the hydrophobic alkyl chains facing each other and head groups pointing out into the polar solvent. By this mechanism the basic cell membrane is formed. Innumerable carbohydrates and proteins are attached to or embedded within this already heterogeneous basic structure.
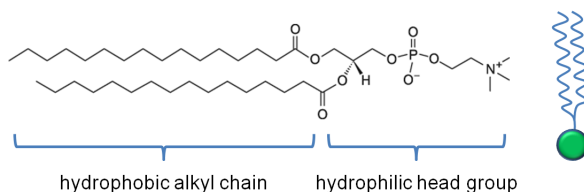

FIGURE 1.4. Chemical structure of the phospholipid DPPC. On the right, a schematic representation of the molecule is given with the hydrophilic head group (shaded circle) below and the hydrophobic alkyl chains above. This representation is used throughout this work.

When trying to understand the physics of a system of interacting bodies, we are confronted with a number of interactions that increases exponentially with the number of component types. In a system as complex as the cell membrane, this means that any attempt to single out a physical property will be obscured by many interfering processes. Thus, in order to enable a quantitative approach of the cell membrane, we have to limit its complexity by finding a suitable model system. In this thesis, we do so by only considering the phospholipids, which when released at the air/water interface self-assemble into a membrane-like monolayer. This monolayer is only one of the two leaflets that form a bilayer. But, since the interactions between two leaflets are weak compared to the interactions within one such leaflet, a monolayer shares many of the physical properties of a bilayer. This homogeneous, controllable system will be our basic model membrane.

Vibrational SFG spectroscopy is an ideal tool to probe these monomolecular layers, also known as Langmuir monolayers. The CH bonds of the alkyl chains have strong and distinct vibrational modes. The exact shape and size of their spectral response indicates how ordered the monolayer is, which is affected by the interfacial lipid density, but possibly also by interactions with other molecular species [18, 46]. Typically, at low lipid concentration the lipids will be in an expanded phase, meaning that their alkyl chains are spread out and disordered. Adding lipids to the surface compresses them more tightly together, until they reach a condensed phase in which they are tightly packed and highly ordered. The lipid monolayer can be seen as a two-dimensional fluid, and the change from expanded to condensed phase as an actual phase change from fluid to gel-like behavior. Note, however, that this phase behavior differs for each lipid species: some lipids have an intermediate heterogeneous expanded/condensed coexistence phase while others do not, and the temperature at which these phase changes occur varies greatly per lipid.

The hydrophobic lipid head groups mostly manifest themselves through their effect on the interfacial water. The head group interacts with the wa-

ter molecules by means of electrostatic forces and/or hydrogen bonding, which typically influences the alignment of water relative to the surface. Positively charged phospholipids, for instance, will orient a water molecule with its electronegative oxygen atom up towards the monolayer, while negatively charged lipids will attract the water's positive hydrogen atoms. Any such change in molecular alignment alters the interfacial molecular symmetry, which will be detectable as an increase or decrease of the spectral water feature.
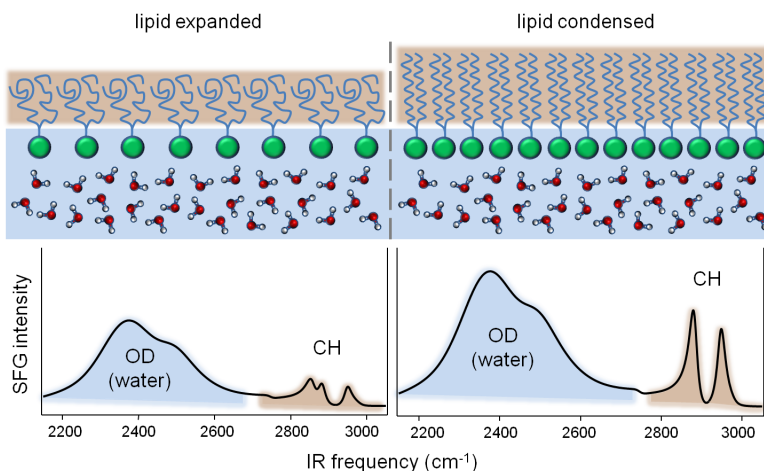
FIGURE 1.5. Schematic depiction of a phospholipid monolayer in the expanded (top left) and condensed (top right) phase. Below each image, a typical SFG spectrum is shown. The water and CH spectral regions are color coded.

Molecular monolayers in the lipid expanded and lipid condensed phases are drawn schematically in figure 1.5. Below the schematic, a typical SFG spectrum is shown, indicating the OD stretch vibration of heavy water (D_2O)[a] and the CH stretch vibrational region. As is customary in infrared spectroscopy, frequency is given in waves per centimeter, cm^{-1}. For the expanded phase, three CH peaks are visible. The first comes from CH_2 modes along the alkyl chain, while the other two are CH_3 modes at the alkyl chain terminus. For the lipid condensed phase, only two modes remain: the CH_2 mode has disappeared. This is a consequence of the order of the alkyl chains, which now forms a highly centrosymmetric layer and is not SFG active anymore. This layer ends in the CH_3 groups, which now form a well-defined interface that is even more SFG active than before. In this example, the lipid head group is negatively charged, causing the water to align with their hydrogen atoms up towards it. This non-centrosymmetric water layer gives rise to a broad water response in the SFG spectrum. The large bandwidth arises from inhomogeneous broadening due to the many hydrogen-bonded states the water molecules may have, each hydrogen bond differently affecting their resonance frequency. When we compare the

---

[a]The often preferred use of D_2O over H_2O is explained in chapter 3.

lipid expanded and lipid condensed monolayer in figure 1.5, the water signal is typically larger in the latter case. This is a result of the higher lipid (and therefore charge) density of a dense monolayer, increasing the electrostatic field at the interface. This field is experienced by the water molecule dipoles, increasing their alignment, which we observe as a larger SFG response in the spectrum.

Understanding the origin of spectral changes in the SFG spectrum allows us to investigate interactions at the interface with molecular precision. When looking at the bare air/water interface, charged or surface-active molecules or ions will interrupt the interfacial hydrogen bond structure, changing the SFG water signal [47–50]. Interactions at lipid monolayers will not only change the water signal, but may also change the order of the alkyl chains. Clear spectral signatures have been reported of the interaction of a model membrane with ions [51,52], with DNA [53,54], and with various peptides and proteins [55–59]. Additionally, in this thesis we will introduce SFG as a tool to study the (nonspecific) interaction of model membranes and synthetic nanomaterials. The effect of nanoparticles and carbon nanotubes on biological matter, and specifically the cell membrane, is of high interest due to toxicity issues and possible medical applications [60–62]. Combining vibrational SFG spectroscopy with other approaches, like surface tensiometry, atomic force microscopy (AFM), scanning electron microscopy (SEM) and molecular dynamics (MD) simulations, provides a strong basis for modeling the molecular orientation and dynamics of these interactions.

1.4 THESIS OVERVIEW

We have now established lipid monolayers as a model system for the cell membrane, and developed a basic understanding of how the molecular structure can be derived from the SFG spectrum. It is impressive how SFG spectroscopy can produce clear vibrational data of interfacial water or of a monolayer of single-molecular thickness. This thesis covers the application of vibrational SFG spectroscopy to various aqueous interfacial systems. Since the technique is still evolving, a significant part of this thesis explores new ways to implement it. This exploration is both technical, trying to refine and advance the methodology, and topical, applying the technique to new interfacial systems. When possible a molecular model is presented based on spectral data. This thesis contains the following chapters:

- **Chapter 2** presents the theoretical aspects of the work discussed in this thesis. The theoretical foundation of the technique is outlined, starting from a description of the interaction of light and matter. Then, nonlinear optical processes are introduced, focusing on SFG. Finally, the details of spectral analysis are described.

- **Chapter 3** presents the experimental aspects of this research work. Here, the vibrational SFG spectroscopy setup is described in detail. Additionally, tensiometry and preparation of lipid monolayers are briefly discussed.

- **Chapter 4** presents the influence of nuclear quantum effects on the alignment of isotopically diluted water at the water-air interface. The chapter starts with a description of molecular dynamics simulations, followed by SFG results. The combination of simulation and experiment confirms the influence of nuclear quantum effects on the water alignment.

- **Chapter 5** presents a comparison between standard, direct SFG and the more advanced technique of PS-SFG spectroscopy. The experimental and analytical processes are described in detail as both methods are applied to lipid monolayer systems of positive and negative charge.

- **Chapter 6**. presents a systematic SFG study of positively and negatively charged nanoparticles interacting with charged lipid membranes. The effect of charge on the lipid organization and water alignment is described, and a model describing the nanoparticle location relative to the surface is presented.

- **Chapter 7** presents a study of the interaction of a charged lipid membrane with single-walled carbon nanotubes made soluble with DNA. A combination of tensiometry, vibrational SFG spectroscopy and a membrane leakage experiment leads to a model of the dynamics of the association of the nanotubes with the membrane surface.

2   THEORY

2.1   NONLINEAR POLARIZATION

The data presented in this thesis are obtained, for the largest part, by means of spectroscopic techniques. Spectroscopy is the practice of characterising matter by looking at its interaction with light. Being electromagnetic radiation itself, light is affected by the electronic and magnetic properties of the molecules and atoms that it encounters. Given that the electronic forces and interactions are many orders of magnitude larger than the magnetic ones, we will deduce the theoretical description of spectroscopy to the coupling of the electric fields of light and matter.

This chapter is largely based on the excellent tutorial overviews of Lambert [63] and Miranda [26]. The discussion is limited to the electric dipole approximation, not considering quadrupole and higher contributions, and ignoring interactions between the dipoles of molecules. For an advanced and thorough description, refer to textbooks by Boyd [64] and Shen [65] which provide the quantum mechanical background necessary for a more complete understanding of the principles of SFG.

Let us consider the interaction of a molecule with a light source through the oscillating electric field $\mathbf{E}$.[a] The molecule's electron cloud will follow the oscillation, inducing an electric polarization $\boldsymbol{\mu}$ proportional to the electric field:

$$\boldsymbol{\mu} = \alpha \mathbf{E} \tag{2.1}$$

where the proportionality constant α is the polarizability of the molecule. For a large number of molecules in a condensed state, the individual molecular polarizabilities can be summed up to find the macroscopic polarizability. This material property is called the susceptibility χ and determines the bulk polarization $\mathbf{P}$ induced by an electric field:

$$\mathbf{P} = \epsilon_0 \chi \mathbf{E} \tag{2.2}$$

where ϵ_0 is the permittivity of free space. For the intense, coherent fields of high-power pulsed laser light, however, equation 2.1 and 2.2 break down. On the molecular level, the electron cloud cannot follow the oscillation any more, introducing anharmonicity in its response. Macroscopically, this anharmonicity manifests itself as a nonlinearity of the susceptibility χ. We may express this nonlinearity by writing χ as a sum of components, $\chi = \chi^{(1)} + \chi^{(2)} + \chi^{(3)} + ...$

---

[a]Throughout this chapter, bold typeface indicates a vector quantity with both magnitude and direction.

Here $\chi^{(1)}$, the first-order susceptibility, expresses the linear relation between $\mathbf{P}$ and $\mathbf{E}$. The second-order nonlinear susceptibility $\chi^{(2)}$ expresses the quadratic relation between $\mathbf{P}$ and $\mathbf{E}$, the third-order nonlinear susceptibility $\chi^{(3}$ the cubic relation between $\mathbf{P}$ and $\mathbf{E}$, etcetera, where the nonlinear terms are much smaller than the linear one. Equation 2.2 now becomes

$$\mathbf{P} = \epsilon_0 \left(\chi^{(1)}\mathbf{E} + \chi^{(2)}\mathbf{E}^2 + \chi^{(3)}\mathbf{E}^3 + ... \right) \tag{2.3}$$

The two-photon processes SHG and SFG originate from the second-order nonlinear susceptibility $\chi^{(2)}$. We can demonstrate this by explicitly stating the time dependence of $\mathbf{E}$,

$$\mathbf{E} = \mathbf{E}_1 \cos \omega t \tag{2.4}$$

Considering only the polarization due to second-order effects $\mathbf{P}^{(2)}$, we obtain

$$\mathbf{P}^{(2)} = \epsilon_0 \chi^{(2)} \left(\mathbf{E}_1 \cos \omega t \right)^2 = \frac{1}{2}\epsilon_0 \chi^{(2)} \mathbf{E}_1^2 \left(1 + \cos 2\omega t \right) \tag{2.5}$$

This demonstrates that through $\chi^{(2)}$, an electric field of frequency ω may cause a polarization that oscillates at a frequency 2ω.

To explore the origins of SFG, we need to consider an electric field consisting of two different frequencies ω_1 and ω_2:

$$\mathbf{E} = \mathbf{E}_1 \cos \omega_1 t + \mathbf{E}_2 \cos \omega_2 t \tag{2.6}$$

Producing the second-order polarization

$$\begin{aligned} \mathbf{P}^{(2)} &= \epsilon_0 \chi^{(2)} \left(\mathbf{E}_1 \cos \omega_1 t + \mathbf{E}_2 \cos \omega_2 t \right)^2 \\ &= \epsilon_0 \chi^{(2)} (\mathbf{E}_1^2 \cos^2 \omega_1 t + \mathbf{E}_2^2 \cos^2 \omega_2 t \\ &\quad + \mathbf{E}_1 \mathbf{E}_2 \cos(\omega_1 + \omega_2)t + \mathbf{E}_1 \mathbf{E}_2 \cos(\omega_1 - \omega_2)t) \\ &= \frac{1}{2}\epsilon_0 \chi^{(2)} (\mathbf{E}_1^2 + \mathbf{E}_2^2 + \mathbf{E}_1^2 \cos 2\omega_1 t + \mathbf{E}_2^2 \cos 2\omega_2 t \\ &\quad + 2\mathbf{E}_1 \mathbf{E}_2 \cos(\omega_1 + \omega_2)t + 2\mathbf{E}_1 \mathbf{E}_2 \cos(\omega_1 - \omega_2)t) \end{aligned} \tag{2.7}$$

This expression shows all contributions of the second-order nonlinear susceptibility $\chi^{(2)}$ to the polarization. There are two constant terms, two SHG terms corresponding to the two doubled original frequencies, the sum-frequency (SF) term, and a difference-frequency (DF) term. In an SFG experiment, all of these contributions will be present. However, since we are specifically detecting the SF signal, in practice they do not influence the measurement. In the following discussion we will therefore only elaborate on the SF term. Omitting the explicit time dependence again, we may express the SF component of the polarizability as

$$\mathbf{P}_{\text{SF}}^{(2)} = \epsilon_0 \chi^{(2)} \mathbf{E}_1 \mathbf{E}_2 \tag{2.8}$$

In the context of this thesis, $\mathbf{E}_1$ and $\mathbf{E}_2$ are the fields originating from a visible and IR pulsed laser source, $\mathbf{E}_{\text{VIS}}$ and $\mathbf{E}_{\text{IR}}$. The vector quantities $\mathbf{P}^{(2)}_{\text{SF}}$, $\mathbf{E}_{\text{VIS}}$ and $\mathbf{E}_{\text{IR}}$ can all have components in each of the three dimensions. Therefore, in Cartesian coordinates $\chi^{(2)}$ is a third-rank tensor with 27 elements. The y-component of $\mathbf{P}^{(2)}_{\text{SF}}$ originating from the y-component of $\mathbf{E}_{\text{VIS}}$ and the z-component of $\mathbf{E}_{\text{IR}}$, for example, is given by

$$\mathbf{P}^{(2)}_{y,\text{SF}} = \epsilon_0 \chi^{(2)}_{yyz} \mathbf{E}_{y,\text{VIS}} \mathbf{E}_{z,\text{IR}} \tag{2.9}$$

The full description of $\mathbf{P}^{(2)}_{\text{SF}}$, including all possible vector components, is given by summing over all three dimensions:

$$\mathbf{P}^{(2)}_{\text{SF}} = \sum_i^{x,y,z} \mathbf{P}^{(2)}_{i,\text{SF}} = \epsilon_0 \sum_i^{x,y,z} \sum_j^{x,y,z} \sum_k^{x,y,z} \chi^{(2)}_{ijk} \mathbf{E}_{j,\text{VIS}} \mathbf{E}_{k,\text{IR}} \tag{2.10}$$

Since $\chi^{(2)}_{ijk}$ describes the physical response of the material to radiation, its properties should be independent of the axis system. Redefining all axes by reversing their sign should also reverse the sign of $\chi^{(2)}_{ijk}$ describing the physical material properties, i. e. ,

$$\chi^{(2)}_{ijk} = -\chi^{(2)}_{-i-j-k} \tag{2.11}$$

However, in a centrosymmetric medium all directions are equivalent. Reversing the axis system in a this environment does not change anything about the description of the system, including $\chi^{(2)}_{ijk}$:

$$\chi^{(2)}_{ijk} = \chi^{(2)}_{-i-j-k} \tag{2.12}$$

The apparent contradiction between equations 2.11 and 2.12 indicates that $\chi^{(2)}_{ijk}$ can only be zero in a centrosymmetric medium [b]. Thus, an SFG signal can only be generated when this symmetry is broken. This typically occurs at an interface between two bulk media, where the medium is isotropic in the planar surface formed by the x and y-axes , but the not along the z-axis. Such a medium is said to have C_∞ symmetry. All systems studied in this thesis fall within this category.

Intuitively, although incompletely, the requirement of symmetry breaking can be understood in terms of the molecular hyperpolarizabilities canceling out on the microscopic scale.

2.2 THE ELECTRIC FIELD AT AN INTERFACE

We have established that laser light can induce an SF oscillation in the macroscopic polarization of a material, providing it is not centrosymmetric. Equation

---

[b]The same reasoning can be applied to any odd-order tensor quantity, implying that $\chi^{(4)}_{ijk}$, $\chi^{(6)}_{ijk}$, etcetera are also zero in a centrosymmetric medium

2.8 shows how this polarization follows from the local electric fields. However, we still need to derice how the magnitude of this field follows from the incident laser light.
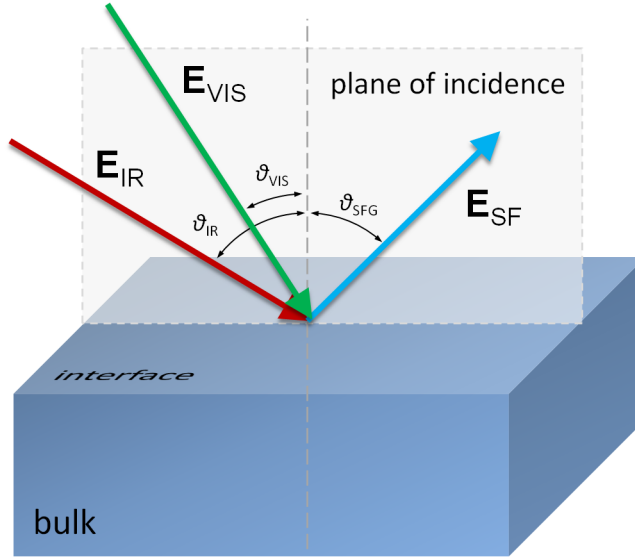

FIGURE 2.1. Generation of the SFG signal at an interface.

In equation 2.7 we found the origin of the SF component. For a visible and IR source of frequencies ω_{VIS} and ω_{IR}, the frequency of the resulting SFG signal will be

$$\omega_{\mathrm{SF}} = \omega_{\mathrm{VIS}} + \omega_{\mathrm{IR}} \qquad (2.13)$$

The angle at which the SFG signal is generated is defined by the angles of incidence of the visible and IR laser beams through the conservation of momentum:

$$n_{\mathrm{SF}} k_{\mathrm{SF}} \sin \theta_{\mathrm{SF}} = n_{\mathrm{VIS}} k_{\mathrm{VIS}} \sin \theta_{\mathrm{VIS}} + n_{\mathrm{IR}} k_{\mathrm{IR}} \sin \theta_{\mathrm{IR}} \qquad (2.14)$$

where all angles are given relative to the surface normal as indicated in figure 2.1, n is the refractive index of the propagation medium and $k = \omega/c$, with c the speed of light. Note that two SFG signals are generated at the interface: one reflected from it, and one propagating into the bulk. In this thesis, only the reflected signal is detected, because it is more easily accessible than the signal disappearing into the sample. The relative sizes of the two signals scale with the reflection coefficients discussed later this chapter. Generally, we will only consider the reflection signal to avoid unnecessary complication.

The direction of the oscillation of the incident visible and IR beams, i.e. their polarization, can be split into two components. The component parallel to the plane of incidence is called p-polarized (from parallel), while the one
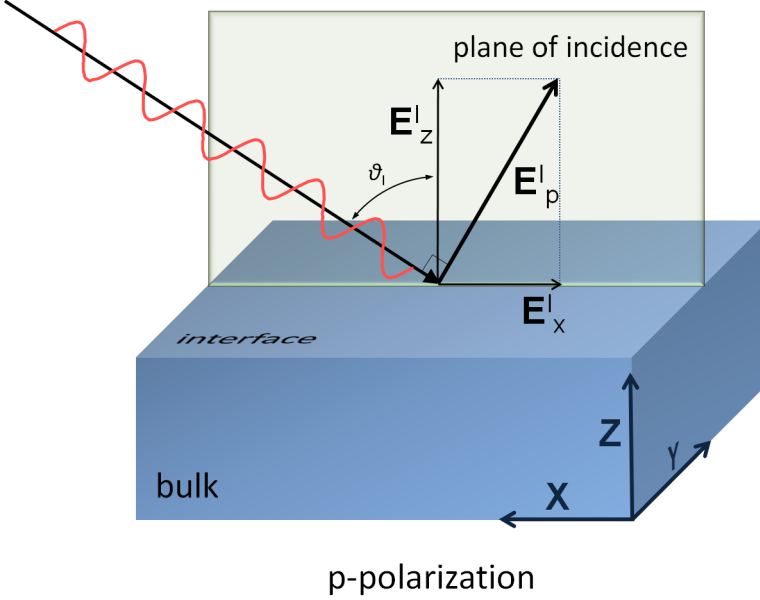
FIGURE 2.2. p-polarized light at an interface. The interfacial electric field can be split up into an x and a z-component.

perpendicular to it is called s-polarized (from *senkrecht*, German for perpendicular). The orientation of a p-polarized incident beam of magnitude E_p^I and the orientation of an s-polarized incident beam of magnitude E_s^I are demonstrated in figures 2.2 and 2.3, respectively. Because in a typical optical setup the beams are reflected into a complex path, the p/s convention relative to the beam is much more practical than the use of a fixed axis system. To calculate the SFG response from the interface, however, we need to be able to express the electric fields in terms of their Cartesian coordinates. From figure 2.2 and 2.3 we may deduce the following relation:

$$\begin{aligned}
\mathbf{E}_x^I &= E_x^I \hat{\mathbf{x}} = -E_p^I \cos\theta_I \hat{\mathbf{x}} \\
\mathbf{E}_y^I &= E_y^I \hat{\mathbf{y}} = E_s^I \hat{\mathbf{y}} \\
\mathbf{E}_z^I &= E_z^I \hat{\mathbf{z}} = E_p^I \sin\theta_I \hat{\mathbf{z}}
\end{aligned} \tag{2.15}$$

To find the SFG polarization from equation 2.10, it is not the incident fields that we need, but rather the interfacial electric fields. These are the sum of the incident and the reflected field. The latter is found by multiplying the incident field by the Fresnel amplitude coefficients for reflection; r_p for p-polarized light, and r_s for s-polarized light:
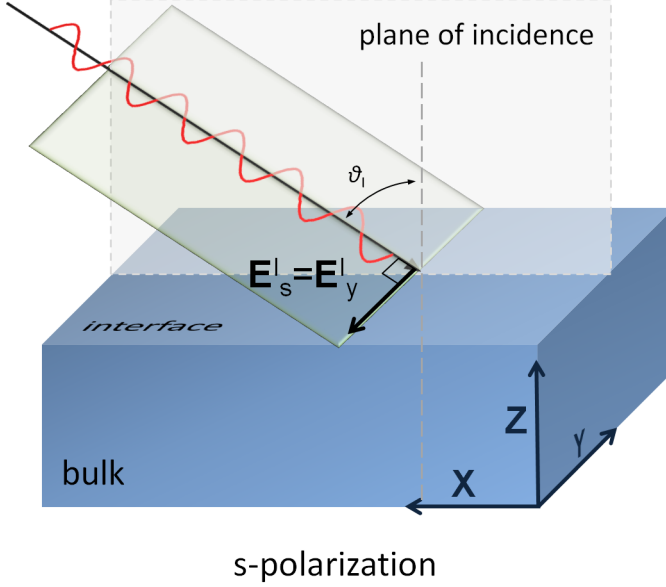
FIGURE 2.3. *p*-polarized light at an interface. The interfacial electric field contains only a y-component.

$$r_p \equiv \frac{E_p^R}{E_p^I} = \frac{n_T \cos\theta_I - n_I \cos\theta_T}{n_T \cos\theta_I + n_I \cos\theta_T}$$
$$r_s \equiv \frac{E_s^R}{E_s^I} = \frac{n_I \cos\theta_I - n_T \cos\theta_T}{n_I \cos\theta_I + n_T \cos\theta_T} \tag{2.16}$$

We can now describe the magnitude of the interfacial field as a function of the incident fields.

$$\begin{aligned}
E_x &= E_x^I + E_x^R = E_x^I + r_p E_x^I = -\left(E_p^I \cos\theta_I + r_p E_p^I \cos\theta_I\right) \\
&= -E_p^I \cos\theta_I(1 + r_p) \equiv -K_x E_p^I \\
E_y &= E_y^I + E_y^R = E_y^I + r_s E_y^I = E_s^I + r_s E_s^I = E_s^I(1 + r_s) \equiv K_y E_s^I \quad \text{(2.17)} \\
E_z &= E_z^I + E_z^R = E_z^I + r_p E_z^I = E_p^I \sin\theta_I + r_p E_p^I \sin\theta_I \equiv K_z E_p^I \\
&= E_p^I \sin\theta_I(1 + r_p)
\end{aligned}$$

where in the last step we defined the Fresnel *K*-factors to simplify the notation. We then arrive at the full expression for the SF polarization (omitting the summation operators):

$$\mathbf{P}_{i,\text{SF}}^{(2)} = \epsilon_0 \chi_{ijk}^{(2)} \hat{\mathbf{j}} K_j E_{p/s,\text{VIS}}^I \hat{\mathbf{k}} K_k E_{p/s,\text{IR}}^I \tag{2.18}$$

2.3   EMISSION OF THE SFG SIGNAL

Up to now, we have described the SF polarization generated at the interface. The next step is to show how this polarization gives rise to the emission of radiation at this frequency. The relation between radiation and the SFG field is given by the nonlinear Fresnel coefficients, or L-factors:

$$\mathbf{E}_{i,\mathrm{SF}} = L_i \mathbf{P}^{(2)}_{i,\mathrm{SF}} \tag{2.19}$$

The L-factors are based on conservation of momentum (phase-matching) conditions between the waves, and continuity of the electric fields across the interface [66]. For a reflection geometry, they are given by

$$
\begin{aligned}
L_x^R &= -\frac{i\omega_{\mathrm{SF}}}{c\epsilon_0} \frac{\cos\theta_{\mathrm{SF}}^T}{n_T\cos\theta_{\mathrm{SF}}^I + n_I\cos\theta_{\mathrm{SF}}^T} \\
L_y^R &= \frac{i\omega_{\mathrm{SF}}}{c\epsilon_0} \frac{1}{n_I\cos\theta_{\mathrm{SF}}^I + n_T\cos\theta_{\mathrm{SF}}^T} \\
L_z^R &= \frac{i\omega_{\mathrm{SF}}}{c\epsilon_0} \frac{(n_T/n_{\mathrm{layer}})^2 \sin\theta_{\mathrm{SF}}^T}{n_I\cos\theta_{\mathrm{SF}}^T + n_T\cos\theta_{\mathrm{SF}}^I}
\end{aligned}
\tag{2.20}
$$

Here, the angles θ_{SF}^I and θ_{SF}^T are the angles of the emitted SFG field in the incidence and transmission medium, respectively, while n_I and n_T are the refractive indices in these media. n_{layer} is the refractive index of the interface, which may be different from those of the two bulk materials bordering it, and can be hard to define. Combining equation 2.18 and 2.19, we can now fully describe the SFG signal generated at an interface based on the angles of incidence and field magnitudes of the visible and IR beam, the refractive indices of the sample, and the second-order nonresonant susceptibility $\chi^{(2)}$. Note that both the K and the L-factors are also defined by these properties. The intensity of the SFG signal scales with the square of its field strength. The complete description of the p and s components of the intensity of the emitted SFG radiation then becomes

$$I_{p,\text{SF}} \propto |\mathbf{E}_{x,\text{SF}}|^2 + |\mathbf{E}_{z,\text{SF}}|^2$$

$$\propto \left| L_x \mathbf{P}^{(2)}_{x,\text{SF}} \right|^2 + \left| L_z \mathbf{P}^{(2)}_{z,\text{SF}} \right|^2$$

$$\propto \left| \epsilon_0 L_x \sum_j^{x,y,z} \sum_k^{x,y,z} \chi^{(2)}_{xjk} K_j E^I_{p,\text{VIS}} K_k E^I_{p,\text{IR}} \right|^2$$

$$+ \left| \epsilon_0 L_z \sum_j^{x,y,z} \sum_k^{x,y,z} \chi^{(2)}_{zjk} K_j E^I_{p,\text{VIS}} K_k E^I_{p,\text{IR}} \right|^2 \qquad (2.21)$$

$$I_{s,\text{SF}} \propto |\mathbf{E}_{y,\text{SF}}|^2$$

$$\propto \left| L_y \mathbf{P}^{(2)}_{y,\text{SF}} \right|^2$$

$$+ \left| \epsilon_0 L_y \sum_j^{x,y,z} \sum_k^{x,y,z} \chi^{(2)}_{yjk} K_j E^I_{s,\text{VIS}} K_k E^I_{s,\text{IR}} \right|^2$$

2.4 SPECTRAL ANALYSIS OF THE SFG SIGNAL

In the previous sections, we have derived how the SFG signal originates from two overlapping beams at an interface, and how its magnitude depends on the setup geometry and material properties. In this thesis, SFG is used as a means to obtain information about the molecular structure at surfaces. To quantify this information, the spectra are fitted with a model that describes the material properties underlying the response. Although many factors contribute to the SFG signal, as is described in 2.21, the only variable that is strongly frequency dependent, and therefore defines the shape of the spectrum, is the second-order susceptibility $\chi^{(2)}$. The resonances, which are used to identify the chemical structure of the sample, are contained within $\chi^{(2)}$. Spectral analysis can therefore be reduced to the fitting of $\chi^{(2)}$ with a physically meaningful mathematical expression, describing the resonant vibrational modes of the sample. Additionally, to obtain a good fit a frequency-independent nonresonant background signal is needed. This background is generally assumed to originate from electronic transitions. These transitions have a high energy but are spectrally remote, resulting in a low intensity, flat signal in the SFG spectral region. It is common to split the nonresonant contribution into a nonresonant amplitude A_{nr} and phase $e^{i\phi_{\text{nr}}}$, where ϕ_{nr} accounts for the phase difference of the nonresonant and resonant oscillations:

$$E_{\text{SF}} \propto \chi^{(2)} E_{\text{VIS}} E_{\text{IR}}$$
$$\propto \left(\chi_{\text{nr}}^{(2)} + \chi_{\text{r}}^{(2)} \right) E_{\text{VIS}} E_{\text{IR}} \tag{2.22}$$
$$\propto \left(A_{\text{nr}} e^{i\phi_{\text{nr}}} + \chi_{\text{r}}^{(2)} \right) E_{\text{VIS}} E_{\text{IR}}$$

Resonances that are driven by an external force, in our case the oscillating electric field of the IR laser, can be described by a Lorentzian function. The resonant part of $\chi^{(2)}$ can therefore be fitted as a sum of these Lorentzians, one for each resonance. The full fitting expression then becomes:

$$\chi^{(2)} = A_{\text{nr}} e^{i\phi_{nr}} + \sum_n \frac{A_n}{\omega_n - \omega_{IR} - i\Gamma_n} \tag{2.23}$$

where A_n, ω_n, and ω_{IR} are the amplitude of resonance n, the center frequency of resonance n and the frequency of the IR excitation beam. Γ_n gives the vibrational lifetime of resonance n, which defines the linewidth of the spectral feature. Equation 2.23 clearly shows that the maximum field strength is found on a resonance, where $\omega_{IR} = \omega_n$, limited in intensity by the vibrational lifetime Γ_n. A_n can be positive or negative, depending on the orientation of the molecular bond that gives rise to the vibrational resonance. When recording an SFG intensity spectrum, $I_{\text{SF}} \propto |\mathbf{E}_{\text{SF}}|^2$ and the absolute orientational information is lost in squaring of the field. In fitting however, the sign assigned to A_n is relevant to the interference of the resonances. Often, the sign is known from literature, or the molecular orientation at the interface is known. Another option is retrieval of the sign through maximum entropy method (MEM), a useful but not always successful computational method [67]. Phase-sensitive SFG spectroscopy is a more powerful, but experimentally challenging technique that is able to measure the molecular orientation directly through interference with a reference signal. Chapter 5 will discuss the theoretical and experimental approach of this technique in detail.

The resonant second-order nonlinear susceptibility, $\chi_{\text{r}}^{(2)}$, is a complex quantity. The most common way to plot it is to take its squared magnitude, since this is proportional to the SFG signal intensity. To look into the spectral properties of $\chi_{\text{r}}^{(2)}$ in more detail, it can be separated into a real and imaginary part. For a single resonance n we obtain:

$$\chi_{\text{r},n}^{(2)} = \frac{A_n}{\omega_n - \omega_{ir} - i\Gamma} \cdot \frac{\omega_n - \omega_{ir} + i\Gamma}{\omega_n - \omega_{ir} + i\Gamma} = \frac{A_n(\omega_n - \omega_{ir} + i\Gamma)}{(\omega_n - \omega_{ir})^2 + \Gamma^2}$$
$$= \frac{A_n(\omega_n - \omega_{ir})}{(\omega_n - \omega_{ir})^2 + \Gamma^2} + i \frac{A_n\Gamma}{(\omega_n - \omega_{ir})^2 + \Gamma^2} \tag{2.24}$$
$$\equiv \text{Re}\left(\chi_{\text{r},n}^{(2)} \right) + i \, \text{Im}\left(\chi_{\text{r},n}^{(2)} \right)$$

Equation 2.24 shows that for the imaginary part of the second-order nonresonant susceptibility, $\text{Im}(\chi^{(2)})$, the frequency dependence is contained only in
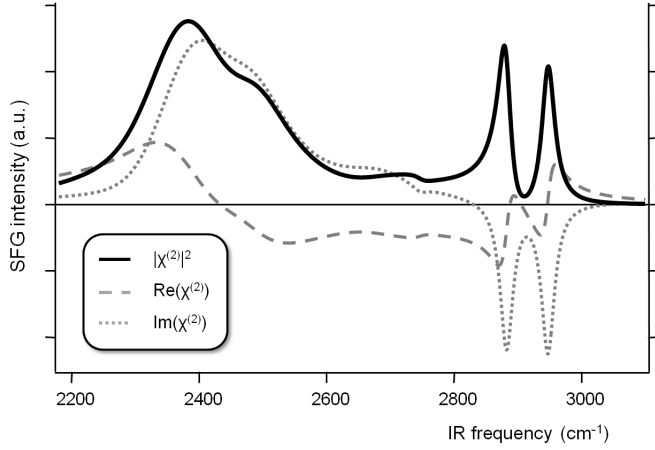
FIGURE 2.4. The fitted SFG intensity spectrum (black) along with the real (grey dashed) and imaginary (grey dotted) parts of the fit.

the denominator. This implies that its shape closely resembles that of the resonances contained within the unsquared $\chi^{(2)}$. This is demonstrated in figure 2.4, where the fitted SFG intensity spectrum of the lipid monolayer described in section 1.3 is plotted. Additionally, the $\mathrm{Re}(\chi^{(2)})$ and $\mathrm{Im}(\chi^{(2)})$ obtained from the fit are displayed. The intensity, fitted by the modeled $\left|\chi^{(2)}\right|^2$, contains clear spectral features, but only of positive amplitude. $\mathrm{Re}(\chi^{(2)})$ is distorted and difficult to interpret due to its intricate frequency dependence. $\mathrm{Im}(\chi^{(2)})$ contains roughly the same spectral features as the intensity spectrum, with the added advantage of displaying the absolute (positive or negative) amplitude of the resonances. For this reason, whenever possible it is informative to look at the $\mathrm{Im}(\chi^{(2)})$ when analysing an SFG spectrum.

3 EXPERIMENTAL MATERIALS AND METHODS

3.1 INFRARED GENERATION

The vibrational SFG data described in this thesis require an intense, pulsed source of IR radiation. The current standard in high-powered pulsed amplified systems is the titanium sapphire laser, Ti:Sapph for short. The output of a Ti:Sapph laser is centered around 800 nm, and can be converted to other wavelengths by an optical parametric amplifier (OPA). At the center of an OPA system is a nonlinear crystal. A seed pulse is generated, usually by creating white light from the amplifier's 800 nm output and filtering out unwanted frequencies. The remaining broadband pulse is combined in the crystal with an 800 nm beam in what is called the first amplification stage. Not only spatial overlap is required, but also temporal overlap, which can be challenging when using ultrashort ($\sim$35 fs) laser pulses but can be achieved by means of stable micrometer delay stages. Rotating the crystal influences the phase-matching conditions between seed and amplification. If phase matching is optimized for the seed frequency, a significant part of the 800 nm light will undergo a difference frequency generation (DFG) process, splitting into the a component that has the same energy as the seed, and a component of a frequency matching the difference in energy between the seed and the 800 nm pulse. Of the two resulting frequencies, the higher-frequency one is traditionally called the *signal*, while the lower-frequency one is called the *idler*. After the first amplification stage, one of the beams is usually discarded, and the other amplified within the crystal by a new pass of 800 nm light of much higher intensity than during the first stage. Having obtained a high signal and idler intensity, these two beams may now be combined outside the OPA in a second DFG crystal, which allows for the generation of even lower frequencies. We will now describe the process of IR generation quantitatively and in more detail, considering the OPA system shown in figure 3.1.

The IR excitation source used for the experiments described in this thesis is based on a stable and efficient OPA system that has been built and described by Hamm *et al.*. [68] It must be noted that the quantitative description given here specifically describes our OPA system rather than the general limit of the system's potential: the use of other geometries and optical materials may strongly alter the characteristics of an OPA system. In our case, the input of the system is 1.2 mJ of a ($\sim$35 fs) pulsed 800 nm amplified laser system. Two different models have been used throughout this thesis: a Coherent Legend and
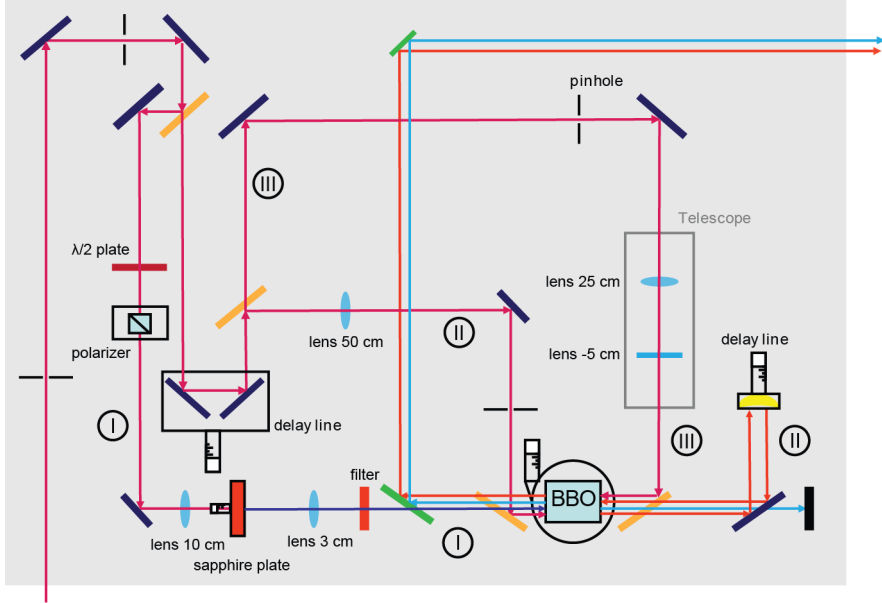
FIGURE 3.1. Experimental geometry of the optical parametric amplifier (OPA). Image adapted from [68].

a Spectra Physics Spitfire Ace, which performed practically identical for the purposes described here. In figure 3.1, the 800 nm beam is seen to enter the OPA system from the lower left. After two mirrors, it encounters a window that reflects a few percent of its power. This small signal, indicated by an encircled Roman numeral I in figure 3.1, passes a $\lambda/2$-plate and a cube polarizer. This set of optics has two functions: firstly, they change the polarization of the light from s to the p-polarization needed in the nonlinear crystal. Secondly, with this this geometry the light intensity can be sensitively controlled by rotating the $\lambda/2$-plate. This control is of importance in the next step, focusing the beam onto a 3 mm thick sapphire plate, where white light is generated. When the intensity is too high, the white light becomes unstable and distorted, but at the right intensity a nicely symmetric circular spectrum is obtained, indicating a neat beam profile. This is this seed pulse, and it continues to the nonlinear medium, a 1 mm-thick barium borate (BBO) crystal.[a]

Meanwhile, most of the 800 nm light has travelled through the first window, over a delay stage and onto a second beam splitter. A slightly larger fraction of about 10 % is now reflected and focused with a f = 50 cm lens into the BBO crystal. This is the first amplification stage, indicated by a Roman numeral II in figure 3.1. It combines with the seed to form the first signal and idler

---

[a]In the original OPA developed by Hamm *et al.* the crystal was 4 mm in thickness. Since then, the development of shorter-pulsed laser systems has increased the light intensity that the crystal can be exposed to. To prevent the crystal from being damaged by this high intensity, it should be chosen thinner to minimize the path length of the radiation within.

light, with frequency in the ranges of 1200 to 1600 nm and 1600 to 2400 nm, respectively. Their combined intensity is typically about 8 μJ. More important than the beam power at this stage is the beam profile, which is determined by the alignment and ultimately greatly affects the intensity and stability of the generated IR radiation. The signal is blocked, and the idler reflected back by means of a refocussing mirror mounted on a delay stage. When passing the BBO crystal on the way back, the idler is overlapped by the second amplification stage, indicated by a Roman numeral III in figure 3.1. This intense beam, still having an energy of about 1 mJ, is not focused onto the BBO because that would surely damage the crystal. Rather, it is narrowed by a telescope consisting of two mirrors, and then collinearly sent through the crystal along with the idler of the first amplification. With a proper alignment, a signal+idler intensity of up to 300 to 350 μJ can be obtained, implying a conversion efficiency of around 30 %. Although the near-IR signal and idler cannot be seen with the naked eye, they are intense enough to generate a strong, visible second harmonic. While this simplifies alignment of the OPA, a practical problem posed by the diverse frequencies, along with the complex experimental geometry, is that an it is difficult to efficiently protect your eyes from the potentially dangerous laser pulses.

To generate the mid-IR frequencies that are required for vibrational spectroscopy, signal and idler need to be combined in a second nonlinear crystal, silver gallium sulphide (AGS, see figure 3.2). In a DFG stage signal and idler are split by a beam splitter to optimize their time overlap before sending both through the AGS crystal.[b] The difference frequency generated by signal and idler can be controlled by changing the orientation of the BBO and AGS crystals, along with adjustments to the temporal and spatial overlap of the beams within the OPA. In our setup, this results in a mid-IR DFG signal that can be tuned between about 1600 cm^{-1}, the amide vibrational region, and 3700 cm^{-1}, the free OH vibration. After the AGS crystal, pulse energies are in the order of 5 μJ. IR generation is inevitably a very inefficient process. On the other hand, much higher IR intensities are not always welcome, since lipid samples may be influenced by heating effects even at low IR flux [69].

3.2   THE SPECTROSCOPY SETUP

The placement of the OPA within the entire SFG setup is shown in figure 3.2. In the lower left corner, we see the 800 nm amplifier that both powers the OPA and provides the visible upconversion pulse at the sample. Around 0.6 of the amplifier output is spectrally narrowed to 25 cm^{-1} using a Fabry-Perot etalon. Only about 40 μJ remains after the etalon, but the frequency narrowing is necessary to provide the SFG spectrum with a decent frequency resolution. The frequency resolution is determined by a convolution of the IR and visible pulse, and to obtain high pulse energies and broadband excitation, the IR needs

---

[b]Signal and idler do not temporally overlap before due to a phase difference in their generation within the BBO crystal [64, 68].
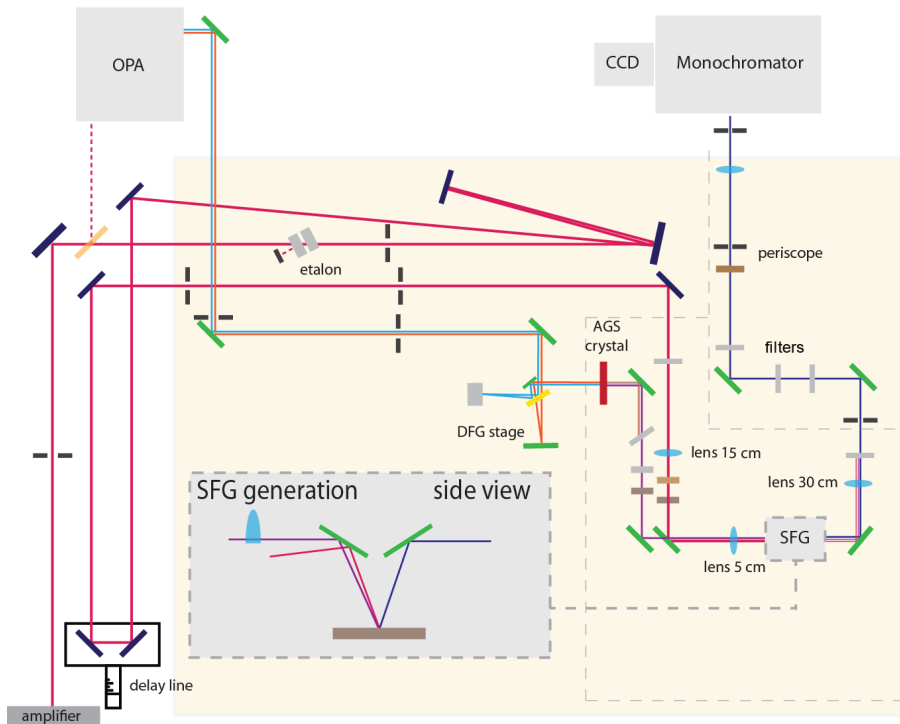
FIGURE 3.2. Experimental geometry of SFG detection. 800 nm (VIS) and mid-infrared (IR) laser pulses are combined and focused onto the sample, generating an SFG response that is detected on a CCD camera. The inset shows a side view of the beams combining on the sample.

to be spectrally broad.

After the etalon, the 800 nm beam is passed back and forth between a few mirrors to compensate the long distance that the (later) IR travels within the OPA. Only by exactly equating the traveled distance, with the help of a delay stage within the 800 nm beam path, can a pulse generated in the amplifier be recombined at the sample to generate an SFG signal. Close to the sample area, the IR beam passes through a half wave plate and polarizer before being focussed onto the sample together with the 800 nm (VIS) beam. IR and VIS are focused onto the sample by means of lenses with a focal length of 50 mm and 200 mm, with angles of incidence of 45° and 40° with respect to the surface normal. The SFG signal is reflected of the sample surface and the remaining 800 nm light is filtered out by a series of high-pass filters. and guided by a series of lenses and mirrors into a spectrograph (Acton, Princeton Instruments) where it dispersed, via a grating, and focused onto an electron multiplied charge coupled device (emCCD) camera (Newton, Andor). Unless stated otherwise, all spectra reported in this thesis are collected under the *ssp*-polarization condition (SFG

and visible s, IR p).

3.3 Sample preparation and tensiometry

The sample holder most commonly used throughout this thesis is a teflon-coated aluminum trough, with a surface area of 49 cm^2 and a volume of 20 mL. For measurements on the air/water interface (chapter 4, it suffices to fill the trough with distilled an filtered millipore water. Regularly, heavy water (D_2O) is used instead of H_2O, because its resonances lie at other frequencies. This can be useful when trying to separate the spectral response of two components, like CH and OH vibrations. Additionally, the IR excitation power obtained with our OPA system is higher at the OD resonant frequencies that at those for OH, which enables measurements with a higher signal-to-noise ratio. For measurements of lipid monolayers, a lipid solution in chloroform (sometimes with methanol) is deposited drop by drop onto the surface with a microliter syringe. In most monolayer studies, the lipid concentration at the surface was established by surface pressure measurements, also known as tensiometry. Tensiometry is an easy to use and useful tool in providing information on the lipid concentration and thermodynamical properties of lipid monolayers. The basic technique is resting a small needle tip onto the surface, attached to an electronic device that records the needle weight, indicating the surface tension. What is commonly called surface pressure can also be interpreted as a change in free energy, as can be made intuitive by noting the matching units for two-dimensional pressure and energy per surface unit area: [N/m] = [J/m2]. A change in surface free energy may be associated with the addition of substance to the surface, as is the case when adding phospholipids to the air-water interface, lowering the free energy. A lowering of the surface free energy corresponds to an increase in surface pressure π, which is defined as relative to that of clean water (π_{water}= 72.8 mN/m at room temperature) as $\pi=\pi_{water}-\pi_{surface}$. The surface pressure is typically a function of surfactant density, but may also change due to the reorganization of the molecular structure at the surface at constant surface density. In general, lipids are deposited onto the surface up to a target value. The relation between the surface pressure and the lipid density is given by an isotherm. For many lipids, these isotherms can be found in literature; alternatively, they are relatively easy to measure by compressing a monolayer of a known quantity of lipid molecules while recording the surface pressure. The shape of the isotherm reveals information about the collective behavior of the monolayer; discontinuities in the curvature indicate phase changes in the lipid monolayer [70].

4 NUCLEAR QUANTUM EFFECTS AT THE WATER-AIR INTERFACE

We start the experimental part of this thesis by looking at the fundamental physics of the bare air/water interface. Using combined theoretical and experimental approaches, we demonstrate that the bond orientation of water at the water-vapor interface depends markedly on the water isotope (H/D) composition. While the interfacial water structures of H_2O and D_2O are indistinguishable, the intramolecular symmetry breaking in HDO is directly reflected at the surface: the OD bonds preferably orient down towards the bulk water, whereas the OH bond tends to orient up into the vapor phase. Path integral molecular dynamics simulations show good agreement with surface-specific sum-frequency generation (SFG) spectroscopy results, revealing that the distinct interfacial bond orientations originate from nuclear quantum effects. The enhanced localization of the heavier D atom leads to stronger hydrogen bonds, giving rise to OD bonds pointing down into the bulk.

4.1 INTRODUCTION

Water in condensed phases is unique in its strong, anisotropic intermolecular interactions. These interactions occur through hydrogen bonds (HBs) between a H atom on one molecule and an O atom of another, and collectively lead to a structurally rich network. Nuclear quantum effects cause a non-negligible zero point energy (ZPE) for low mass nuclei, specifically for H atoms. The high density of H atoms in water makes nuclear quantum effects significant [71–75]. These effects show up when H atoms are replaced by heavier D atoms, giving rise to different macroscopic properties of H_2O and D_2O in a non-intuitive fashion: D_2O melts at a temperature 3.8 K higher than H_2O; the temperature of the maximum density increased by 7.2 K in D_2O compared with H_2O; protein stability is increased in D_2O [74]; D_2O ice is expanded relative to H_2O [75]. Isotopic substitution of water has provided an indispensable tool for studying nuclear quantum effects on water properties, structure and dynamics.

While significant understanding has been reached regarding the different HB interactions due to the isotope effects in bulk water [71–76], these effects have not been fully examined at aqueous interfaces. Aqueous interfaces require the interruption of the HB network, exhibiting specific anisotropic properties. At the water-vapor interface, this results in some interfacial water molecules having

'free' non-H-bonded OH groups sticking into the vapor phase. The water-vapor interface is of intrinsic interest owing to its ubiquity in nature, and also serves as a paradigmatic model system for extended hydrophobic surfaces. In addition to these fundamental interests, nuclear quantum effects at aqueous interfaces are relevant for interface-specific vibrational spectroscopy studies such as sum-frequency generation (SFG), where isotopic dilution has been routinely used to avoid intra- and intermolecular couplings of interfacial water [23, 24, 77–80]. Knowledge of the isotope effect is essential to verify the implicit assumption that interfacial water structures for the mixture of H_2O, D_2O, and HDO are identical.

In this chapter, we explore the nuclear quantum effects on the water structure near the vapor interface. We perform path integral molecular dynamics (PIMD) simulations to include the nuclear quantum effects explicitly [81]. Our simulation shows that the broken symmetry of the HB interactions in HDO gives rise to distinct OH and OD bond orientations at the vapor interface. We confirm distinct bond orientations by measuring SFG spectra experimentally and comparing them with the PIMD simulations.

4.2   Theory

PIMD simulations were performed with 80 water molecules by using the CP2K package program. To simplify the discussion, we used pure H_2O, D_2O, and HDO instead of their mixture. The simulation cell was set to 13.2 for the x and y axes and 70 for the z axis, where the xy plane was parallel to the interface and the z axis was parallel to the surface normal. Periodic boundary conditions were used. First, we ran classical MD simulations to sample 30 configurations for the HDO-vapor interface at 285, 300, and 315 K and 15 configurations for the H_2O-vapor and D_2O-vapor interfaces at 300 K. Then, the PIMD simulations based on generalized Langevin equations (GLE) [82] were performed at each temperature, where the independent Gaussian number N_s+1=5, the minimum frequency of thermostating ω_{min}=1 cm^{-1}, and the maximum frequency ω_{max}=10000 cm^{-1}.[a] The number of beads for the PIMD simulation, P, was set to 24. P 24 is sufficient for reproducing the quantum distribution function and energy reasonably [76]. The time step was set to 0.1fs. 100ps PIMD runs were conducted to equilibrate the systems. Sequentially, we ran over 200ps PIMD simulations to sample water configurations, which were used for calculating the bond orientations, the HB number, and the SFG spectra.

The possible anisotropy of water at interfaces can be characterized by the OH (OD) bond orientation [83], which is readily qualified by the axial profile of the angle θ between the OH (OD) bond and the surface normal. Note that two angles θ for each H_2O (D_2O) molecule were calculated. The origin point of the z-coordinate was set to the center of mass for the system. The Gibbs dividing surface is located at $|z|$=6.8 (see supporting information). Figure 4.2 depicts the average angle $\langle \cos\theta \rangle$ for H_2O, D_2O, and HDO. The H_2O and D_2O

---

[a]The parameters for the GLE thermostat were obtained from http://gle4md.berlios.de
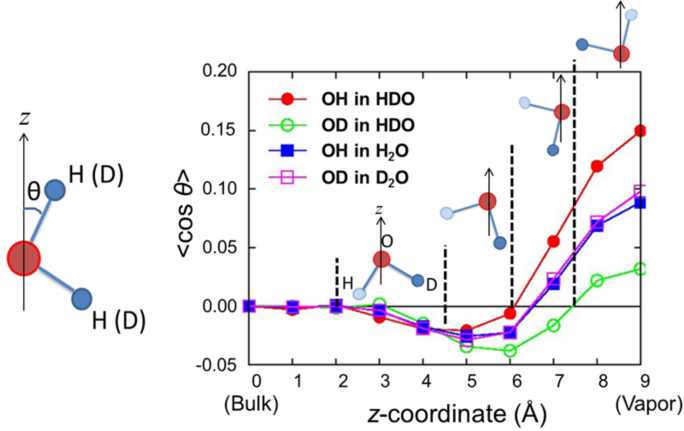
FIGURE 4.1. (Left) Pictorial representation of the angle θ between the OH (OD) bond and the surface normal. (Right) Axial distribution of average angles $\langle \cos \theta \rangle$. Lines are guides for the eye. The water molecules illustrate the average orientations of HDO (D dark grey, H light grey) in the different regions. The positive and negative z-axis points up to the vapor region and to the bulk water region, respectively.

curves overlap, indicating that the OH bond orientation of H_2O is similar to the OD orientation of D_2O. On average both the OH and OD bonds orient to the vapor phase for $|z|>6.7$ and orient to the bulk for $3.0 <|z|<6.7$, while specific orientation vanishes for $|z|<3.0$. While H_2O and D_2O give indiscernible results, the OH bond orientation of HDO is markedly different from the OD bond. In the bulk region ($|z|<2.0$), the OH and OD bonds show no specific orientations. Approaching the interface, the OH bond shows slightly stronger orientation toward the bulk than the OD bond for $2.0<|z|<4.2$, while the opposite tendency can be found for $4.2 <|z|<6.1$. In $6.1 <|z|<7.4$, the OH and OD bonds orient to the vapor and the bulk, respectively. Both the OH and OD bonds orient to the vapor region in $|z|>7.4$, but $\cos \theta$ is larger for the OH bond than the OD bond. This distinct orientation arises from nuclear quantum effects, as evidenced by its disappearance as reducing the number of beads for the PIMD simulation, P, and by its temperature dependence. At 285 K the distinct OH and OD bond orientations were enhanced while they decreased at 315K (see supporting information), which is consistent with the enhanced nuclear quantum effect at lower temperature. The symmetry is broken due to the nuclear quantum effects, so that the OH and OD bonds tend to orient toward the vapor and the bulk regions, respectively.

To elucidate the intermolecular interactions underlying the asymmetric bond orientation of HDO, we calculated the numbers of OH. . . O and OD. . . O HBs. The presence of the HB was defined as $1.59 < r_{H...O} <2.27$ and $\alpha<40°$, where $r_{H...O}$ denotes the intermolecular OH (OD) distance and α the angle between intra- and intermolecular OH (OD) bonds (see the sketch in the left side of
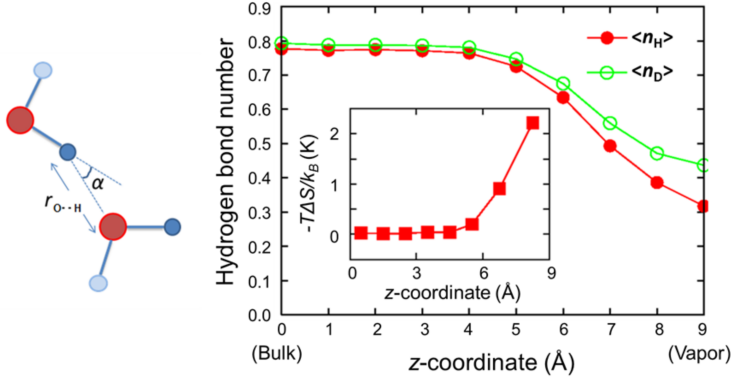
FIGURE 4.2. (Left) Pictorial representation of the distance $r_{H\ldots O}$ and the angle α for the HB definition. (Right) Depth profiles of the HB numbers for the OH O $\langle n_H \rangle$ and OD...O $\langle n_D \rangle$ at the HDO/vapor interface. The free energy loss $-T\Delta S/k_b$ originated from the entropy decrease due to the distinct OH and OD bond orientations are plotted in the inset. The lines are guide for the eyes.

figure 4.2) [84]. Figure 4.2 displays the axial profiles of the HB numbers for OH...O $\langle n_H \rangle$ and for OD...O $\langle n_D \rangle$. In the bulk region ($|z|<2.0$), $\langle n_D \rangle$ is 2% larger than $\langle n_H \rangle$, which is consistent with a more diffusive OH...O angle compared to the OD...O angle in bulk water [73]. Moving from the bulk to the vapor region, the difference between $\langle n_D \rangle$ and $\langle n_H \rangle$ increases, indicating that increased OD...O HBs stabilizes the interfacial water structure at the cost of the concomitant entropy decrease. More OD...O HBs than OH...O HBs make the enrichment of the free OH bonds pointing toward the vapor phase. Our finding can be connected with the previous study of isotopic fractionation of H_2O-HDO water [85]. By decomposing the kinetic energy into the components arising from the OH bond vector and two vectors orthogonal to the OH bond, Markland and Berne have showed that the components arising from the vectors orthogonal to the OH bond stabilizes the D excess in liquid compared to gas. This indicates that the free OH bond and hydrogen-bonded OD bond is favored compared with the free OD bond and hydrogen-bonded OH bond, which is consistent with our observation. This stronger 'H-bond' of a D atom arises from the increased moment of inertia of D_2O molecule: the librational mode does not respond as fast to changes in the environment as that of H_2O. This entails that it is more stable and has less rotational uncertainty, making it less prone to quantum tunneling effects that quickly make and break bonds [86,87].

The entropic cost of creating this asymmetry should be balanced by the OH...O and OD...O HB energy difference. This HB energy difference results in a melting point difference of 3.8 K between bulk H_2O and D_2O. In the following we will demonstrate that an energy difference corresponding to a few K originating from the nuclear quantum effects is enough to generate the distinct OH and OD bond orientations at the HDO-vapor interface. Our calculation

methodology is as follows: The entropy would be maximal when the OH and OD bond orientations are the same. The entropy for this hypothetical case is denoted by S_1. On the other hand, our PIMD simulations show different preferred orientations of the OH and OD bonds. The entropy of this case is called S_2. The entropy decrease due to the distinct bond orientations can then be calculated as $\Delta S = S_2 - S_1$. S_1 and S_2 were calculated from the histograms of the OH and OD bond orientations (see supporting information). The axial profile of $-T\Delta S/k_b$ for one HDO molecule is plotted in the inset of figure 4.2, indicating that $-T\Delta S/k_b$ increases with approaching the vapor region and reaches a maximum value of a few K, i.e. the same magnitude as the melting point difference between H_2O and D_2O. This shows that energetic gain and entropic costs for the preferred bond orientations are balanced.
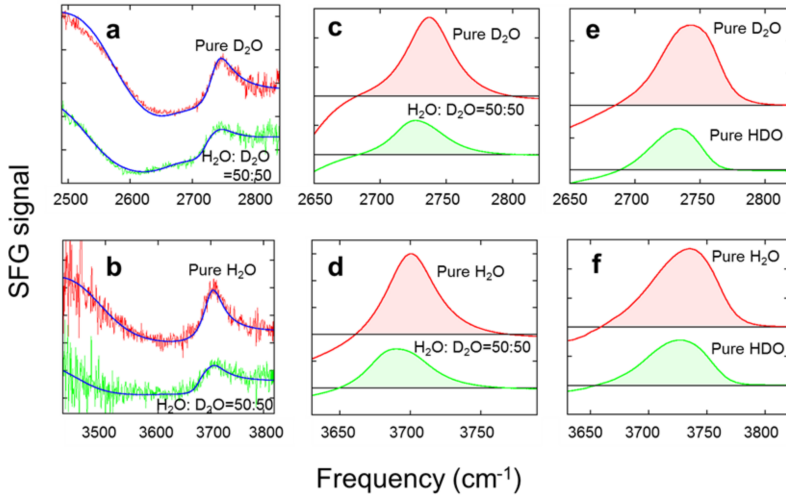
4.3   EXPERIMENT

FIGURE 4.3. (a, b) Experimentally measured SFG spectra $\left|\chi_{ssp}^{(2)}(\omega)\right|^2$ (red and green) and their fitted curves (blue), (c, d) $Im\left(\chi_{ssp}^{(2)}(\omega)\right)$ constituted by the fitted parameters, and (e, f) simulated $Im\left(\chi_{ssp}^{(2)}(\omega)\right)$. Top panels (a), (c), (e) and down panels (b), (d), (f) display the spectra in the OD and OH stretching regions, respectively. Filled areas in (c), (d), (e), and (f) represent the free OH or OD bond peak areas (see main text).

Our PIMD simulations predict that more free OH bonds than free OD bonds are present at the isotopically diluted water-vapor interface due to nuclear quantum effects. We used vibrational SFG spectroscopy to establish this enrichment of free OH bonds experimentally. As SFG is a second-order process, it is forbidden in bulk media and therefore provides an excellent tool to probe the surface

composition [25]. In our study, SFG spectra at the water-vapor interface were recorded for a range of different isotopic dilutions, two of which are plotted in figure 4.3 (a) and (b), under *ssp* polarization (SFG and visible *s* polarized, infrared *p* polarized). The free OH (OD) stretch vibration shows up in the SFG spectra of the water-vapor interface as a narrow resonant peak at ~ 3700 cm^{-1} (~ 2750 cm^{-1}) [23, 25, 77–80]. To probe the OH bond enrichment at the vapor interface, the SFG spectra for the OH and OD stretch regions were measured as a function of isotopic dilution. To decompose the SFG intensity to the free OH (OD), hydrogen bonded OH (OD), and non-resonant contributions, we fit the SFG intensities by using

$$I_{ssp}(\omega) \propto \left| \chi_{ssp}^{(2)}(\omega) \right|^2 = \left| A_{NR} e^{i\varphi_{NR}} + \sum_{i}^{n} \frac{A_i}{\omega - \omega_i + i\Gamma_i} \right|^2, \qquad (4.1)$$

where A_{NR} is the non-resonant amplitude, φ_{NR} the non-resonant phase, and A_i, ω_i, and Γ_i the peak intensity, center frequency, and width of the ith Lorentzian, respectively. Details of the fitting procedure can be found in the supporting information. The fitted curves in figure 4.3 (a) and (b) accurately reproduce the SFG spectral shapes. $Im(\chi_{ssp}^{(2)}(\omega))$ constructed from these fitting parameters are shown in figure 4.3 (c) and (d). Since $Im(\chi_{ssp}^{(2)}(\omega))$ is directly related to the spectral shape of the resonances, we used it to calculate the free OH (OD) peak area $A_{OH}(x)$ ($A_{OD}(x)$) for the concentration x of H$_2$O (D$_2$O), which was defined as the peak area of the fitted $Im(\chi_{ssp}^{(2)}(\omega))$ above a baseline defined for the OH (OD) stretch region at 3770 (2800) cm^{-1}. Subsequently, in order to enable direct comparison between the SFG experiments and the PIMD simulations, we simulated $Im(\chi_{ssp}^{(2)}(\omega))$ by using the PIMD snapshots and calculated the normalized peak areas. The simulation details are written in the supporting information. The simulated SFG spectra of H$_2$O, D$_2$O, and HDO are shown in figure 4.3 (e) and (f). Since diluted water consists of a mixture of H$_2$O, D$_2$O, and HDO, $Im(\chi_{ssp}^{(2)}(\omega))$ for the mixtures can be calculated by

$$\chi^{(2)}(\omega) = [H_2O]\chi_{H_2O}^{(2)}(\omega) + [HDO]\chi_{HDO}^{(2)}(\omega) + [D_2O]\chi_{D_2O}^{(2)}(\omega), \qquad (4.2)$$

where [H$_2$O], [D$_2$O], and [HDO] are the concentrations of H$_2$O, D$_2$O, and HDO, respectively. By utilizing the equilibrium constant $K = $ [HDO]^2/[H$_2$O][D$_2$O] of 3.86 [88], we calculated $Im(\chi_{ssp}^{(2)}(\omega))$ for different H$_2$O/D$_2$O concentrations. As with the experimental data, the normalized free OH (OD) bond peak areas, $A_{OH}(x)$ ($A_{OD}(x)$), were calculated by integrating the peak areas above the baseline $Im(\chi_{ssp}^{(2)}(\omega)) = 0$.

In figure 4.3, the experimentally obtained normalized bond areas for the different isotopic dilutions, $A_{OH}(x)/A_{OH}(x{=}1.0)$ and $A_{OD}(x)/A_{OD}(x{=}1.0)$, are plotted as squares while the simulated peak areas are represented by solid lines. Good agreement can be seen between the simulated normalized peak areas and the experimentally measured data with exceptions at the high concentration of
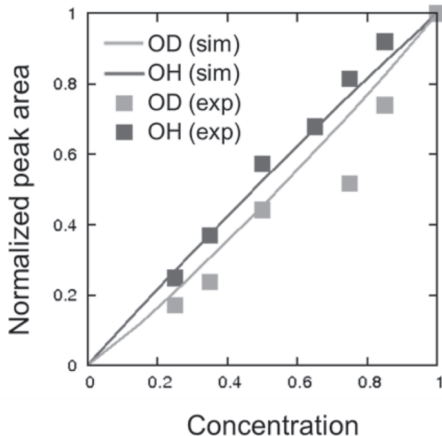
Figure 4.4.   Normalized free OH and OD bond peak areas $A(x)/A(x{=}1.0)$ as a function of the concentration x from the SFG experiments (squares) and the PIMD simulations (lines).

the OD stretch mode. For high D_2O concentration, the free D_2O shoulder peak at $\sim$2665cm^{-1} contributes to the signal, complicating the estimation of the free OD bond peak areas. Nevertheless, both the SFG spectra and the PIMD simulations indicate that the normalized free OH peak areas consistently lie above the normalized free OD peak areas. Since without distinct bond orientations SFG signals for both the free OH and OD stretches would be reduced with the concentration in the same way [23, 78], this result confirms that more free OH bonds than free OD bonds are present at the vapor interface in isotopic mixtures. Note that we assumed that the concentration of the H_2O, D_2O, and HDO is in the same manner with the bulk water in this study. We will address the isotope effect of the distribution of water species in the mixture of H_2O, D_2O, and HDO.

In summary, we have simulated the H_2O, D_2O, and HDO-vapor interfaces by using the PIMD simulations to incorporate the nuclear quantum effects explicitly. The OH bond orientation at the H_2O-vapor interface was similar to the OD bond orientation at the D_2O-vapor interfaces. In contrast, our PIMD simulations indicate that the OH and OD bonds have distinct orientation at the HDO-vapor interface; the OD bond tends to orient toward the bulk region, while the OH bond tends to orient toward the vapor region. This distinct OH and OD bond orientations have been identified by experimentally observed SFG spectra and the simulated SFG spectra from the PIMD simulations. The current study confirms that nuclear quantum effects generate distinct OH and OD bond orientations at the water-vapor interface and indicates that nuclear quantum effects are non-negligible for quantitative analyses in interface-specific studies, e.g. SFG at isotopic diluted samples.

4.4   Supporting information

Simulated density profile

The density profiles of H_2O, D_2O, and HDO are shown in figure 4.4. The Gibbs dividing surface is located at $|z| = 6.8$. All the density profiles are identical after rescaling molecular masses.
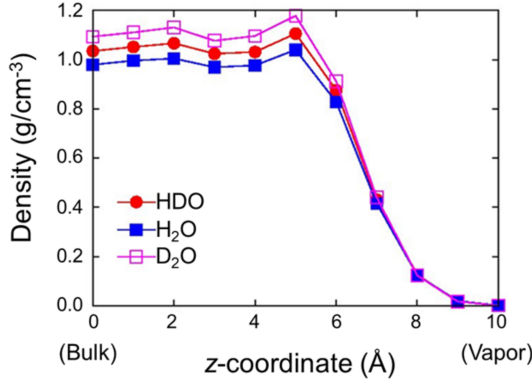

Figure 4.5. Axial distribution of the density at HDO, H_2O, and D_2O-vapor interfaces. Lines are guides for the eye.

Temperature dependence for the orientation distribution

The temperature dependence of the OH and OD orientations were surveyed, by performing PIMD simulation for the HDO-vapor interface at 285, 300, and 315K. The results are summarized in figure 4.4. This figure shows that the distinction of the OH and OD bond orientations are enhanced at lower temperatures at the vapor interface. The nuclear quantum effect is enhanced at the lower temperature [89], and one can expect that the enhanced difference of the OH and OD bond orientations due to the nuclear quantum effect is also enhanced at lower temperature. This figure is consistent with the nature of the nuclear quantum effect.

Entropy calculation from the distribution of $\cos\theta$

The normalized distribution of $\cos\theta$ for each layer is displayed in figure 4.4. The entropy can be calculated

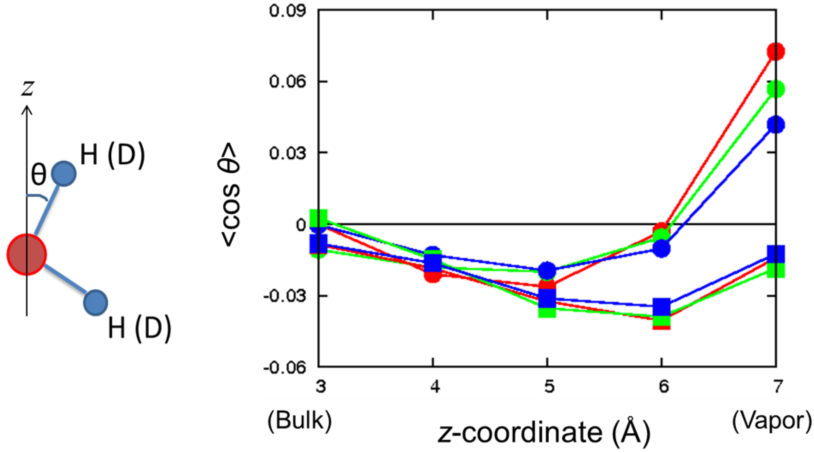$$S = -k_B \sum_i p_i \ln p_i \qquad (4.3)$$

FIGURE 4.6. (Left) Pictorial representation of the angle θ between the OH (OD) bond and the surface normal. (Right) Axial distribution of average angles $\langle \cos\theta \rangle$ at 285 K (red), 300 K (green), and 315 K (blue). Lines are guides for the eyes. The filled circles and squares denote the angles associated with the OH and OD bonds, respectively.

where p_i is the probability for $\cos\theta$. S_2 is the entropy for the OH and OD bond orientations of HDO obtained from our PIMD simulation. S_2 for one HDO molecule can be calculated

$$S_2 = -k_B \left(\sum_i p_i^{OH} \ln p_i^{OH} + \sum_i p_i^{OD} \ln p_i^{OD} \right) \quad (4.4)$$

S_1 is the entropy by assuming that the OH and OD bond orientations are the same. S_1 is, thus, given by

$$S_1 = -2k_B \sum_i \frac{p_i^{OH} + p_i^{OD}}{2} \ln \frac{p_i^{OH} + p_i^{OD}}{2} \quad (4.5)$$

The entropy decreases due to the distinct bond orientations, $\Delta S = S_2 - S_1$, was calculated from p_i^{OH} and p_i^{OD} given in figure 4.4. The depth profile of $T\Delta S/k_b$ is shown in the inset of figure 4.4.

SFG SPECTRAL CALCULATION FROM PIMD

We simulated the free OH and OD stretch regions of the SFG spectra at the H_2O, D_2O, and HDO-vapor interfaces by using the snapshots obtained from our PIMD simulation. In the homogeneous limit, the resonant part of the x-directed SFG response function generated by the z-directed infrared (IR) and x-directed visible pulses can be written
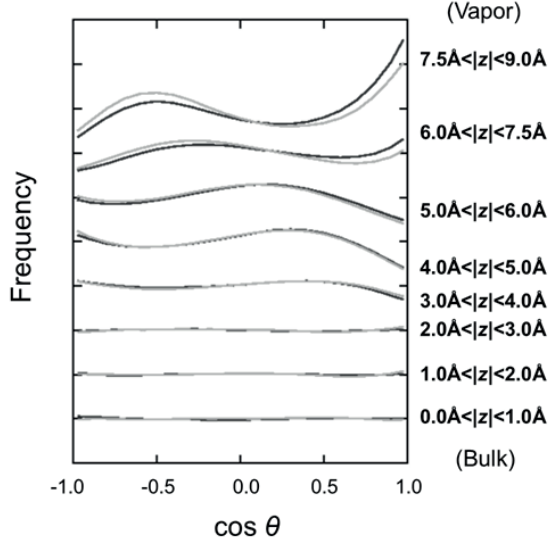
FIGURE 4.7. Normalized distribution of $\cos\theta$ for the OH bond (dark grey) and OD bond (light grey).

$$\chi^{(2)}_{xxz}(\omega) = \sum_n \left\langle \frac{a_{n,xx}(0)m_{n,z}(0)}{\omega_n(0) - \omega - i/2T_1} \right\rangle, \tag{4.6}$$

where $a_{n,xx}(0)$, $m_{n,z}(0)$, and $\omega_n(0)$ is the xx-tensor element of the transition polarizability, the z-component of the transition dipole moment, and the transition frequency of chromophore n, respectively [90–92]. Note that $\chi^{(2)}_{ssp}(\omega) \propto \chi^{(2)}_{xxz}(\omega)$ [66]. The excited vibrational lifetime T_1 was set to 1.3 ps [90, 93]. The z-component of the transition dipole moment can be written as

$$m_z = \mu' x_{10} \vec{u}_{bond} \cdot \vec{u}_z, \tag{4.7}$$

where μ' is the magnitude of the dipole derivative, x_{10} is the 1-0 matrix element of the OH stretch coordinate, $\vec{u}_{bond}$ is the OH or OD bond unit vector, and $\vec{u}_z$ is the surface normal unit vector [90]. Similarly, the xx-tensor of the transition polarizability can be given by

$$a_{xx} = x_{10} \left((\alpha'_{||} - \alpha'_{\perp})(\vec{u}_{bond} \cdot \vec{u}_x)^2 + \alpha'_{\perp} \right), \tag{4.8}$$

where $\alpha'_{||}$ and $\alpha'_{\perp}$ are the magnitudes of the polarizability derivatives parallel and perpendicular to the OH bond, respectively [90]. μ', $\alpha'_{||}$, $\alpha'_{\perp}$, x_{10}, and ω have been parameterized as a function of the electric field, E, along the OH (OD) bond at H (D) atom [90, 93]. We set $\alpha'_{||}/\alpha'_{\perp} = 5.6$ [90]. E was calculated from all the water molecules within 6.6 by setting the SPC/E point charges to

the geometries obtained from our PIMD simulation. Note that we assume that the difference of the equilibrated structures between the SPC/E and q-SPC/Fw models is tiny and the electrostatic map for the SPC/E model can be applied for the geometry obtained from our PIMD simulations with the q-SPC/Fw water model. The intramolecular coupling shifts the frequencies of the OH (OD) stretching modes in H_2O-vapor and D_2O-vapor interfaces. The intramolecular coupling ω_{12} can be calculated from ref. [79]. The frequency shift due to the intramolecular coupling is given by [80]

$$\Delta = \sqrt{\frac{(\omega_1 - \omega_2)^2}{4} - \omega_{12}^2} - \frac{|\omega_1 - \omega_2|}{2} \tag{4.9}$$

Then, the stretching frequencies are given by $\omega_1 + \Delta$ and $\omega_2 - \Delta$ for $\omega_1 > \omega_2$, and $\omega_1 - \Delta$ and $\omega_2 + \Delta$ for $\omega_1 < \omega_2$ for each water molecule.

Experimental setup

In the SFG experiments, 1 mJ of the output of a regeneratively amplified Ti: sapphire system (Spitfire Ace, Spectra Physics, Inc.) producing ˜35 fs pulses centered at 800 nm was used to generate tunable mid-IR pulses using a home-built optical parametric amplifier and difference frequency generation unit [68]. 0.5 mJ of the amplifier output was spectrally narrowed to ˜15 cm^{-1} using a Fabry-Perot etalon. The IR beam passes through a half wave plate and polarizer before being focussed onto the sample together with this spectrally narrowed visible beam. A focal length of 50 mm and 200 mm were used in this reflection geometry, with angles of incidence of 45° and 40° with respect to the surface normal and a remaining power of 5 mW and 25 mW (IR and visible, respectively). The SFG signal was focused into a spectrograph (Acton, Princeton Instruments) in which it was dispersed, via a grating, and focused onto an electron multiplied Charge Coupled Device (emCCD) camera (Newton, Andor). All spectra reported in this study were collected under the *ssp*-polarization condition (SFG and visible *s*, IR *p* polarizations). The measured SFG spectra are shown in figure 4.4.

Fitting procedure of the SFG signal

As described in the main text, the SFG spectra were fitted with a Lorentzian lineshape model. We fitted spectra from 2490 to 2840 cm^{-1} for the OD stretch region and from 3420 to 3820 cm^{-1} for the OH stretch region. A_{NR} and φ_{NR} were kept constant throughout the fits of all spectra, both in the OH and OD region. To fit the OH stretch region three Lorentzians were used. Two positive peaks corresponding to the free OH bonds of HDO and H_2O molecules make up the free OH itself, largely overlapping with central frequencies of 3682 cm^{-1} and 3700 cm^{-1}, respectively. The third negative peak corresponds to the H-bonded OH stretch frequency around 3450 cm^{-1}. With these three resonances, an accurate fit of the experimental data could be achieved for all isotopic dilutions (see figure 4.4). The amplitudes of the two free OH (OD) stretch peaks overlap,
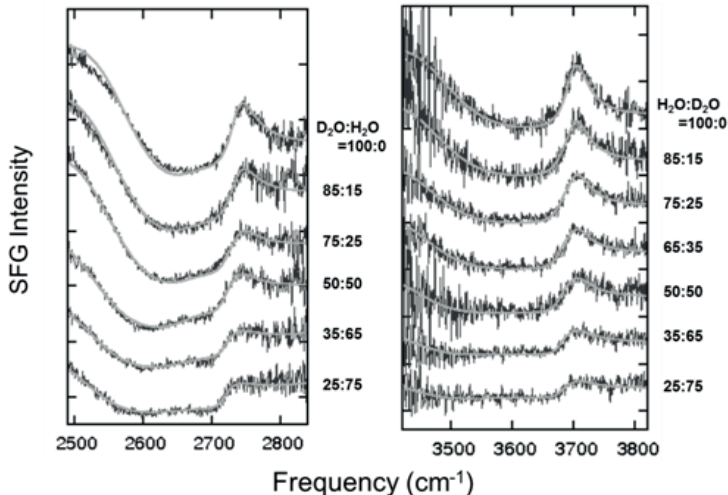
FIGURE 4.8. Experimentally measured SFG spectra (dark grey) and Lorentzian model fits (light grey). Left and right panels display the OD and OH stretch regions, respectively. Isotope dilution ratios are indicated in the plot.

making them to a large extent exchangeable in the fittings. However, since we are interested in the peak areas of the free OH (OD) stretch peak, only the sum of these contributions to the SFG spectra are necessary to identify the distinct bond orientations. The peak area was insensitive to these exchanges.

In the OD stretch region, three analogous resonances were fitted to the data: the negative hydrogen bonded OD around 2550 cm^{-1}, the positive free HDO at 2722 cm^{-1} and the positive free D_2O at 2737 cm^{-1}. However, two additional peaks were needed to fit the data with equal accuracy. Firstly, the negative H-bonded OH peak, although lying outside the scope of our experimental data, was added to the fitting expression because the red tail of the resonance was found to influence the free OD stretch region, especially for low OD:OH dilutions. Secondly, a broad feature at 2665 cm^{-1} (free D_2O shoulder peak) was evident in the OD data. This peak has been described previously [80].

In fitting the data, all center frequencies and widths were fixed, except for the H-bonded OH and OD frequencies. These were slightly shifted to lower frequency with increasing HDO, which has been reported in previous studies [24, 94]. It should be noted that the exact fitting results and the obtained areas of the free OH (OD) peak plotted in figure 4.3 of the main text depend subtly on the starting choice of fitting parameters. However, the OD data points lie below the OH points for all different fitting attempts. Fitting parameters are summarized in Table S1 and S2. All the fitted curves are shown in figure 4.4 along with the measured SFG spectra. The signs of the different peaks have been obtained from ref. [23, 94].

We would like to note that fitting the data with a series of Lorentzians helps

in identifying the spectral overlaps, but the need for a non-resonant background and phase term introduces uncertainty to the fitting process. To bypass the uncertainty of the fitting procedure, the results were reproduced by means of an alternative experimental method. By increasing the delay between the infrared and visible pulse, the short-lived non-resonant background and broad spectral features originating from the hydrogen bonded OH (OD) stretching mode are suppressed, leaving only the narrow, longer-lived free mode remaining. This method has been previously applied by Stiopkin *et al.* [80]. The area of the remaining free OH (OD) peak is proportional to the square of the free OH (OD) bond peak areas. Using this method, the nuclear quantum effects were qualitatively reproduced. The downside of this method is a decrease of the signal-to-noise ratio, increasing the uncertainty of extracted resonance intensities. Moreover, as the lifetime of the OH and OD are different [95], there is an intrinsic error in this procedure.

Parameter	H100	H85	H75	H65	H50	H35	H25
NR amplitude	-0.053	-0.053	-0.053	-0.053	-0.053	-0.053	-0.053
NR phase	-0.4	-0.4	-0.4	-0.4	-0.4	-0.4	-0.4
HB OH amplitude	-9.51	-8.56	-7.14	-6.52	-4.77	-3.16	-2.48
HB OH frequency	3475	3465	3360	3455	3445	3440	3435
HB OH width	110	110	110	110	110	110	110
Free HDO amplitude	0	0.200	0.278	0.350	0.341	0.250	0.150
Free HDO frequency	3682	3682	3682	3682	3682	3682	3682
Free HDO width	18	18	18	18	18	18	18
Free H_2O amplitude	1.684	1.301	1.013	0.719	0.519	0.310	0.228
Free H_2O frequency	3700	3700	3700	3700	3700	3700	3700
Free H_2O width	23	23	23	23	23	23	23

TABLE I. Fitting parameters for the OH stretch region. Phases are in radians, while frequencies and widths are expressed in cm^{-1}.

Parameter	D100	D85	D75	D50	D35	D25
NR amplitude	-0.045	-0.045	-0.045	-0.045	-0.045	-0.045
NR phase	-0.4	-0.4	-0.4	-0.4	-0.4	-0.4
HB OD amplitude	-6.77	-5.96	-5.28	-3.76	-2.58	-2.24
HB OD frequency	2565	2550	2545	2535	2528	2523
HB OD width	100	100	100	100	100	100
Free D_2O shoulder amplitude	1.218	0.748	0.498	0.384	0.150	0.003
Free D_2O shoulder frequency	2665	2665	2665	2665	2665	2665
Free D_2O shoulder width	55	55	55	55	55	55
Free HDO amplitude	0	0.050	0.105	0.155	0.114	0.113
Free HDO frequency	2722	2722	2722	2722	2722	2722
Free HDO width	18	18	18	18	18	18
Free D_2O amplitude	0.749	0.526	0.336	0.174	0.083	0.053
Free D_2O frequency	2737	2737	2737	2737	2737	2737
Free D_2O width	23	23	23	23	23	23
HB OH amplitude	0	-2.25	-3.51	-5.02	-6.11	-7.35
HB OH frequency	3425	3430	3435	3445	3450	3455
HB OH width	110	110	110	110	110	110

TABLE II. Fitting parameters for the OD stretch region. Phases are in radians, while frequencies and widths are expressed in cm^{-1}.

5   Phase-Specific Sum-Frequency Generation Spectroscopy

In the previous chapter we discussed fundamental physics at the interface; in this chapter we explore the fundamental principles behind our spectroscopic methodology. In recent years, phase-specific sum-frequency generation (PS-SFG, also known as heterodyne-detected SFG) spectroscopy has been increasingly replacing its predecessor (which to distinguish it we will here name direct SFG, or homodyne SFG) as the experimental technique of choice for characterizing interfacial structure. The technique enables phase-specific measurements, allowing for the determination of the real and imaginary parts of the interfacial vibrational response function and thereby the unambiguous identification of molecular orientation. This phase-sensitivity requires, however, a complete understanding of the complex optical properties of the sample, and of their effect on the signal. These optical properties significantly influence the raw spectral data from which the real and imaginary parts of the second-order susceptibility are retrieved. We show that it is essential to correct the data appropriately to correctly infer the true molecular response. This chapter presents a detailed description of the physical contributions to the phase-resolved spectrum, allowing a direct comparison between the phase-resolved spectrum and that obtained using the well-understood direct detection method, in a step-by-step data analysis process. In addition to phase sensitivity, PS-SFG has been shown to increase the sensitivity compared to traditional (direct) SFG spectroscopy. We present a quantitative comparison between theoretical limits of the signal-to-noise ratio of both techniques, which shows that for many systems the signal-to-noise ratio is very similar for direct- and phase-specific SFG signals.

5.1 Introduction

Vibrational sum frequency generation (SFG) spectroscopy is in many ways an ideal technique for probing the structure of interfaces at the molecular level. As with infrared spectroscopy, vibrational modes are interrogated by an infrared laser source of resonant frequency ω_1 in order to identify the spectral signatures

of the molecular moieties present. In SFG spectroscopy a second, non-resonant laser with (generally) near-infrared frequency ω_2 is overlapped in time and space with the first one, upconverting the vibrational polarization into the visible region, through a virtual state. Emission from this state at frequency $\omega = \omega_1 + \omega_2$ lies well within the visible optical region and can therefore be detected background-free and sensitively by commercially available CCD cameras. The true strength of SFG spectroscopy, however, lies in the surface specificity of the technique. Since the instantaneous excitation and upconversion of molecular vibrations is a two-photon process, the intensity of the sum-frequency emission is determined by the second-order nonlinear susceptibility $\chi^{(2)}$ of the sample and the strength of the incoming visible and infrared fields:

$$I_{\text{SFG}} = |E_{\text{SFG}}|^2 \propto \left| \chi^{(2)} E_{\text{VIS}} E_{\text{IR}} \right|^2 I_{\text{SFG}} = |E_{\text{SFG}}|^2 \propto \left| \chi^2 E_{\text{VIS}} E_{\text{IR}} \right|^2 \qquad (5.1)$$

The molecular information contained in the detected SFG spectrum thus originates from $\chi^{(2)}$, being the macroscopic average of the molecular hyperpolarizability. For a centrosymmetric medium, which most bulk materials are, $\chi^{(2)}$ cancels out in the dipole approximation and no SFG signal is generated from the bulk. Only when the symmetry is broken, e.g. at an interface, the sum-frequency field becomes finite. It is this surface specificity that sets SFG spectroscopy apart from other infrared techniques by enabling detection of water, surfactants and surface-bound peptides and proteins at the interface that would otherwise be indiscernible from the typically much larger bulk signal. For this reason the technique has become very popular since its first application approximately two decades ago [27, 40, 96–102]. On the other hand, it can be argued that SFG spectroscopy has not yet reached its full potential because of a lack of uniformity in the presentation of data: to extract $\left| \chi^{(2)} \right|^2$ from the detected intensity, corrections need to be made for the Fresnel factors that depend on the specific geometric of the setup – a practice that is not always explicitly described. The inconsistencies thus arising in spectra of, for example, the air-water interface were recently addressed and shown to be converging to an accepted standard [20].

A more fundamental shortcoming of the technique lies in the detection of the squared term $|\chi^{(2)}|^2$ (see equation 5.1), whereby all information on the complex nature of $\chi^{(2)}$ is lost. This drawback can be circumvented by the application of an interference-based phase-specific SFG (PS-SFG) detection scheme, as was initially demonstrated by the group of Shen [103], and subsequently by several other groups [33–35]. With this approach one can obtain phase-specific spectra. By mixing the sample signal with a local oscillator (LO) of known phase, the detected intensity does not only contain the squared field strengths, but also two cross terms:

$$\begin{aligned} I = \left| E_{/textdet} \right|^2 &= |E_{\text{LO}} + E_{\text{sample}}|^2 \\ &= |E_{\text{LO}}|^2 + \left| E_{\text{sample}} \right|^2 + E_{\text{LO}} E_{\text{sample}}^* + E_{\text{LO}}^* E_{\text{sample}} \end{aligned} \qquad (5.2)$$

From these cross terms, the complex $\chi^{(2)}$ can be extracted, as the cross terms contain the phase information of the resonances that is lost in more conventional direct SFG measurements. The imaginary part of $\chi^{(2)}$, Im $\chi^{(2)}$, shows the vibrational resonances, and can be thus directly compared to what is measured in a linear IR absorption measurement. However, these resonant peaks can be either positive or negative in the Im $\chi^{(2)}$ of an PS-SFG spectrum, and it is this phase of the vibration that is indicative of the direction of the aligned molecules, making it possible to distinguish 'up'-pointing molecular bonds from 'down'-pointing ones [32]. This additional information on interfacial molecular structure makes the potential of PS-SFG even larger than that of its direct counterpart, and promising results have been published using several forms of the technique [33–36, 42, 103]. Several authors have used the term 'heterodyne SFG' to indicate this novel technique, and 'homodyne' for the direct SFG approach. This nomenclature is technically not correct, since heterodyning implies interference with a local oscillator of a different frequency to frequency-shift the detected signal. PS-SFG is therefore strictly speaking a homodyne technique, but to avoid further confusion we refrain from using either term altogether, and refer here to phase-resolved and direct SFG.

The benefits of phase-resolved SFG come at a price: extracting the complex $\chi^{(2)}$ from the measured intensity spectrum is less straightforward than finding $|\chi^{(2)}|^2$. In the latter case, only the Fresnel factors need to be corrected for, which determine the local field effects of IR, VIS and SFG field in dependence of the particular angles of incidence, polarizations, and the resulting phase matching conditions [63]. In the PS-SFG case however, additional corrections are needed to find the true real and imaginary parts of $\chi^{(2)}$. Firstly, a z-cut quartz crystal is generally used as a nonresonant reference to obtain the infrared spectral shape. The use of such a reference is traditionally thought to require a correction of the complex phase of 90 degrees because of the mismatch between the bulk-like response of the quartz reference and the surface-like response of aqueous interfaces [104, 105], although more recent measurements suggest a correction closer to 115 degrees [106]. Further, in most experimental geometries, either the visible and infrared pulse generating the LO [34, 35] or the LO itself [33, 103] are reflected from the sample. The complex reflection coefficient of the sample (of water, for example) may greatly influence the spectral shape of both the SFG intensity and phase, as will be demonstrated below. Finally, a seemingly trivial but important source of phase aberrations originates from the challenge in maintaining phase stability of the experimental setup.

As a result of these challenges, there is no complete consistency between different phase-detected studies [20, 107]. Specifically, details of the sign and the zero-crossing point of the imaginary spectrum have remained debated [20, 107], which may lead to varying interpretations of molecular structure at the interface. Apparently, the corrections described above for retrieving the complex $\chi^{(2)}$ from the phase-resolved measurements are not yet fully understood or universally applied.

In this study, we present phase-resolved and direct measurements of lipid monolayers of positive and negative charge on water. We record the SFG spec-
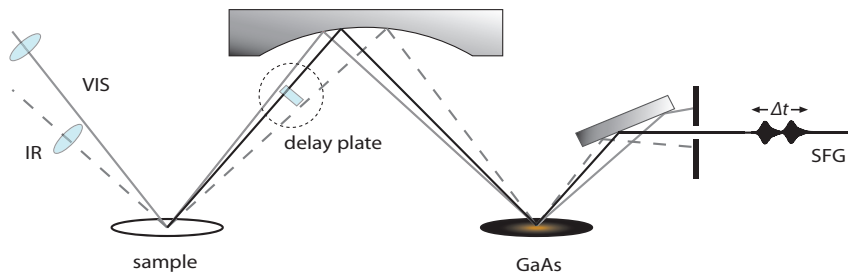
FIGURE 5.1. Experimental geometry of PS-SFG detection. 800 nm (VIS) and mid-infrared (IR) laser pulses are focused onto the aqueous interface of the sample, generating an SFG response that is delayed by a silica plate. The three beams are refocused by a spherical mirror onto a gallium arsenide (GaAs) wafer, generating a second SFG response that interferes with the sample signal on the CCD.

tra across the lipid CH and water OH resonances. We explicitly show all the steps of PS-SFG data analysis, including the application of the aforementioned corrections in amplitude and phase and compare direct SFG and PS-SFG measurements in order to show the implications of these corrections. In this way, we hope to promote reproducibility and consistency between the many results that are certain to come from PS-SFG spectroscopy.

5.2   Materials and methods

The experimental setup used to perform PS-SFG measurements is largely based on that developed by the Tahara group 13. 1 mJ of the output of a regeneratively amplified Ti: sapphire system (Legend, Coherent, Inc.) producing ∼35 fs pulses centered at 800 nm is used to generate tunable mid-IR pulses using a homebuilt optical parametric amplifier and difference frequency generation unit. 0.5 mJ of the amplifier output is spectrally narrowed to ∼25 cm^{-1} using a Fabry-Perot etalon. The IR beam passes through a half wave plate and polarizer before being focussed onto the sample together with the spectrally narrowed visible beam. A focal length of 50 mm and 200 mm are used in this reflection geometry, with angles of incidence of 45° and 40° with respect to the surface normal and a remaining power of 5 mW and 25 mW (IR and visible, respectively; see figure 5.1). The SFG signal generated in this way passes through a silica delay plate (1 mm, with antireflection coating) and is refocused, together with the reflected IR and visible pulses, onto a 110 gallium arsenide wafer (GaAs, 110 cut, from which the LO is generated) by means of a gold-coated spherical mirror with a focal length of 150 mm.

The remaining 800 nm light is filtered out and the SFG signal is passed through a polarizer and focused into a spectrograph (Acton, Princeton Instruments) in which it is dispersed, via a grating, and focused onto an electron multiplied Charge Coupled Device (emCCD) camera (Newton, Andor). All spectra
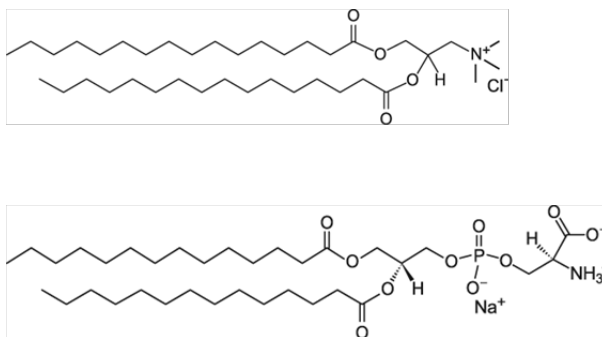
FIGURE 5.2. Chemical structure of DPTAP (top) and DMPS (bottom). Their net positive and negative charge will result in alignment of the water with hydrogen atoms down and up, respectively. It is this phase of the vibration that can be identified through PS-SFG spectroscopy.

reported in this study were collected under the ssp polarization condition (s polarized sum frequency, s polarized visible, p polarized IR). All measurements were conducted at 23 °C. Direct measurements were performed by blocking the IR between the sample and GaAs. Note that the reflectivity of GaAs is low in this geometry (< 0.4), causing a significant loss in SFG signal strength. The reflection coefficient is, however, wavelength independent, ruling out the danger of spectral distortion.

To extract the true phase of $\chi^{(2)}$ from the PS-SFG measurements, the height and angular placement of the quartz reference and the aqueous sample have to be highly reproducible. To this end, a diode laser pointer was reflected off the sample site and projected in the far field onto a millimetre grid. Monitoring both the position of the reflected laser light on the grid and the position of the SFG signal on the CCD camera enabled for a reproducibility of the phase of the quartz and lipid samples within 3.

Cationic 1,2-dipalmitoyl-3-trimethylammonium-propane (DPTAP) and anionic 1,2-dimyristoyl-sn-glycero-3-phospho-L-serine (DMPS) were obtained from Avanti Polar Lipids; their chemical structures are shown in figure 5.2. Self-assembled monolayers were produced by dropcasting a solution of this lipid in chloroform (1 g/L) drop by drop onto a pure H_2O subphase. H_2O used in this study was demineralised and then filtered using a Millipore unit to a final resistivity of 18 MΩ cm. Samples were prepared in a 70 mm by 70 mm Teflon-coated aluminium trough (approximately 20 mL). The experiments were performed at a surface pressure of 22 ± 2 mN/m, measured with a commercially available tensiometer (placeCityKibron, country-regionFinland).

5.3   EXPERIMENT AND ANALYSIS: AMPLITUDE AND PHASE CORRECTIONS

In broadband frequency-domain SFG spectroscopy, the nonlinear response of a surface is induced by overlapping a broadband infrared (IR) and a narrowband visible (placeVIS) pulse in both time and space. In PS-SFG spectroscopy, this signal is mixed with a local oscillator of independent phase. For instance, the reflected VIS and IR and the generated SFG beams can be refocused on a medium with a frequency independent (i.e. non-resonant) second-order nonlinear response, e.g. GaAs, on the surface of which the local oscillator (LO) is then generated. The detected field E_{det} is the sum of the contribution from the LO (E_{LO}) and that of the sample (E_{sample}), reflected from the GaAs wafer:

$$E_{\text{det}} = E_{\text{LO}} + r_{\text{GaAs}} E_{\text{sample}} \tag{5.3}$$

where r_{GaAs} is the reflection coefficient of the local oscillator medium.

The contributions of the sample and the LO are defined by the vacuum permittivity (ε_0), the geometry- and material-specific Fresnel factors (F), the second-order nonlinear susceptibility ($\chi^{(2)}$), and the incoming visible and IR fields (E_{VIS} and E_{IR}), taking into account that these are reflected by the sample before reaching the GaAs:

$$
\begin{aligned}
E_{\text{sample}} &= \varepsilon_0 F_{\text{sample}} \chi^2_{\text{sample}} E_{\text{VIS}} E_{\text{IR}} \\
E_{\text{LO}} &= \varepsilon_0 F_{\text{GaAs}} \chi^2_{\text{GaAs}} r_{\text{sample}} \left(\omega_{\text{VIS}} \right) r_{\text{sample}} \left(\omega_{\text{IR}} \right) E_{\text{VIS}} E_{\text{IR}}
\end{aligned}
\tag{5.4}
$$

$\chi^{(2)}{}_{sample}$ is the quantity of interest, as it contains the molecular response and we aim to extract this quantity from the collected spectrum. Therefore, we focus below on cancelling out the other factors. Keeping in mind that E_{LO} is dependent on the incoming infrared and visible field and therefore on the reflectivity of the sample, it will be referred to as $E_{\text{LO,s}}$ — this quantity differs from the local oscillator field obtained if the incident infrared and visible beams had not been first reflected off the sample. To obtain the spectral shape of the original IR excitation pulse required for the normalization of the sample spectrum, the sample is replaced by quartz, which is also a non-resonant material and gives a response E_{quartz}. The LO that is generated after reflection of the IR and placeVIS on quartz shall be referred to as $E_{\text{LO,q}}$.

The detected intensity is the square of the sum of all field strength contributions. In direct SFG spectroscopy only the sample field E_{sample} contributes, causing the signal to be squared in its entirety and thereby losing all phase information. In PS-SFG spectroscopy, phase information is preserved within the linear cross-terms of the intensity of a signal composed of contributions of several sources (equation 5.2). These cross terms are extracted from the total intensity by introducing a controllable delay between the SFG response of the sample and that of the LO, as is explained below.

According to Fourier theory, a delay Δt of the SF response of the sample relative to that of the LO results in an exponential prefactor in the frequency domain:

$$E_{\text{det}}(t) = E_{\text{LO}}(t) + r_{\text{GaAs}}E_{\text{sample}}(t - \Delta t)$$
$$\rightarrow E_{\text{det}}(\omega) = E_{\text{LO}}(\omega) + r_{\text{GaAs}}E_{\text{sample}}(\omega)e^{(i\omega\Delta t)} \tag{5.5}$$

With this delay, the intensity spectrum detected on the CCD camera is given by:

$$I = |E_{\text{det}}|^2 = \left| E_{\text{LO}} + r_{\text{GaAs}}E_{\text{sample}}e^{(i\omega\Delta t)} \right|^2$$
$$= |E_{\text{LO}}|^2 + \left| r_{\text{GaAs}}E_{\text{sample}} \right|^2 \tag{5.6}$$
$$+ E_{\text{LO}}r_{\text{GaAs}}^*E_{\text{sample}}^*e^{(-i\omega\Delta t)} + E_{\text{LO}}^*r_{\text{GaAs}}E_{\text{sample}}e^{(i\omega\Delta t)}$$

In figure 5.3 this composed intensity is shown for a quartz reference and lipid (DPTAP) monolayer sample. The exponential delay term gives rise to fringes on the spectrum. They are much smaller for the sample than for quartz, displaying that the quartz response is of comparable size to the LO, whereas the response of this aqueous interface is much smaller. Linear terms are extracted from this composed intensity spectrum by taking the inverse Fourier transform (using an IFFT algorithm), resulting in a time-domain spectrum with the sum of the two quadratic terms at t = 0 and the two delayed terms on either side of this peak (figure 5.4). The delayed term at t = 1.6 ps contains the unaltered E_{sample} whereas the term at t = -1.6 contains its complex conjugate; these are the fourth and third terms, respectively, of the right-hand side of equation 5.6. The positively delayed term is selected by setting the values of the Fourier transforms outside the window shown in Fig. 4 to zero and transforming back to the frequency domain by taking the Fourier transform. We are left with the complex cross term, shown graphically and algebraically in figure 5.5.

If we consider the two terms shown in figure 5.5, it is evident that dividing these two terms cancels out the exponential term introduced by the delay and the reflection coefficient of the local oscillator. What we are then left with is one of the two linear cross terms from the total detected intensity (equation 2) normalized to account for the spectral shape of the IR excitation. In analogy with normalized direct SFG spectra, we may refer to this quantity as the extracted PS-SFG intensity I_{PS}:

$$I_{\text{PS}} \equiv \frac{E_{\text{LO,s}}^*r_{\text{GaAs}}E_{\text{sample}}e^{(i\omega\Delta t)}}{E_{\text{LO,q}}^*r_{\text{GaAs}}iE_{\text{quartz}}e^{(i\omega\Delta t)}} = \frac{E_{\text{LO,s}}^*E_{\text{sample}}}{E_{\text{LO,q}}^*iE_{\text{quartz}}} \tag{5.7}$$

Note that we have also inserted a factor i here to account for the 90° phase difference between the SFG response of the aqueous interface of the sample and the quartz crystal [104, 105], noting that the exact value of this correction is under debate [20, 106]. Substituting equation 5.4 into this expression results in:
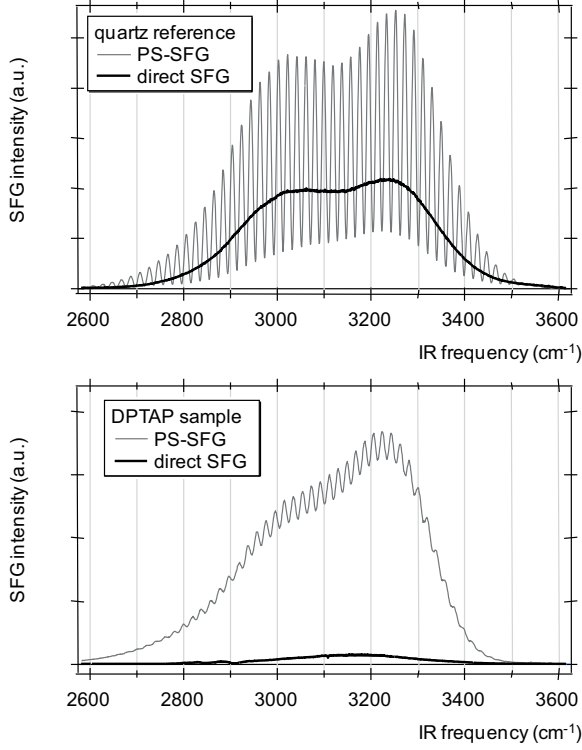
FIGURE 5.3. Binned intensity spectra of the quartz reference (top) and sample (bottom). The quartz reference has an SFG response that is comparable in magnitude to the local oscillator in the PS-SFG measurements, causing strong interference and thus deep fringes. The lipid sample signal is much lower than the local oscillator, as can be seen by the narrow fringes. The direct SFG sample signal is two orders of magnitude smaller.

$$
\begin{aligned}
&\frac{E_{\text{LO,s}}^* E_{\text{sample}}}{i E_{\text{LO,q}}^* E_{\text{quartz}}} \\[2mm]
&= \left(\frac{\varepsilon_0 F_{\text{GaAs}} \chi_{\text{GaAs}}^{(2)} r_{\text{sample}} \left(\omega_{\text{VIS}} \right) r_{\text{sample}} \left(\omega_{\text{IR}} \right) E_{\text{VIS}} E_{\text{IR}}}{\varepsilon_0 F_{\text{GaAs}} \chi_{\text{GaAs}}^{(2)} r_{\text{quartz}} \left(\omega_{\text{VIS}} \right) r_{\text{quartz}} \left(\omega_{\text{IR}} \right) E_{\text{VIS}} E_{\text{IR}}} \right)^* \\[2mm]
&\quad \times \frac{\varepsilon_0 F_{\text{sample}} \chi_{\text{sample}}^{(2)} E_{\text{VIS}} E_{\text{IR}}}{i \varepsilon_0 F_{\text{quartz}} \chi_{\text{quartz}}^{(2)} E_{\text{VIS}} E_{\text{IR}}} \\[2mm]
&= \left(\frac{r_{\text{sample}} \left(\omega_{\text{VIS}} \right) r_{\text{sample}} \left(\omega_{\text{IR}} \right)}{r_{\text{quartz}} \left(\omega_{\text{VIS}} \right) r_{\text{quartz}} \left(\omega_{\text{IR}} \right)} \right)^* \frac{F_{\text{sample}} \chi_{\text{sample}}^{(2)}}{i F_{\text{quartz}} \chi_{\text{quartz}}^{(2)}}
\end{aligned}
\tag{5.8}
$$

Clearly, all terms cancel out except for the reflection coefficients r, the Fres-
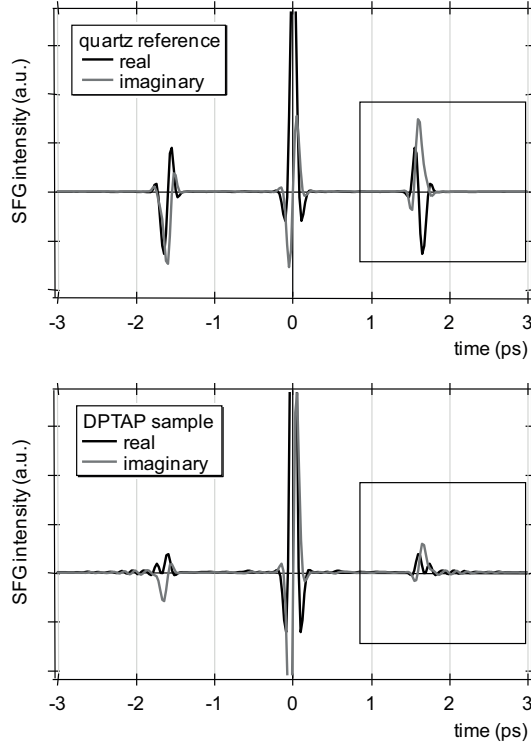
FIGURE 5.4. Inverse Fourier transforms of the spectra shown in figure 5.3 (top quartz, bottom sample). The sum of the two quadratic terms of equation 5.6 at t = 0 are flanked by the two delayed cross terms at $-\Delta t$ and Δt. The framed area shows the window of data that is selected; i.e. all other values are set to zero before Fourier-transforming back to the frequency domain.

nel factors F and the second-order non-linear susceptibilities χ, each of them different for the sample than for quartz. Since quartz is nonresonant, $\chi^{(2)}_{\mathrm{quartz}}$ is constant (i.e. frequency independent), and $\chi^{(2)}_{\mathrm{sample}}$ can be extracted from this expression by inserting r and F. Traditionally, for direct SFG spectra a correction for F is rarely made, that is, the presented direct SFG spectra are often not corrected for the Fresnel factors; if we proceed with the PS-SFG spectra along the same line, only the reflectivity of the sample and of quartz have to be considered. To show that we are indeed able to extract $F_{\mathrm{sample}}\chi^{(2)}_{\mathrm{sample}}$ correctly by means of this procedure, we compare $|F_{\mathrm{sample}}\chi^{(2)}_{\mathrm{sample}}|^2$ acquired by direct detection with the magnitude squared of $F_{\mathrm{sample}}\chi^{(2)}_{\mathrm{sample}}$ as obtained by PS-SFG. Let us briefly review the direct detection case, where the detected field is simply E_{sample}, and the detected intensity after normalization by the quartz reference is given by:
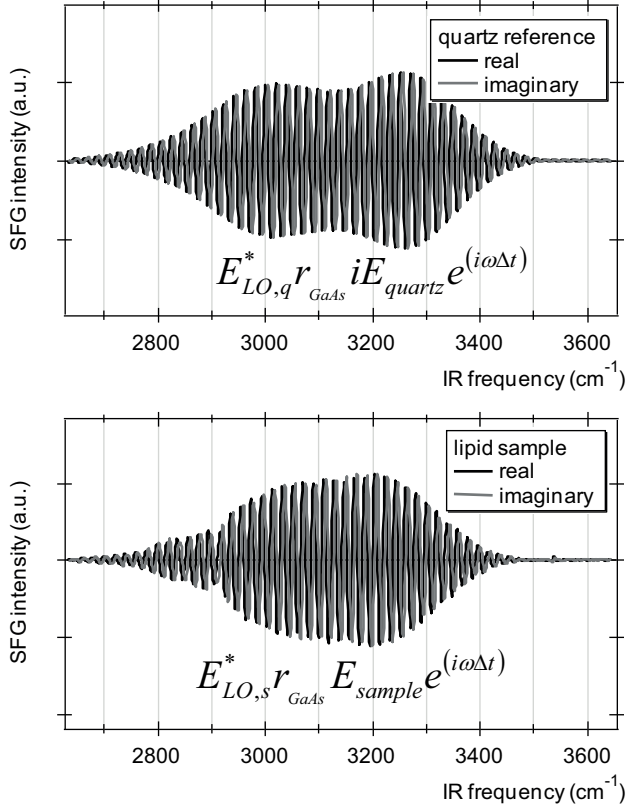
FIGURE 5.5. Linear terms of the PS-SFG intensity of the quartz reference (top) and sample (bottom) obtained by Fourier transforming the selected regions of figure 5.4. Dividing sample by reference gives what may be defined as the PS-SFG intensity I_{PS}, the normalized cross term of the total PS-SFG intensity (equation 5.7).

$$I_{\text{dir}} = \frac{|E_{\text{sample}}|^2}{|E_{\text{quartz}}|^2} = \frac{\left|\varepsilon_0 F_{\text{sample}} \chi_{\text{sample}}^{(2)} E_{\text{VIS}} E_{\text{IR}}\right|^2}{\left|\varepsilon_0 F_{\text{quartz}} \chi_{\text{quartz}}^{(2)} E_{\text{VIS}} E_{\text{IR}}\right|^2} = \frac{\left|F_{\text{sample}} \chi_{\text{sample}}^{(2)}\right|^2}{\left|F_{\text{quartz}} \chi_{\text{quartz}}^{(2)}\right|^2} \quad (5.9)$$

To allow a quantitative comparison between the squared direct SFG terms to the linear PS-SFG spectrum, the squared magnitude of the latter should be taken:

$$|I_{\mathrm{PS}}|^2 = \frac{\left| E_{\mathrm{LO,s}}^* E_{\mathrm{sample}} \right|^2}{\left| E_{\mathrm{LO,q}}^* E_{\mathrm{quartz}} \right|^2}$$

$$= \frac{\left| r_{\mathrm{sample}}\left(\omega_{\mathrm{VIS}}\right) r_{\mathrm{sample}}\left(\omega_{\mathrm{IR}}\right) \right|^2}{\left| r_{\mathrm{quartz}}\left(\omega_{\mathrm{VIS}}\right) r_{\mathrm{quartz}}\left(\omega_{\mathrm{IR}}\right) \right|^2} \frac{\left| F_{\mathrm{sample}} \chi_{\mathrm{sample}}^{(2)} \right|^2}{\left| F_{\mathrm{quartz}} \chi_{\mathrm{quartz}}^{(2)} \right|^2} \tag{5.10}$$

producing the relation:

$$I_{\mathrm{dir}} = \frac{\left| F_{\mathrm{sample}} \chi_{\mathrm{sample}}^{(2)} \right|^2}{\left| F_{\mathrm{quartz}} \chi_{\mathrm{quartz}}^{(2)} \right|^2} = \frac{\left| r_{\mathrm{quartz}}\left(\omega_{\mathrm{VIS}}\right) r_{\mathrm{quartz}}\left(\omega_{\mathrm{IR}}\right) \right|^2}{\left| r_{\mathrm{sample}}\left(\omega_{\mathrm{VIS}}\right) r_{\mathrm{sample}}\left(\omega_{\mathrm{IR}}\right) \right|^2} |I_{\mathrm{PS}}|^2$$

$$\approx \frac{\left| r_{\mathrm{quartz}}\left(\omega_{\mathrm{IR}}\right) \right|^2}{\left| r_{\mathrm{sample}}\left(\omega_{\mathrm{IR}}\right) \right|^2} |I_{\mathrm{PS}}|^2 \tag{5.11}$$

This indicates that a correction for the reflection coefficient should be sufficient to match the two spectra. In the last step we make use of the fact that the reflection coefficient is roughly frequency independent across the narrow bandwidth of the placeVIS pulse, so that we only have to consider the IR range. Also, it is safe to assume that the reflectivity of the water-lipid-air interface does not deviate much from that of the water-air interface, since only a single molecular layer of lipids is present [108]. The reflectivity of water has strong real and imaginary components in the mid-infrared, the latter due to its vibrational resonance, while the reflectivity of quartz is real, small and non-resonant, and therefore hardly contributes to the signal.

The reflectivity coefficient for the p-polarized infrared radiation is given by [109]:

$$R_p = \left(\frac{n_1 \cos \vartheta_t - n_2 \cos \vartheta_i}{n_1 \cos \vartheta_t + n_2 \cos \vartheta_i} \right)^2 = \left(\frac{n_1 \sqrt{1 - \left(\frac{n_1}{n_2} \sin \vartheta_i\right)^2} - n_2 \cos \vartheta_i}{n_1 \sqrt{1 - \left(\frac{n_1}{n_2} \sin \vartheta_i\right)^2} + n_2 \cos \vartheta_i} \right)^2 \tag{5.12}$$

where n_1 is the index of refraction of air, n_2 the frequency-dependent complex index of refraction of water [110], θ_t the angle of refraction and θ_i the angle of incidence with respect to the surface normal. Note that in experiments where an isotopic dilution of D_2O in H_2O is used, determination of the reflection coefficient becomes more complex, since it is insufficient to consider a proportional combination of the index of refraction of both liquids, as the infrared response of HDO is not a linear combination of that of D_2O and H_2O.

As shown in the appendix, there is also a reliable way of independently determining the squared magnitude of the reflectivity, which should be particularly helpful to assess the theoretical prediction of the reflection coefficient for such samples where the complex bulk refractive index is not confidently known.
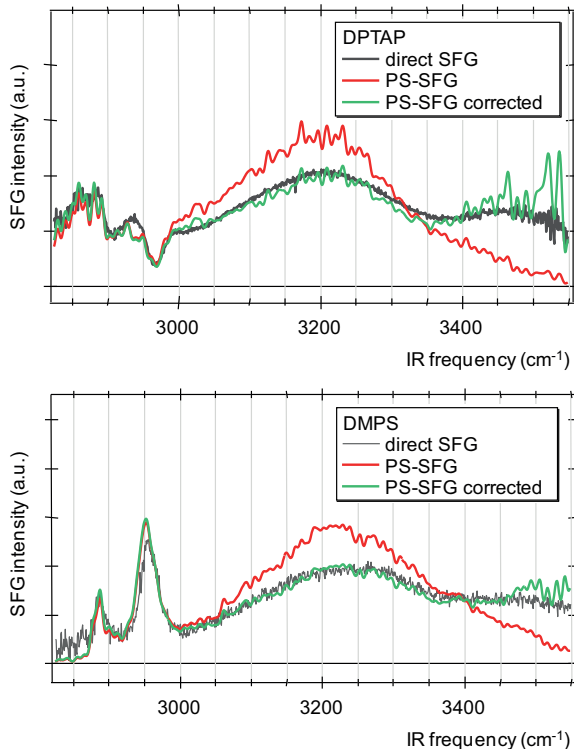

FIGURE 5.6. Intensity spectra of DPTAP (top) and DMPS (bottom) obtained by direct SFG and PS-SFG detection. The squared magnitude of the PS-SFG results is plotted, before and after correction for reflection coefficients. This correction does not cause much change in the CH region (the two peaks around 2900 cm^{-1}). The spectral shape of the broad OH band, however, is greatly affected by the reflection coefficients and only matches the direct SFG intensity spectrum after the correction is applied.

In figure 5.6, the effect of this correction is shown for a DPTAP and a DMPS monolayer. Both spectra show the CH$_3$ symmetric stretch (2880 cm^{-1}), the CH$_3$ Fermi resonance of the CH$_3$ symmetric stretch and bend overtone (2940 cm^{-1}), and the OH stretch (around 3200-3400 cm^{-1}) vibrations; these are well known from literature (e.g. [111]). It is apparent that without correcting for the infrared reflectivity of the water interface there is significant disagreement between the direct SFG response and the 'direct' response inferred from the PS-SFG measurements. Applying the mentioned correction for the reflection coefficient of water makes the direct SFG and PS-SFG spectra neatly overlap.

The effect of the complex reflection coefficient correction on the imaginary
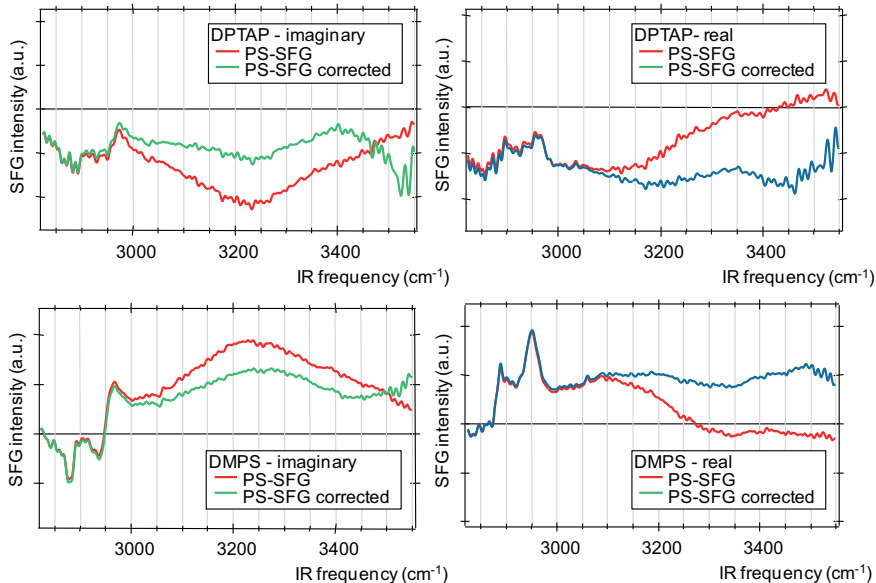
Figure 5.7. The imaginary and real parts of the complex spectra of DPTAP (top two panels) and DMPS (bottom two panels) found by PS-SFG detection and analysis. The results are shown before and after correction for the reflection coefficients, displaying the large influence of the sample reflectivity on the spectral shape.

and real part of $\chi^{(2)}$ is shown in figure 5.7. The imaginary spectra of both lipid samples reveal that next to the two negative CH_3 peaks seen in the direct spectrum, a positive peak is present at $2970 \, cm^{-1}$; this is the CH_3 antisymmetric stretch vibration [111]. The broad water peak is negative for DPTAP and positive for DMPS, in agreement with a study by the Tahara group16. Clearly, without the reflectivity correction the amplitude of the OH band in the Im $\chi^{(2)}$ spectrum is overestimated for both lipids, but the exact change in shape is dependent on the relative real and imaginary components. It seems evident that it is important to apply this correction before assigning individual resonances to the inferred spectral shape, applying this correction can result in significant changes to amplitude, frequency and even sign of resonances. Note that above $3400 \, cm^{-1}$ the reflection coefficient of water becomes very small, causing the noise on the corrected data to diverge. One should thus take care in considering this region in the fitting of the complex spectrum.

5.4   Discussion of SNR

The preceding discourse shows that the correct interpretation of PS-SFG spectra hinges on careful data analysis and the application of corrections of the amplitude and phase of the signal. Provided these measures are taken, PS-SFG can provide complex spectra that contain the phase information of the studied

interface, thereby surpassing the possibilities of direct SFG spectroscopy.

A second previously reported advantage arising from PS-SFG detection is an increase of signal-to-noise ratio (SNR) [33, 34, 42, 112]. Indeed, the PS-SFG signal can be orders of magnitude higher than the direct SFG signal due to interference with a large SFG signal from the local oscillator. Consequently, the detected PS-SFG signal may be lifted above noise sources in the detection, like dark current noise and read out noise. We show below that although the technique can provide a higher SNR in specific cases, it generally does not result in improvement. In order to quantify the increase in SNR we again compare direct SFG and PS-SFG detection. In this comparison we assume the setup consists of state of the art experimental equipment. The direct SFG and PS-SFG noise terms consist of photon shot noise (N_{shot}), dark current noise (N_{DC}), and other noise sources in the readout (electrical, N_R). Hence the total noise in both measurements amounts to:

$$N_{tot} = \sqrt{N_{shot}^2 + N_{DC}^2 + N_R^2} \tag{5.13}$$

In a typical direct SFG experiment, the photons are detected by a deep cooled (electron multiplying) charge coupled device (emCCD) camera. The number of detected SFG photons ranges from one to several thousand per pixel for a typical measurement.

For the camera that is used in our measurements, the dark current noise is 0.0002 counts per pixel per second and the read out noise amounts to 2.8 counts per pixel per read out. The dark current noise and readout noise of these instruments will therefore become irrelevant for signal strengths ranging in the hundreds of counts per pixel. For the lipid monolayers studied in this chapter, the intensity at resonances was 150 to 600 counts per pixel when setting an integration time of 360 s. When photon counts do indeed range in the hundreds, the SNR is dominated by photon shot noise, which scales with the square root of the total intensity. For the direct SFG measurements, we can then write the SNR as the ratio of the SFG intensity to the noise:

$$SNR_{\mathrm{dir}} = \frac{I_{SFG,\mathrm{sample}}}{N_{tot}} \approx \frac{I_{SFG,\mathrm{sample}}}{N_{shot}} \propto \frac{I_{SFG,\mathrm{sample}}}{\sqrt{I_{SFG,\mathrm{sample}}}} = \sqrt{I_{SFG,\mathrm{sample}}}$$

$$N_{shot} > N_{DC}, N_R$$

$$\tag{5.14}$$

This relationship would imply that the larger signal I observed in a PS-SFG measurement would result in increased signal-to-noise. The situation is not that simple, however: in a PS-SFG measurement, the SFG signal originates from multiple contributions, namely the SFG signal from the sample, the SFG signal from the local oscillator, and the cross terms (CT) due to interference of the two (equation 5.2). The cross term holds all the useful (phase) information and is proportional to the sample electric field ($E_{SFG,\mathrm{sample}}$) times the local oscillator electric field ($E_{SFG,\mathrm{LO}}$), but the signal is 'carried' on top of the (generally) much larger signal from the local oscillator alone ($I_{SFG,\mathrm{LO}}$).

Suppose that the field strength from the local oscillator is c times higher than that emitted by the sample. The signal contributions are then given by:

$$E_{SFG,\text{LO}} = cE_{SFG,\text{sample}}$$
$$I_{SFG,\text{LO}} = c^2 I_{SFG,\text{sample}} \tag{5.15}$$
$$I_{SFG,CT} = E_{SFG,\text{LO}}E_{SFG,\text{sample}} = cE^2_{SFG,\text{sample}} = cI_{SFG,\text{sample}}$$

The total noise in the PS-SFG measurement consists of the combined noise from the sample, the local oscillator, and noise in the cross terms. Due to the strong signal from the local oscillator ($c \gg 1$), the total noise is dominated by the shot noise of this contribution:

$$N_{shot} \approx N_{shot,\text{LO}} \text{ for } c \gg 1$$
$$N_{shot,\text{LO}} \propto \sqrt{I_{SFG,\text{LO}}} = cE_{SFG,\text{sample}} \tag{5.16}$$

The higher photon counts in the PS-SFG experiment lift the SFG signal above the dark current noise and electrical detection noise, which can also be neglected. Therefore in the PS-SFG experiment we only have to account for the photon shot noise from the local oscillator. The SNR for the PS-SFG signal is given by:

$$SNR_{\text{PS}} = \frac{I_{SFG,CT}}{N_{tot}} \approx \frac{I_{SFG,CT}}{N_{shot,\text{LO}}} \propto \frac{cI_{SFG,\text{sample}}}{cE_{SFG,\text{sample}}} = SNR_{\text{dir}} \tag{5.17}$$
$$\text{for } N_{shot} \gg N_{DC}, N_R$$

Perhaps surprisingly, the SNR of the PS-SFG measurement is not sensitive to the relative signal strength of the local oscillator c, and equals that of the direct SFG measurement in case the shot noise is the limiting factor. Analogous conclusions have previously been reached in the analysis of phase-specific second-harmonic generation spectroscopy [113]. Only if the SNR in the direct SFG measurement is not shot noise limited, i.e. if it is dominated by dark current noise or read out noise, an increase of SNR is expected in the PS-SFG measurement.

Furthermore, in the analysis we have assumed ideal experimental conditions for the PS-SFG experiment, with shot noise being the only source of noise. Figure 5.8 shows that under these conditions the SNR is equal for both techniques for all signal strengths (dashed line). In practice however, deviations from this ideal behaviour will occur, as the GaAs is not a perfect reflector for the sample SFG signal. Therefore, a more realistic picture shows that PS-SFG does show an increase in SNR for low signal strengths, while for higher numbers of counts direct SFG detection may be preferred, because of the PS-SFG signal loss caused by the GaAs reflectivity (figure 5.8, solid lines). Another effect that realistically cannot be avoided is suboptimal interference: when the two fields E_{sample} and E_{LO} do not perfectly overlap on the CCD camera, the fringes
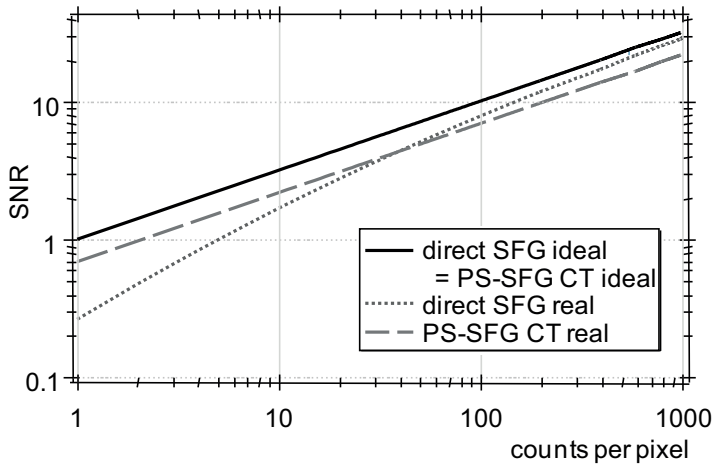
FIGURE 5.8. Theoretical predictions of direct SFG and PS-SFG signal-to-noise ratio (SNR) as a function of photon counts per pixel of the total spectrum (direct case) or of the cross term (CT, PS-SFG case). Although in the ideal case of only shot noise the two are equal (equation 5.17), realistically PS-SFG detection performs better at very low photon counts since the strong local oscillator intensity lifts the signal above the read-out noise. Alternatively, at higher photon counts the SNR of PS-SFG detection can be expected to be surpassed by direct detection because of the signal loss due to GaAs reflectivity and suboptimal interference.

caused by the interference will be less deep than theoretically possible, resulting in an overall lower intensity of the linear cross terms28. In figure 5.8, these two effects – GaAs reflectivity and suboptimal interference – are assumed to lower the real PS-SFG SNR by a factor of 0.7 when compared to the ideal SNR. Note that extracting the PS-SFG cross term by selecting a time window (figure 5.4) is a form of Fourier filtering, and in this process some high-frequency noise is filtered out. Since this practice is also possible for direct SFG spectra, it is not an intrinsic advantage of PS-SFG spectroscopy. One should take notice of this filtering effect when comparing direct SFG and PS-SFG spectra in the way that is shown in figure 5.6, since the noise that is apparent in the spectrum may be misleading.

Summarizing this section on signal-to-noise, PS-SFG spectroscopy can reach a better SNR in the case of samples that generate very weak SFG fields, but generally PS-SFG detection does not result in improvement of the SNR for the case of the relatively high signals of a typical aqueous or metallic surface. The underlying reason is that, while overall signal levels are indeed increased for PS-SFG compared to direct detection, the shot noise also increases proportionally. While it is evident that implementing PS-SFG spectroscopy can overcome the sensitivity limits of the direct SFG technique in the very low signal limit, it is certainly not true that the SNR increases as a general rule.

5.5   Conclusion

We have shown that with correct data analysis and reflectivity corrections, the PS-SFG and direct SFG signals can be equated. A particularly important correction originates from the fact that the spectrum of the infrared pulse at the local oscillator is different from that at the sample, due to dispersion in the linear reflectivity of the sample. Our data show that correcting for this and other effects influences the shape of the retrieved second-order nonlinear susceptibility $\chi^{(2)}$ significantly, indicating that care must be taken when extracting the complex $\chi^{(2)}$ from the PS-SFG intensity spectra: without the proper correction, the spectra of the imaginary part of $\chi^{(2)}$ may contain features that do not reflect the physical reality of the surface. Additionally we have made a theoretical prediction of the signal-to-noise that can be obtained by PS-SFG, and show that generally the signal-to-noise of direct- and PS-SFG detected signals will be very similar when limited by shot noise; only at very low signal strengths will the signal-to-noise of PS-SFG detection exceed that of direct detection.

5.6   Appendix: calculated and empirical reflectivity corrections

The magnitude squared reflectivity correction can be calculated, given the experimental geometry and the tabulated complex refractive index of the aqueous interface, but it can also be extracted from the squared terms of the total PS-SFG intensity:

$$
\begin{aligned}
&\left|E_{\text{LO,s}}\right|^2 + \left|r_{\text{GaAs}}E_{\text{sample}}\right|^2 \\
&= \left|\varepsilon_0 F_{\text{GaAs}}\chi^{(2)}_{\text{GaAs}}r_{\text{sample}}\left(\omega_{\text{VIS}}\right)r_{\text{sample}}\left(\omega_{\text{IR}}\right)E_{\text{VIS}}E_{\text{IR}}\right|^2 \\
&\quad + \left|r_{\text{GaAs}}\varepsilon_0 F_{\text{sample}}\chi^{(2)}_{\text{sample}}E_{\text{VIS}}E_{\text{IR}}\right|^2 \\
&\approx \left|\varepsilon_0 F_{\text{GaAs}}\chi^{(2)}_{\text{GaAs}}r_{\text{sample}}\left(\omega_{\text{VIS}}\right)r_{\text{sample}}\left(\omega_{\text{IR}}\right)E_{\text{VIS}}E_{\text{IR}}\right|^2
\end{aligned}
\tag{5.18}
$$

In the last step we use that $\chi^{(2)}_{\text{sample}} \ll \chi^{(2)}_{\text{GaAs}}$. In principle, the sample term can be cancelled by subtracting the direct SFG spectrum from this expression, making it more precise.

For quartz, both terms are of comparable magnitude and cannot be simplified:

$$
\begin{aligned}
&\left|E_{\text{LO,q}}\right|^2 + \left|r_{\text{GaAs}}E_{\text{quartz}}\right|^2 \\
&= \left|\varepsilon_0 F_{\text{GaAs}}\chi^{(2)}_{\text{GaAs}}r_{\text{quartz}}\left(\omega_{\text{VIS}}\right)r_{\text{quartz}}\left(\omega_{\text{IR}}\right)E_{\text{VIS}}E_{\text{IR}}\right|^2 \\
&\quad + \left|r_{\text{GaAs}}\varepsilon_0 F_{\text{quartz}}\chi^{(2)}_{\text{quartz}}E_{\text{VIS}}E_{\text{IR}}\right|^2
\end{aligned}
\tag{5.19}
$$

In this case we have to use the fact that the second term is equal to the direct SFG reference. Subtracting this term and dividing equation 5.18 by the resulting expressions gives:

$$
\frac{|E_{\text{LO,s}}|^2}{|E_{\text{LO,q}}|^2} = \frac{\left|\varepsilon_0 F_{\text{GaAs}} \chi_{\text{GaAs}}^{(2)} r_{\text{sample}}(\omega_{\text{VIS}}) r_{\text{sample}}(\omega_{\text{IR}}) E_{\text{VIS}} E_{\text{IR}}\right|^2}{\left|\varepsilon_0 F_{\text{GaAs}} \chi_{\text{GaAs}}^{(2)} r_{\text{quartz}}(\omega_{\text{VIS}}) r_{\text{quartz}}(\omega_{\text{IR}}) E_{\text{VIS}} E_{\text{IR}}\right|^2}
$$

$$
= \frac{|r_{\text{sample}}(\omega_{\text{VIS}}) r_{\text{sample}}(\omega_{\text{IR}})|^2}{|r_{\text{quartz}}(\omega_{\text{VIS}}) r_{\text{quartz}}(\omega_{\text{IR}})|^2} \tag{5.20}
$$

which is exactly the correction term we were looking for (see equation 5.11). Figure 5.9 shows the correction extracted in this way compared to the squared magnitude of the complex reflectivity of water with an incident angle of 40 degrees.
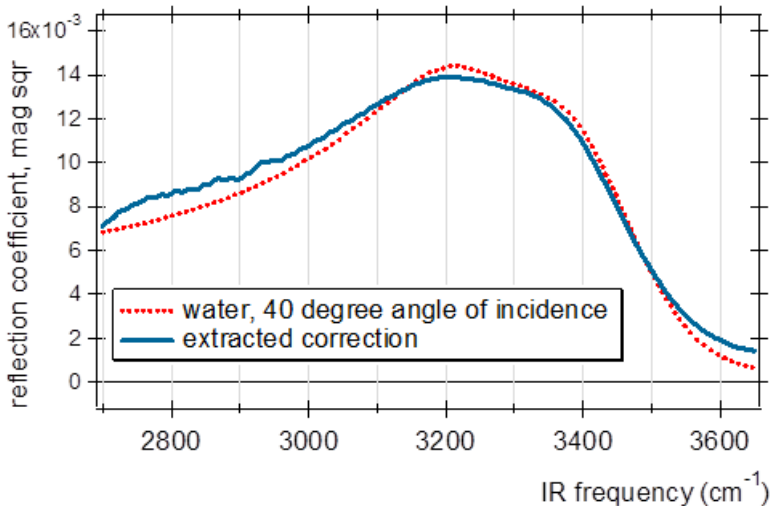

FIGURE 5.9. The squared magnitude of the sample reflectivity extracted from the quadratic terms of the PS-SFG intensity spectrum (equation 5.20) compared to the theoretical reflection coefficient of water (also magnitude squared). This method may be helpful to assess the reflectivity of samples of which the theoretical reflectivity is not straightforward to obtain, such as isotopic dilutions of D_2O in H_2O.

6 Nanoparticle-induced Molecular Reorganization at Lipid Monolayers

Proceeding with the exploration of the possibilities of SFG spectroscopy, we here apply it to a highly controllable, but biologically relevant model system of a lipid monolayer with charged nanoparticles (NPs). The interaction of lipid monolayers with charged polystyrene NPs is relevant for NP cytotoxicity and drug delivery research, and may serve as a general model for electrostatics at biomimetic interfaces. In this study, we employ vibrational sum-frequency generation (SFG) spectroscopy as a tool to probe and quantify binding of NPs to lipid monolayers. Strong spectral signatures of the interaction can be identified in both the interfacial water signal, and in the CH vibrations of the lipid alkyl chains. We examine the role of electrostatics on the interaction by using positively and negatively charged NPs, binding to lipids of positive, negative and zwitterionic charge. Although the interaction is strongest for opposing charges, as is to be expected, every combination displays some effect of nanoparticle presence in the SFG spectra. For zwitterionic lipids, a remarkable asymmetry arises that can be ascribed to the distribution of charges in and the flexibility of the lipid head group. The role of the interfacial water molecules in this system is followed in detail, and a schematic model of the molecular alignment is proposed. Scanning electron microscopy images provide a visual confirmation of the interaction.

6.1 Introduction

In recent years, the interaction of biological matter and nanomaterials has been a topic of discussion in both the scientific world and in society in general. The reason for this interest is the increasing application of nanomaterials in commercial and medical sectors. This rapid growth of exposure of the public to these relatively unknown substances raises health concerns, since our scientific knowledge may not keep up with these developments. The interaction of nanoparticles (NPs) with the human body is dependent on various factors, such as particle size, shape and charge, which determine the spread of particles through different parts of the body and the potential of causing damage there [114–116].

When examining the effect of NPs on the human body on a molecular scale, we should realize that a key interaction is that between the particles and the cell membrane. Firstly, whether the particles are able to move through this barrier greatly influences their spread through the body as a whole. Secondly, the potential disruption of a membrane by NPs is a cause of cytotoxicity, either trough necrosis or the triggering of apoptosis [60, 117].

Advances in synthesis methodology have shown that it is possible to produce NPs that pass through the cell membrane without damaging it [114, 118, 119]. This development confirms that NPs can be applied in a medical context, e.g. as drug carriers or stabilizers of targeted drug delivery systems [120]. To effectively synthesize NPs towards this end, it is crucial to understand the role that physicochemical properties such as size, charge and surface chemistry play in the interaction. More generally then, NPs are of fundamental interest to our understanding of the interaction between nanoscale objects and biological soft condensed matter. The controllability of their composition enables research focused on specific particle properties.

Many studies have focused on the interface between nanoparticles and phospholipids. Nonspecific binding of charged nanoparticles locally changes the fluidity of the lipid membrane in liposomes [46]. The fluidity of the lipids is reflected by the organization of the hydrophobic chains, which are typically more ordered in the gel phase than in the fluid phase. Recent simulations on phospholipid bilayers with nanoparticles of varying charge have confirmed these observations [121]. However, a gap remains in our understanding of the mechanism by which nanoparticles affect the membrane on a molecular level. A direct observation of lipid reorganization would be able to provide a link between the macroscopic observations on the one hand and theoretical and molecular dynamics simulations on the other. To this end, we here employ vibrational sum-frequency generation (SFG) spectroscopy, a second-order and therefore surface-specific optical technique [25]. We study monolayers composed of a single type of lipid, looking at various different lipids. SFG spectroscopy has been shown to be able to directly identify lipid chain ordering by looking at the relative sum-frequency intensity of the various CH-stretch vibrations [122]. It is therefore a suitable tool in studying the changes in molecular organization upon nanoparticle binding to lipid layers. Furthermore, SFG spectroscopy is very well suited to monitor the vibrational response of membrane bound interfacial water, which is known to be very sensitive to changes in the surface charge [24]. The behavior of water around the interface is of added value because of the important role of water in determining the structure and functioning of biological membranes [123].

In this study we focus on the role of NP and membrane charge. We choose single-lipid monolayers as model systems. Our charged model membranes are monolayers of DPPG, which is negatively charged due to a phosphate group, and DPTAP containing a positively charged choline group.

The third lipid that we studied is DPPC, which is electrostatically the most complex of the three since it contains both a negative phosphate and a positive choline group. This zwitterionic head group makes its electrostatic influence on
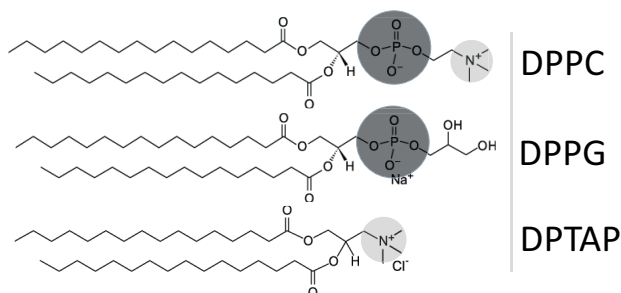
FIGURE 6.1. Chemical structure of the three lipids used in this study.

the surrounding water complex [124]. However, it is also the most studied phospholipid due to its prevalence in biological membranes, notably the mammalian pulmonary system [125, 126]. For DPPC, the binding of both positively and negatively charged NPs has been reported, with the negatively charged NPs raising the phase transition temperature by tens of degrees [127] and decreasing the membrane fluidity [46]. These observations can be intuitively interpreted as being caused by a local gelation of the lipids at the NP binding site. Molecular dynamics simulations have confirmed this hypothesis, and have shown an ordering effect due to the pull of the negative NP on the positive terminus of the DPPC head group [121,128]. The chemical structure of the three lipids is shown in figure 6.1, highlighting the structural similarities between them. Note that while our target system, the actual cell membrane, does not contain positively charged lipids, it has an abundance of nagatively charged and zwitterionic lipid species. We opted to include DPTAP to assess the water's response to a single choline group, in hope to better understand the partial effect of the two separate charge groups of DPPC.

We employ basic polystyrene latex NPs functionalized with small, simple charge groups: amidine provides a positive charge, carboxyl a negative charge. Evidently, the interaction between NPs and monolayers of opposite charge is expected to be electrostatically favored. The influence of NP binding on the monolayer fluidity and alkyl chain order, which are indicators of the membrane structure, is more complex since it depends on the charge distribution and orientation of the lipids head group [121, 128]. The spectral changes will indicate what the role is of electric charge on interfacial molecular reorganization upon NP binding. Scanning electron microscopy images were recorded as an additional and direct means to estimate the interfacial NP density.

6.2 Materials and methods

Lipids. The negatively charged phospholipid DPPG (1,2-dihexadecanoyl-sn-glycero-3-phospho-(1'-rac-glycerol) with sodium salt), the positively charged lipid DPTAP (1,2-dipalmitoyl-3-trimethylammonium-propane with chloride salt) and the zwitterionic phospholipid DPPC (dipalmitoylphosphatidylcholine,

figure 6.1) and its deuterated alternative d75-DPPC were obtained from Avanti
Polar Lipids. Self-assembled monolayers were produced by dropcasting a
solution of this lipid in chloroform (0.5 g/L) drop by drop onto a H_2O or
D_2O subphase. D_2O used in this study was obtained from Cambridge Isotope
Laboratories (MA), 99.96% pure and was used as received. H_2O used in this
study was distilled and then filtered using a Millipore unit to a final resistivity
of 18.2 MΩ per cm. Samples were prepared in a 20 mL Teflon-coated aluminum
trough. Surface pressure in these troughs was quantified using a commercially
available tensiometer (Kibron, Finland).

Nanoparticles. Polystyrene latex NPs have a mean diameter of 27 nm with
a standard deviation of 6 nm. Negatively charged NPs were functionalized with
carboxyl groups, yielding a charge density of 1.1 nm^2 per charge group (8.2 x
103 charges per particle). A zeta potential of -61.4 mV was measured by means
of electrophoretic mobility equipment (Malvern Instruments Ltd). Positively
charged NPs were functionalized with amidine groups, yielding a charge density
of 4.3 nm^2 per charge (2.1 x 103 charges per particle) and a zeta potential of
53.3 mV.

After preparation of the monolayer, NPs were injected underneath the sur-
face without puncturing it through a hole in the side of the trough. In all
described experiments concentrations are expressed in μL of 4 volume-% NP
suspension. The aqueous suspension was injected into the subphase (i.e. the
water reservoir underneath the monolayer) while gently stirring with a magnetic
stirrer located on the bottom of the sample holder. The resulting NP concen-
tration was 0.32 nM per 1 μL injected suspension. The added NP cross section
surface present in the trough at a concentration of 1 μL is enough to cover the
entire monolayer surface.

Tensiometry measurements. In tensiometry, the two-dimensional pressure
along the circumference of a needle tip is measured. This surface pressure re-
flects the surface free energy, which changes upon the binding or insertion of
new molecules to or into an existing monolayer [129, 130]. Tensiometry mea-
surements were performed using the Wilhelmy plate method (Kibron Inc.). In
tensiometry, the two-dimensional pressure along the circumference of a needle
tip is measured. This surface pressure is indicative of the surface free energy,
which changes upon the binding or insertion of new molecules to or into an exist-
ing monolayer. Tensiometry measurements were performed using the Wilhelmy
plate method (Kibron Inc.).

Sum-frequency generation spectroscopy. SFG spectroscopy is able to probe
interfaces specifically and background-free through the second-order non-linear
susceptibility $\chi^{(2)}$ of the sample material.

In the SFG experiments, 1 mJ of the output of a regeneratively amplified
titanium sapphire system (Spitfire Ace, Spectra Physics, Inc.) producing ∼35
fs pulses centered at 800 nm was used to generate tuneable mid-IR pulses using
a homebuilt optical parametric amplifier and difference frequency generation
unit [68]. 0.5 mJ of the amplifier output was spectrally narrowed to ∼15 cm^{-1}
using a Fabry-Perot etalon. The IR beam passes through a half wave plate and
polarizer before being focussed with an f = 50 mm lens onto the sample together

with this spectrally narrowed visible beam, focussed with an f = 200 mm lens, with angles of incidence of 45° and 40° with respect to the surface normal and a power of 5 mW and 25 mW. The SFG signal was detected in reflection mode and focused into a spectrograph (Acton, Princeton Instruments) in which it was dispersed, via a grating, and focused onto an electron multiplied Charge Coupled Device (emCCD) camera (Newton, Andor). All spectra reported in this study were collected under the *ssp*-polarization condition (SFG and visible *s*, IR *p* polarizations). All measurements were conducted at 23 °C.

The increase in CH vibrational intensity can be thought to originate from a direct spectral response of CH modes within the NPs themselves. To check this, control experiments were performed on a monolayer deuterated DPPC (d75-DPPC). In the SFG spectrum of this deuterated lipid, the alkyl chain vibrations are removed from the 2800-2950 cm^{-1} region. By doing so, spectral changes caused by the introduction of new vibrational modes can be unambiguously separated from those caused by lipid reorganization. Upon injecting NPs underneath a d75-DPPC monolayer, no emerging peaks were observed in the CH region, ruling out the possibility of the presence of molecular vibrations within this region of moieties within or on the polystyrene NPs. At first sight, this observation may be surprising given the abundance of CH modes within polystyrene polymers. However, the small size of the nanoparticles in conjunction with their internal symmetry causes their SFG response to cancel out [131].

Scanning electron microscopy (SEM). Samples for SEM were prepared by means of the exact same protocol as the SFG spectroscopy samples, and then deposited on a silicon template-stripped gold (40-45 nm) on glass substrate by Langmuir-Schfer deposition. The SEM images were all taken with an FEI GEMINI SEM-system for a 10 μL 4% volume suspension of NPs, amounting to a concentration of 3.2 nM, and stirred for 20 minutes.

Reference measurements without lipids were performed observe the possible direct interaction between gold substrate and NPs. These images showed no deposition of NPs, indicating that all NPs observed in the SEM images in this chapter are lipid-mediated.

6.3   Results and discussion

DPTAP

Pure monolayers of the positively charged lipid DPTAP were prepared at a surface pressure of 28 mN/m. Charged NPs were injected underneath the monolayer while stirring with a magnetic stirrer. To visualize the binding of NPs to the monolayer and estimate the interfacial concentration, the monolayer was deposited on a gold substrate and recorded by means of SEM. Figures 6.2 and 6.3 show the resulting images for monolayers with 3.2 nM of carboxyl (-) and amidine (+) coated polystyrene latex NPs, respectively. Although with this technique no lipid structures are discernible, the 30 nm NPs are readily iden-

tifiable. Clearly, electrostatics dominate the interaction: adding the negatively
charged NPs to the positively charged surface causes large clusters of NPs to
congregate at the surface (figure 6.2). Combining equal charges, on the other
hand, shows no trace of NP binding, with only a few particles visible in the
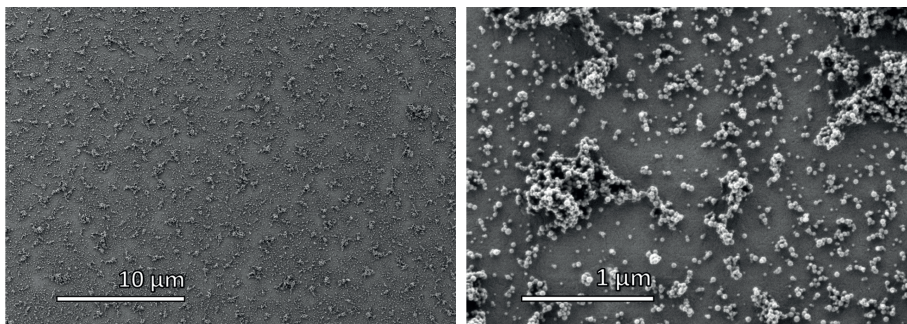image (figure 6.3, right image).

FIGURE 6.2. SEM image of DPTAP (+) monolayer with 3 nM carboxyl (-) NPs
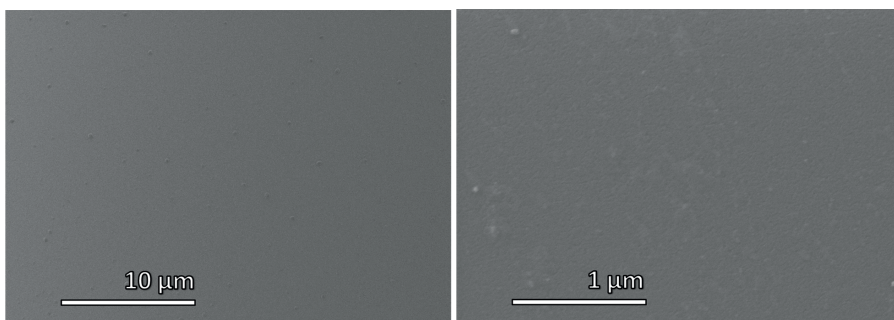deposited on a gold substrate.

FIGURE 6.3. SEM image of DPTAP (+) monolayer with 3 nM amidine (+) NPs
deposited on a gold substrate. Hardly any particles are present due to the electrostatic
repulsion.

SFG spectra of the aqueous sample were recorded for a range of NP concen-
trations. A few of these spectra are shown in figure 6.4. First, the response of
the DPTAP monolayer was measured without any NPs present; this spectrum
is shown in red. The most prominent features are the double water (OD) fea-
ture between 2200 and 2600 cm^{-1} and the various CH vibrations around 2900
cm^{-1}. The two apparent water peaks do not, in fact, arise from separate water
structures, but are due to a dip caused by intramolecular coupling between bend
and stretch vibrations of the water molecule [132]. The CH vibrational modes
of saturated lipid alkyl chains give rise to six SFG peaks in the 2800-2950 cm^{-1}
region [133]. For most lipids at high concentration, the three most intense of
these are the CH_2 symmetric stretch (CH_2SS, 2854 cm^{-1}), the CH_3 symmetric
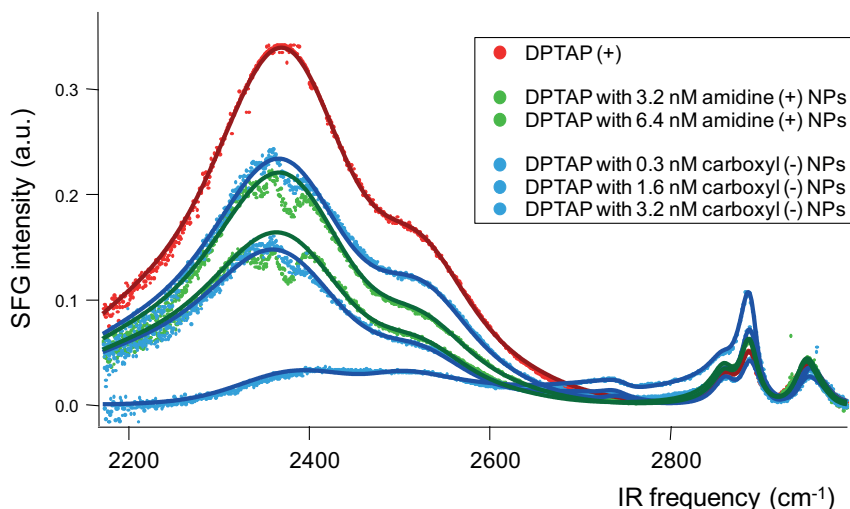
FIGURE 6.4. Vibrational SFG spectra of a DPTAP (+) monolayer with varying concentrations of carboxyl (-, blue) and amidine (+, green) functionalized latex nanoparticles.
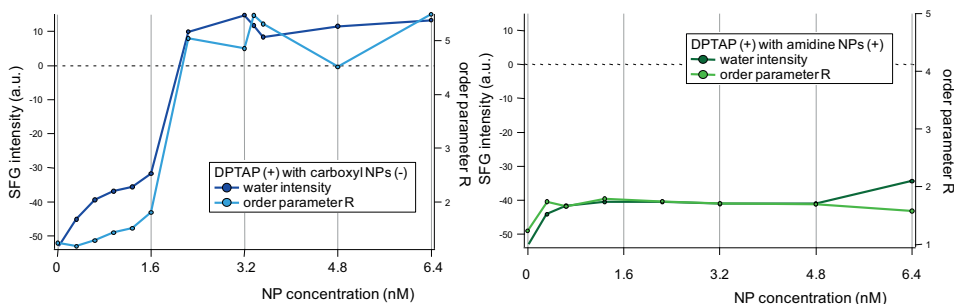

FIGURE 6.5. OD stretch resonance intensity (water intensity) and order parameter R extracted from the fits in figure 6.4 plotted as a function of concentration for carboxyl (-, left, blue) and amidine (+, right, green) nanoparticles. Note the negative sign of the water intensity, a large negative value implying a strong negative signal.

stretch (CH$_3$SS, 2883 cm^{-1}), and a Fermi Resonance of the CH$_3$ symmetric stretch and bend overtone (CH$_3$FR, 2946 cm^{-1}) [111]. For increasing lipid density, the CH$_2$SS diminishes because of internal cancellation of the SFG signal within the alkyl chains, which become more centrosymmetric as pressure (and therefore chain order) increases. The CH$_3$SS, on the other hand, increases with lipid density, thus making the intensity ratio R = I$_{CH_3}$/ ICH$_{CH_2}$ a measure to quantify lipid order [18].

Adding NPs beneath the monolayer induced significant and distinct changes in the spectra within minutes after injection. Both for the carboxyl (-) and

amidine (+) NPs, the water signal intensity and the order parameter R change dependent on NP concentration, which proves that the NPs interact with the lipid monolayer. To quantify the observed spectral changes, the VSF spectra were fitted by assigning Lorentzian line shapes to the CH modes and Voigt profiles to the water bands [25, 63].

Apart from the double water feature and the three aforementioned CH vibrations, two Lorentzians were needed to obtain an accurate fit of the spectra. The first is a weak, broad feature around $2650 2700$ cm^{-1} that can be attributed to weakly hydrogen bonded water bordering the lipid and/or air-water interface [35]. The second is a very weak and narrow (33 cm^{-1}) feature at 2750 cm^{-1} that corresponds to an overtone of the CH$_3$ bend mode [134]. Figure 6.4 shows the fitted spectra for a selection of NP concentrations. The increase in noise level around 2350 cm^{-1} is due to IR absorption by the CO2 asymmetric stretch vibration in air.

The decrease of the water intensity is the most striking effect that the injection of NPs underneath the DPTAP monolayer has on the SFG spectrum. This decrease implies that water alignment at the air-lipid-water interface is disturbed, which is likely to be caused by the changes in the electrostatic potential at the surface upon introducing the highly multivalent charged NPs. While SFG spectroscopy is highly surface specific, both the second-order susceptibility (2) and the third-order susceptibility (3) contribute to the signal at a charged interface [135, 136]. The former arises from water molecules aligned at the interface, the latter from the fact that a static potential is present at a charged interface so that a signal from the isotropic bulk appears. While spectral changes may originate from both (2) and (3) and their relative contribution is hard to estimate, any such change must be caused by a modulation of the electrostatic potential. An additional effect may be that the presence of NPs at the surface pushes a part of the water contributing to the SFG signal out of the interfacial region.

Figure 6.5 displays the concentration dependence of the water intensity defined as the sum of the intensities of the two water peaks between 2200 and 2600 cm^{-1} for carboxyl (-) NPs (left) and amidine (+) NPs (right). The fitted intensity does not only have a magnitude, but also a sign, indicating the phase of the vibration, i.e. whether the molecular bond is pointing up or down with respect to the surface. For water aligned by a positive monolayer, which is to say with the negative oxygen pointing up and the positive hydrogens pointing down, commonly a negative sign is assigned, as is indicated on the left axes in figure 6.5.

Looking at figure 6.5, left panel, we can conclude that the carboxyl (-) NPs interact strongly with the oppositely charged choline in the lipid head group. With increasing concentration of NPs, more and more negative charges are added to the positively charged surface, and we see the water signal go to zero. This tells us that the carboxyl (-) NPs are closely bound to the DPTAP head group; if a layer of water would be present between the two, a strongly aligned negative signal would remain. At higher NP concentrations (> 2 nM) the water intensity becomes positive; this effect can also be seen in figure 6.4

as a remarkable change in spectral shape due to interference of the overlapping
vibrations. This is a strong indication that charge inversion takes place at
the interface: the overcompensation of the potential at a charged surface by
opposing charged ions or particles, which various studies have reported to occur
with multivalent charge groups [137–142]. In these studies, the multivalence of
the charged particles was crucial to changing the surface charge. This explains
the seemingly low influence of counterions in the current experiments. In terms
of molecular structure, the charge inversion in this case may be caused by the
negative carboxyl group being in direct contact with the water molecules, while
the positive charge on the lipids choline group is shielded by the head groups
methyl groups and by the carboxyl NPs themselves.

When adding amidine (+) NPs, the water signal decreases (the solid green
line in figure 6.5, right panel), but much less strongly than for the carboxyl NPs.
This result may appear surprising at first glance, since a) the SEM images re-
vealed no interaction of the DPTAP monolayer and the amidine (+) NPs at all
(figure 6.3), and b) the charge on these particles, when located at the surface,
should only enhance the water alignment. However, combining these two obser-
vations, we may conclude that the amidine (+) NPs do not bind to the DPTAP
monolayer, but remain in a suspension in the subphase. The electrostatic po-
tential of this suspension of positively charged NPs below the interfacial water
opposes the alignment effect of the charged lipids. As a consequence the water
SFG response decreases.

In addition to variations in the water intensity, a second large spectral change
can be identified in the CH stretch vibrational region, around 2900 cm^{-1} (fig-
ure 6.4). The order parameter R calculated from these changes is plotted in
figure 6.5 as a function of NP concentration (dashed lines). It is immediately
clear that R closely follows the water intensity. Given the negative sign of the
water peak, this means that the water intensity is actually rather inversely pro-
portional to R. So what does this relation imply about the interaction on the
molecular level? Considering carboxyl (-) NPs first, the order of the lipids in-
creases with NP concentration. This effect has been reported before for DPPC
membranes in both theory and experiment, and was ascribed to the electrostatic
pull of the NPs negative charge on the flexible lipid head group [46, 121, 128].
This pull straightens the lipid, decreasing its footprint size (the space the head
group takes at the interfacial plane), increasing the local lipid density and the
phase transition temperature. We are able to detect these changes with SFG
spectroscopy due to the accompanied increase in alkyl chain ordering. It is
remarkable that DPTAP shows the same effect, since its smaller head group
size does not allow equally large changes in footprint size as those occurring in
DPPC. Possibly, the change in charge distribution over the atoms of the lipid
head group is enough to induce the molecular order.

For amidine (+) NPs, the change in lipid order parameter R is not significant.
Note that although in figure 6.5 (right panel) the change appears to be similar
to that of the water signal, the error on R is larger than on the water signal
because it originates from much smaller spectral features. The observation that
R remains unchanged (or decreases by a very small amount) is consistent with

the conclusion that amidine (+) NPs do not come into close contact with the monolayer but rather remain suspended in the subphase.
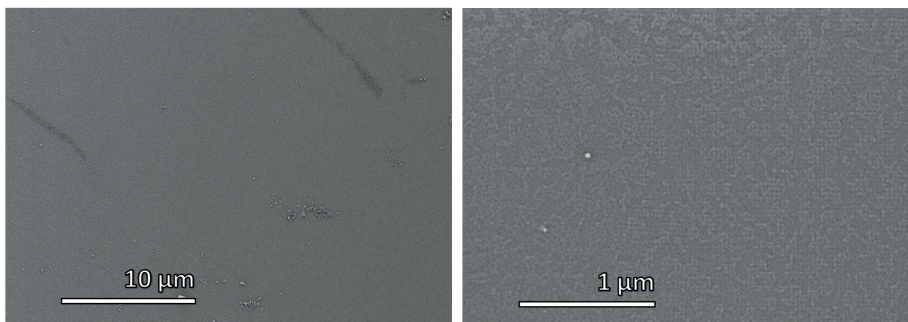
DPPG

FIGURE 6.6. SEM image of DPPG (-) monolayer with 3 nM carboxyl (-) NPs deposited on a gold substrate. Hardly any particles are present due to electrostatic repulsion.
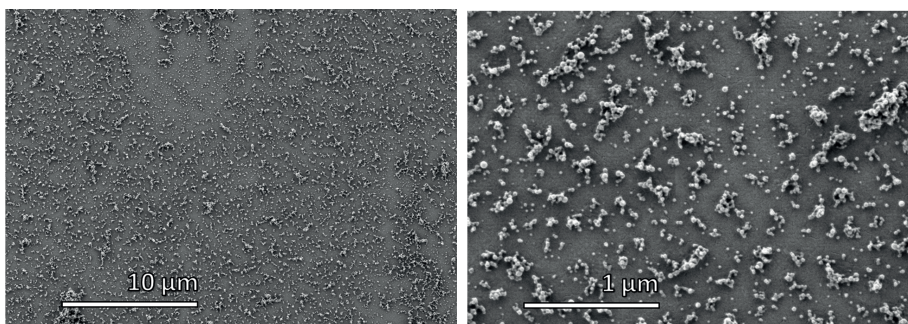

FIGURE 6.7. SEM image of DPPG (-) monolayer with 3 nM amidine (+) NPs deposited on a gold substrate.

The SEM and SFG measurements were repeated in the exact same way with monolayers prepared of the negatively charged lipid DPPG. Monolayers were prepared at a surface pressure of 30 mN/m. Figure 6.6 and 6.7 show SEM images of deposited monolayers of DPPG with 3.2 nM of carboxyl (-) and amidine (+) coated polystyrene latex NPs, respectively. Clearly, the result is the exact opposite of DPTAP: now the carboxyl (-) particles do not bind, while the amidine (+) NPs cover a significant area of the surface. Basic electrostatics is responsible for this behavior: the repulsion and attraction of carboxyl (-) and amidine (+), respectively, of NPs by the negatively charged phosphate group of DPPG. Two other, more subtle differences of DPPG with the DPTAP case can be identified: firstly, on a larger scale some inhomogeneous features can
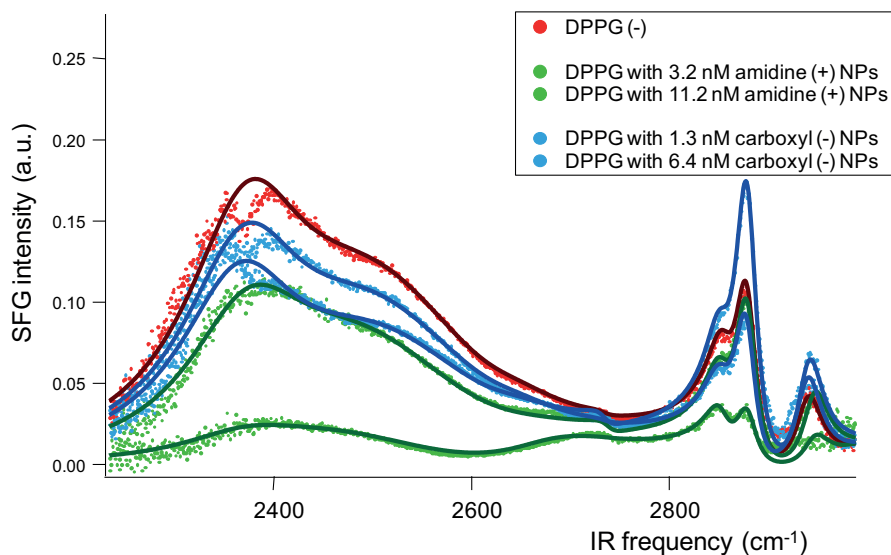
FIGURE 6.8. Vibrational SFG spectra of a DPPG (-) monolayer with varying concentrations of carboxyl (-, blue) and amidine (+, green) functionalized latex nanoparticles.
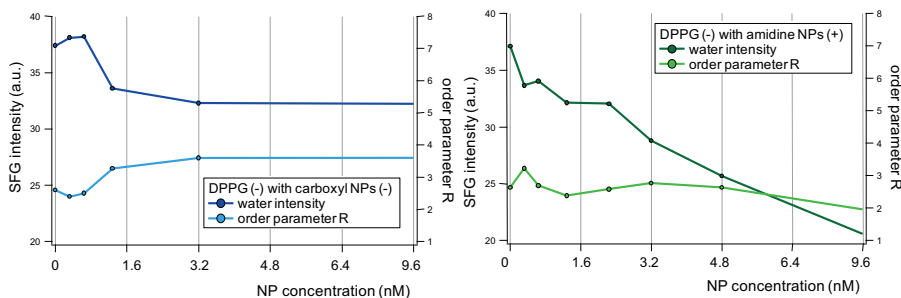

FIGURE 6.9. OD stretch resonance intensity (water intensity) and order parameter R extracted from the fits in figure 6.8 plotted as a function of concentration for carboxyl (-, left, blue) and amidine (+, right, green) nanoparticles.

be identified, where the concentration of NPs is locally larger (figure 6.6, left panel) or smaller (figure 6.7, left panel). Given7 the fluidity of the monolayer, inhomogeneities of this scale are unlikely to occur in single-lipid monolayers on an aqueous subphase, and should therefore be ascribed to impurities on the gold substrate. Secondly, the NP concentration and agglomeration rate is lower for DPPG with amidine (+) NPs than it was for DPTAP with carboxyl (-) NPs, even though the charge density on the amidine (+) NPs is lower. At this point, we may hypothesize that the electrostatic field of DPTAP is larger than that of DPPG, but SFG spectroscopy will shine more light on this issue.

Several SFG spectra of DPPG with NPs are shown in figure 6.8. Similar to the SEM images, many of the effects of NPs on the DPPG spectrum mirror the changes observed for DPTAP. Again, both amidine (+) and carboxyl (-) NPs lower the water intensity, but the effect is now much stronger for amidine (+) NPs (figure 6.9). Given the difference in head group charge between DPTAP and DPPG this makes perfect sense, and all conclusions about the mechanism of the interaction drawn for DPTAP equally hold for DPPG.

A difference between the DPTAP and DPPG interaction can be identified in the order parameter R for NPs of charge opposite to that of the lipid head group. While R increased in the case of DPTAP with carboxyl (-) nanoparticles, no such change can be seen for DPPG with amidine (+) NPs. Apparently the chemical structure of the DPPG head group, with the glycerol dangling beneath the negatively charged phosphate group, does not allow for the same ordering effect when feeling the pull of charged NPs underneath. A steric effect of the glycerol group, which may be forced under a non-zero angle with the rest of the lipid in order to allow the minimal distance between the charge on the lipids and on the NP, is a likely explanation for this asymmetry.

A final difference between the spectra of DPTAP and DPPG is the magnitude of the water intensity. Note here that it is customary to give the SFG intensity in arbitrary units, and that care should be given when quantitatively comparing SFG spectra of separate measurements [20, 66]. In this study however, experimental conditions were kept constant enough to obtain fully reproducible results for the different systems, justifying comparison. Looking at the relative size of the water and CH response gives a further sense of scale. The significantly smaller absolute value of the water signal of DPPG (+37) when compared to DPTAP (-52) indicates that the electrostatic potential felt by the interfacial water is lower for this lipid, thus reducing the overall alignment of water molecules. This spectral feature then supports the hypothesis drawn from the SEM images that the amidine (+) concentration at DPPG is lower than the carboxyl (-) concentration at DPTAP due to the size of the interfacial electrostatic potential.

DPPC

Monolayers of DPPC were prepared at a surface pressure of 27 mN/m. Figure 6.10 and 6.11 show SEM images of deposited monolayers of DPPC with 3.2 nM of carboxyl (-) and amidine (+) coated polystyrene latex NPs, respectively. The results are now completely different from those obtained with the charged lipids: both carboxyl (-) and amidine (+) NPs show up in the microscopy images, indicating that both NPs of opposite charge interact with and bind to the dipolar head group of DPPC.

Remarkably, the NPs now show no signs of aggregation. The fact that they remain perfectly separated here, at the DPPC layer, suggests that they do not aggregate in the subphase suspension, since it is unlikely that the surface potential at the DPPC interface would separate them again. More likely the aggregation observed for the charged lipids takes place at the lipid interface, where
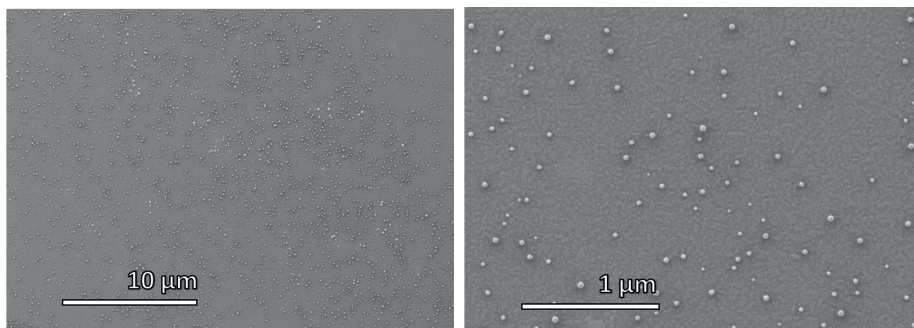
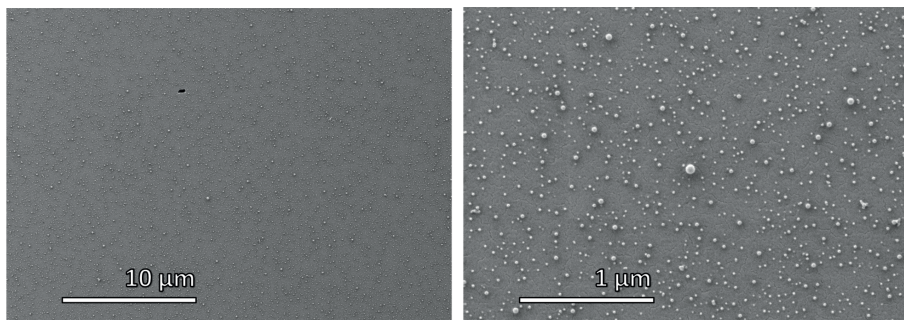FIGURE 6.10. SEM image of DPPC (-/+) monolayer with 3 nM carboxyl (-) NPs deposited on a gold substrate.

FIGURE 6.11. SEM image of DPPC (-/+) monolayer with 3 nM amidine (+) NPs deposited on a gold substrate.

the surface potential overcomes the repulsion of the particles. Despite their overall neutral charge, DPPC monolayers do cause an electrostatic alignment of the interfacial water through dipole-dipole interactions. Molecular dynamics simulations have predicted that the negative charge on the phosphate group dominates the electrostatic potential [143–146]. Phase-specific SFG studies confirmed that the average alignment of the interfacial water is with the hydrogen atoms pointing towards the monolayer, i.e. its dipole moment pointing up, and that the aligned water that contributes most to the SFG signal is located between the phosphate and the choline group [35, 124]. This indicates that the water feels an electrostatic potential similar to that created by a negatively charged lipid like DPPG. The relatively higher concentration of amidine (+) NPs than carboxyl (-) NPs at the DPPC interface observed in the SEM images (figure 6.10 and 6.11) may be explained by this overall negative potential caused by the zwitterionic head group.

In figure 6.12, several spectra of DPPC with carboxyl (-) and amidine (+) NPs are shown. As expected, our fitted SFG spectrum for pure DPPC shows a
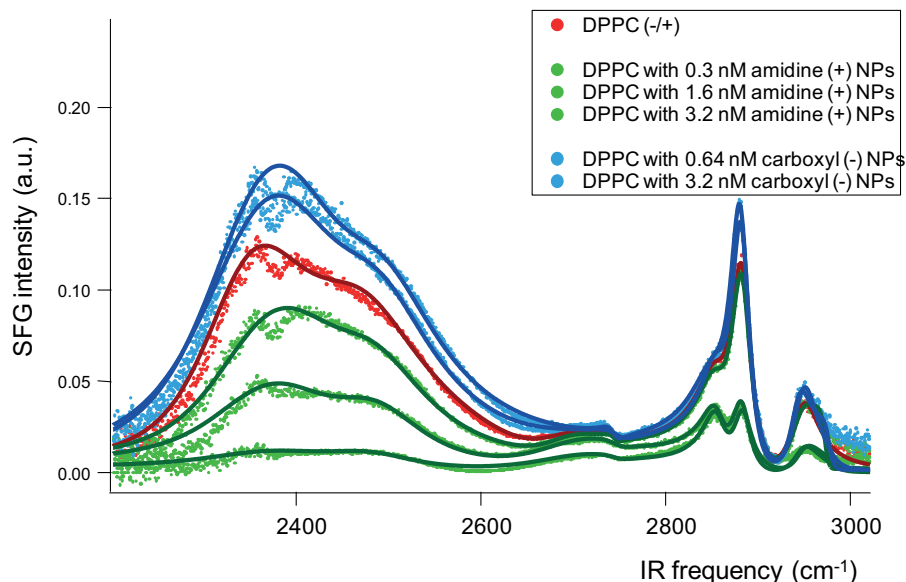
FIGURE 6.12. Vibrational SFG spectra of a DPPC (-/+) monolayer with varying concentrations of carboxyl (-, blue) and amidine (+, green) functionalized latex nanoparticles.
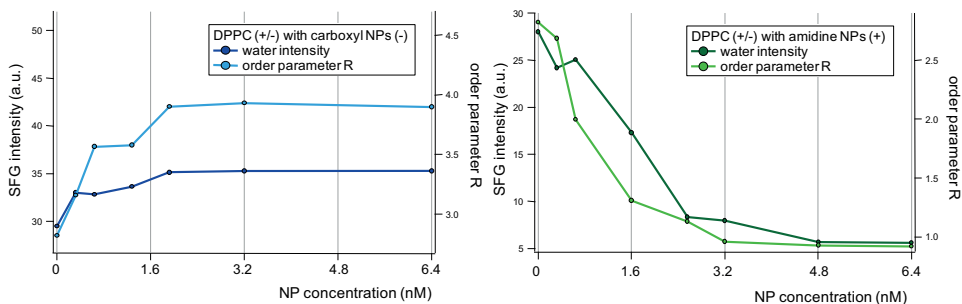

FIGURE 6.13. OD stretch resonance intensity (water intensity) and order parameter R extracted from the fits in figure 6.12 plotted as a function of concentration for carboxyl (-, left, blue) and amidine (+, right, green) nanoparticles.

large water peak of negative amplitude, implying that the water dipole moment is pointing up. Note that while we measure without phase sensitivity here, the relative sign of the amplitudes can be inferred from the line shapes: the general shape of the DPPC spectrum (figure 6.12) resembles that of DPPG (figure 6.8) much more than DPTAP (figure 6.4). Indeed, it is impossible to obtain a good fit of the DPPC spectrum when assigning a positive amplitude to the hydrogen bonded region.

The effects of increasing the NP concentration are now highly asymmetrical: carboxyl (-) NPs cause both the absolute water signal and the order parameter R to increase. Amidine (+) NPs cause the water signal and the order parameter to decrease. These changes can be explained by considering the flexibility of the dipolar head group of DPPC. In a typical membrane, the phosphorus-to-nitrogen vector makes only a small angle with the surface plane [147]. The pull of a carboxyl (-) NP on the choline group may increase this angle, while the pull of an amidine (+) NP on the phosphate group will likely decrease it. Since the electrostatic potential of DPPC is highest between the phosphate and choline groups [35, 146], the projection of the DPPC head group dipole vector on the surface normal determines the degree of water alignment, and thus the SFG water signal. The increase of the water signal observed for carboxyl NPs then implies that the lipid is stretched along the surface normal, which is in agreement with the according increase of the order parameter R in figure 6.13 (left panel). The lowering of the water signal to practically zero for the amidine (+) particles implies that the head group vector is parallel to the surface, increasing the lipid foot print and lowering the alkyl chain order, as is reflected by R in figure 6.13 (right panel). The increase in head group order for negative NPs and decrease in order for positive NPs is in good agreement with a recent molecular dynamics simulation study [148]. However, it was reported there that the changes in the head group order always led to a decrease in the order of the alkyl chains, in contrast to what we observe for DPPC with carboxyl (-) NPs. A possible explanation for this apparent discrepancy is the starting lipid surface pressure, which in the simulation was 7 mN/m, corresponding to a mixed lipid expanded and condensed phase, versus 27 mN/m in our measurements, corresponding to an entirely condensed phase. Indeed, preliminary measurements (results not shown) revealed that at lower surface pressure the interaction may display very different characteristics.

6.4   Conclusion

The main results of this chapter are summarized in a schematic graphic. DP-TAP monolayers interact with carboxyl (-) NPs, but not with amidine (+) ones because of the electrostatic repulsion (figure 6.14). Carboxyl (-) NPs induce a local ordering of the lipid by pulling on the positive charge and stretching the lipid, decreasing its footprint. In the case of DPTAP, carboxyl (-) nanoparticles are able to bind directly to the choline charge group. As a result, no water is left between the lipid and the NP in fact, simulations with negatively charged NPs have shown that the binding can be so tight that the lipid membrane may follow the NPs curvature, in a process that may be the first stage of NP endocytosis [121]. The highly multivalent NPs even induce a charge inversion at the surface, resulting in an orientation inversion of the water molecules that can be observed in the SFG spectrum as a change of amplitude sign (figure 6.4, 6.5).

Similarly, DPPG monolayers interact with amidine (+) NPs, but not with carboxyl (-) ones (figure 6.15). However, in this case the water amplitude does

DPTAP

Figure 6.14. Schematic representation of the interfacial molecular structures during the DPTAP-nanoparticle interaction. Carboxyl-modified (-) particles bind to the monolayer and increase the lipid alkyl chain order.
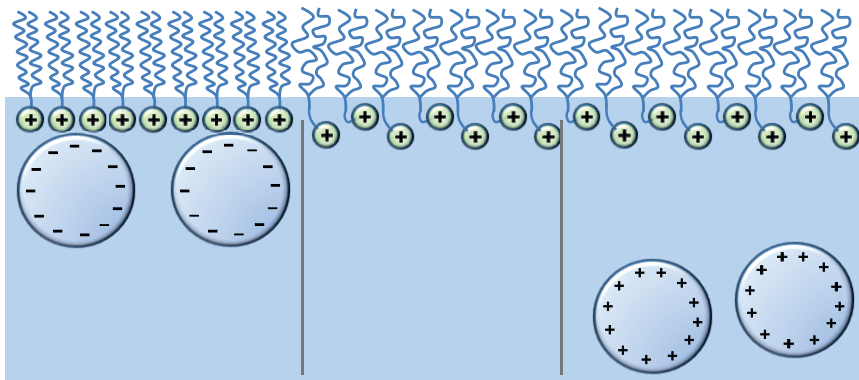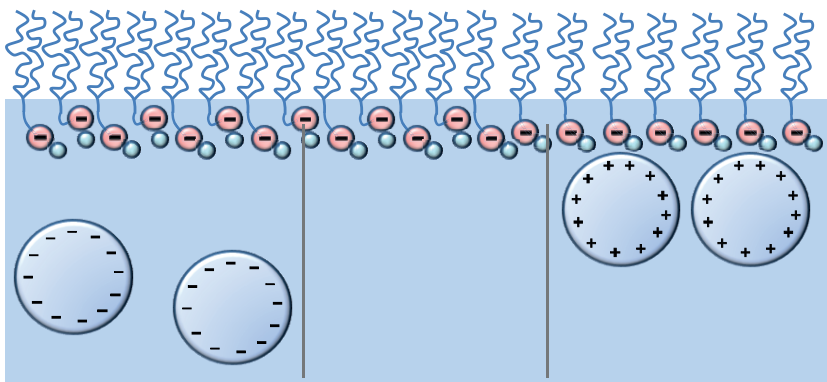
DPPG

Figure 6.15. Schematic representation of the interfacial molecular structures during the DPPG-nanoparticle interaction. Carboxyl-modified (-) particles bind to the monolayer.

not change sign: apparently even after NP binding there is water left between the lipid and the particle. This difference with DPTAP can be ascribed to the presence of the somewhat bulky glycerol group beneath the phosphate group of DPPG. This glycerol prevents the NPs to bind directly to the phosphate charge group, and leaves room for strongly aligned water molecules. The glycerol group

also adds to the lipid footprint area and prevents the pull of the charged NPs to fully straighten the lipid. This explains why the order parameter R does not increase for DPPG with amidine (+) NPs like it does for DPTAP with carboxyl (-) ones.
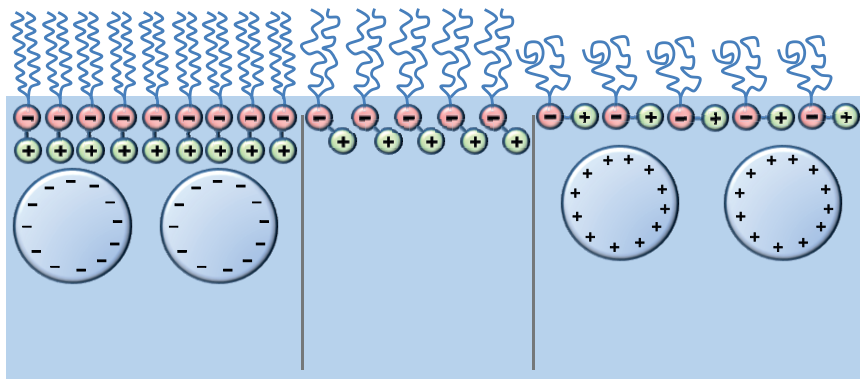
DPPC

FIGURE 6.16. Schematic representation of the interfacial molecular structures during the DPPG-nanoparticle interaction.

The DPPC interface is fundamentally different from the other two systems because a) the aligned water here is located between the charge groups of the lipid rather than below the lipids head group, and b) the head group dipole is able to move relative to the surface normal. The binding of carboxyl (-) NPs induces a pull on the positively charged choline group, stretching the lipid along the surface normal (figure 6.16, left). This causes the dipole projection on the surface normal to increase, and with it the average alignment of the interfacial water, which is detected as an increase of the water signal in the SFG spectrum. Possibly, aligned water underneath the NPs also contributes to this signal. The stretched lipid now has a lower footprint area and more ordered alkyl chains, as can be inferred from the increased order parameter R (figure 6.13, left panel).

The binding of amidine (+) nanoparticles induces a pull on the lipids negative choline group, aligning the head group dipole more parallel to the surface (figure 6.16, right). Since there is now no potential along the surface normal, no net water alignment is present and the SFG signal disappears almost entirely. The lipid footprint area increases and the alkyl chain order decreases, which is reflected in a significant drop of the order parameter R (figure 6.13, right panel). The water around the NPs, which are presumably not tightly bound to the head group due to the presence of the positive choline charge, is symmetrical and does not generate an SFG signal.

Summarizing, we have assessed vibrational SFG spectroscopy as a viable tool to study the interaction between charged nanoparticles and lipid membranes.

From the SFG spectra we were able to infer the location of the NPs relative to the membrane, the changes in water alignment due to the nanoparticles, and the changes in lipid head group and alkyl chain order upon the binding of NPs. SEM images provided further support for the hypotheses drawn from the SFG spectra. Several phenomena are briefly discussed that could have interesting follow-up studies. For one thing, the charged NPs were shown to aggregate at the inversely charged, but not at the zwitterionic lipid interface. Aggregation is an important factor in cytotoxicity of nanomaterials, because even if single particles are harmless, an aggregate may, due to its shape and size, display very different properties [149]. Note however that it cannot be ruled out that aggregation takes place only after deposition on the gold substrate and does not occur at the air-lipid-water interface.

Further, we have shown that the water intensity at saturated NP concentration is an indicator of the vicinity of the NPs to the lipid charge groups. Carboxyl (-) NPs caused charge inversion by tightly binding to a DPTAP monolayer, while amidine (+) NPs at a DPPG monolayer showed no reversal of water alignment. This use of water alignment as a probe of charge proximity and charge inversion may be refined and applied to a range of electrostatic interfacial interactions. Finally, having proven SFG spectroscopy to be an apt tool to probe the charged NP-lipid interaction, further NP parameters such as size, shape and hydrophobicity may be mapped, adding to the understanding of the influence of these factors on a molecular level and providing a link between molecular dynamics simulations and macroscopic observations.

7 A Molecular View of the Interaction of Carbon Nanotubes with Lipid Membranes

In this chapter we remain at the bio-nanointerface, now focusing on carbon nanotubes, and on the slow dynamics of their interaction with a monolayer. An important property of Single-Wall Carbon Nanotubes (SWNTs) is their ability to transgress the cell membrane. Most studies agree that functionalized nanotubes can be internalized into a cell by receptor-mediated endocytosis (RME, i.e. specific uptake) without damaging the membrane, while pristine nanotubes are likely to be cytotoxic. Although specific nanotube uptake has been studied extensively in in vivo systems, and simulations have covered the nonspecific case, a gap exists in our experimental knowledge of nonspecific interactions and the molecular processes involved. By means of a combination of tensiometry and surface-specific vibrational spectroscopy we elucidate the nonspecific interaction between a Langmuir lipid monolayer and DNA-covered carbon nanotubes and identify two separate stages in the interaction dynamics. In the first stage, the nanotubes bind to the lipid monolayer through electrostatic, nonspecific interactions mediated by the DNA molecules, which changes the interfacial water structure. The second stage comprises nanotubes being taken up into the hydrodrophobic region of the monolayer, reflected in changes in the lipid alkyl chain organization. A binding and dissociation model previously developed for RME describes our data well, revealing that the time constants of this nonspecific process are remarkably similar to those observed for the RME case. This similarity implies that cell-level observations are not necessarily sufficient to distinguish between different cell entry mechanisms, as is commonly assumed. Despite the apparently strong SWNT-monolayer interaction, vesicle leakage experiments reveal no rupture of lipid membranes of vesicles in the presence of SWNTs.

7.1   Introduction

Single-Wall Carbon Nanotubes (SWNTs) have been proposed as suitable candidates for transport of genetic material and drugs into cells in gene- and cancer therapy applications [62, 150, 151]. SWNTs are able to perform this task very efficiently because of their large surface area to which cargo molecules can be bonded noncovalently. The applicability of these functionalized SWNTs depends critically on their ability to cross the barrier formed by the cell membrane. As such, the interaction between SWNTs and the phospholipids and proteins that comprise the cell membrane is of great importance. Pristine nanotubes may aggregate and damage the cell membrane [149, 152], while functionalized SWNTs have been reported to enter cells spontaneously [153–155] and without any cytotoxic effects [119, 156, 157]. Particularly, for DNA-wrapped SWNTs, in vivo studies have shown the cell entry mechanism to be receptor-mediated endocytosis (RME) [158, 159]. Jin *et al.* have developed a model that includes the influence of particle size and shape on the endocytosis rate that accurately fits the observations from single particle tracking fluorescence microscopy [119]. Nonspecific interactions of SWNTs with the cell membrane, on the other hand, have been covered mostly by theory and simulations. SWNTs were shown to spontaneously insert into the hydrophobic alkyl chain region of a phospholipid bilayer [160], and this interaction, driven by unspecific van der Waals, steric, electrostatic and acid−base forces, was shown to be equal in strength to specific interactions [161]. Because specific and unspecific interaction strengths are comparable, it is important to recognize the role of processes other than RME, i.e. nonspecific interactions, in the SWNT-membrane interaction. While it may not significantly contribute to internalization of the SWNTs into cells, the nonspecific component could well play a significant role in SWNT cytotoxicity. In this study, we aim to experimentally address this issue by analyzing the nonspecific interaction between DNA-wrapped SWNTs and a single-lipid Langmuir monolayer acting as a model membrane. Using vibrational sum-frequency generation (SFG) spectroscopy, a powerful, non-invasive optical technique that is able to probe interfaces specifically, with a sensitivity to only a few molecular layers [25, 122, 162, 163], we characterized the dynamical behavior of the interfacial water and the lipids upon binding of SWNTs. Tensiometry provides additional information on the thermodynamics. For quantitative analysis, a binding-dissociation model was applied to describe the dynamics of the interaction. Finally, a membrane leakage experiment was performed to see if the strong observed interaction results in membrane rupture.

7.2   Methods

DNA-Wrapped SWNTs. Density gradient ultracentrifugation purified and (6,5) enriched DNA-SWNTs with an average length of 250 nm were used. $(GT)_{16}$ ssDNA is bound noncovalently to the SWNT surface [164]. A 20% surface coverage of ssDNA on the SWNTs and adsorption of ∼3 ssDNA molecules

per tube are estimated. The energetically highly favorable adsorption of ss-DNA to the SWNT surface prevents aggregation of SWNTs, while minimizing the presence of free ssDNA in the SWNT sample [165]. DNA-SWNTs were solvated in PBS buffer.

PBS Buffer.   Phosphate buffer was prepared by dissolving 0.12 g NaH_2PO_4 in 100 mL D_2O (Cambridge Isotope Laboratories, Inc, 99.93% purity). NaOH was added to a pH of 7.4.

Tensiometry.   In tensiometry, the two-dimensional pressure along the circumference of a needle tip is measured. This surface pressure is indicative of the surface free energy, which changes upon the binding or insertion of new molecules to or into an existing monolayer [129, 130]. Tensiometry measurements were performed using the Wilhelmy plate method (Kibron Inc.).

SFG Setup.   To obtain molecular-level insight into the interaction, we employ vibrational sum-frequency generation (SFG) spectroscopy. SFG spectroscopy is a technique that allows one to record the orientation and internal, conformational order of surface molecules [14]. SFG relies on the resonant enhancement of frequency mixing between visible (VIS) and infrared (IR) laser pulses when the infrared pulse is resonant with a surface vibration. Because it is an even-order ($\chi^{(2)}$) non-linear optical process, SFG is bulk-forbidden. The technique thus provides the vibrational spectrum of specifically the surface molecules with sensitivity generally unobtainable from conventional linear spectroscopies. As such, it has been used extensively to investigate bio-mimetic systems [25, 122, 133, 162, 163]. The setup and procedure to analyze the data are described in detail in previous publications [53, 54]. In brief, for our SFG experiments, we used a regeneratively amplified Ti:sapphire system (Legend, Coherent, Inc.) to produce pulses of 120 fs FWHM centered at 800 nm, with a 1 kHz repetition rate and a power of 2.5 W. 1 W of this output power was used to pump a tunable optical parametric amplifier system (TOPAS, Lights Conversion Inc.) to generate pulses at mid-infrared (IR) wavelengths. 0.5 W of the total 800 nm output was frequency-narrowed with an 25 cm^{-1} etalon and used as the upconverting (VIS) beam in the SFG experiment.
    Polarizers in the VIS and IR beam path were used to ensure detection of SF spectra in the SSP polarization (SF S polarized, VIS S polarized, and IR P polarized). The SSP polarization scheme produces the most intense SF response for the studied system.
$\lambda/2$ plates placed before the polarizers were used to adjust the power of the VIS and IR beams in order to prevent heating of the sample. Experiments were performed at a VIS power of 10 μJ per pulse and an IR power of 3.0-4.5 μJ.
The SF beam is focused onto a spectrograph (Princeton Instruments, Acton SP 2300) which is coupled to an Electron Multiplied Charge Coupled Device (EMCCD, Andor Technologies) for detection.

SFG procedure.   A home-built, Teflon coated 20 mL aluminum trough was used as a sample holder during the SFG experiments. A DPTAP monolayer

was prepared on the buffer subphase by dropcasting a solution of DPTAP in chloroform up to a surface pressure of 19 mN/m.

DNA-wrapped SWNTs in PBS buffer were injected underneath the DPTAP monolayer through a hole in the side of the trough to prevent disruption of the lipids. The substrate was stirred by a magnetic microstir during and after injection. SFG spectra were recorded before and at specific times after SWNT injection.

The frequency region of the SFG spectra is restricted by the bandwidth of the IR-pulse. In our setup the IR-pulse has a FWHM of $\sim$200 cm^{-1}. Since the region of interest ($\sim$ 2100-3100 cm^{-1}) is wider than the width of the IR-pulse the output frequency of the TOPAS was automatically tuned to produce IR pulses to cover the whole range. Spectra were recorded for 6 minutes each.

LUV preparation.   Large unilamellar vesicles (LUVs) were produced using the protocol described by Engel *et al.* [166] Briefly, 12.5 μmol DOPC was dissolved in 800 μL chloroform in a 10 mL glass tube. The solvent was evaporated by flushing with dry nitrogen and putting the tube in a vacuum desiccator for 20 minutes. The lipid film created in this process was dissolved in 0.5 mL PBS buffer pH 7.4 (prepared as described above) containing 50 mM calcein. The solution was left for at least 30 minutes to ensure complete hydration of the lipids, then frozen in liquid nitrogen and unfrozen in a water bath of $\sim$40°C. The latter step was repeated ten times. The solution was extruded through a filter holder (Liposofast, Avestin, Inc.) for at least eleven times, using filters with a pore diameter of 200 nm. Free calcein was extracted from the produced vesicles by using size-exclusion column chromatography (Sephadex G-50 fine) and elution with PBS buffer containing 100 mM NaCl.

Fluorometer.   A plate reader (Perkin Elmer VICTOR^3 Multilabel Counter) was used to measure fluorescence of the vesicles. 6 μL of the vesicle solution was added to 100 mM NaCl PBS buffer in wells of a 96 wells plate. After measuring fluorescence of the untreated vesicles, SWNTs in PBS buffer were added up to a final well volume of 200 μL and fluorescence was measured as a function of time. The plate was shaken just before each fluorescence measurement to mix the suspension. At the end of the experiment 15 μL 10% Triton X-100 (Sigma-Aldrich) was added to disintegrate the vesicles.

7.3   Results and discussion

Here, we use a bottom-up approach in which lipid monolayers of 1,2-dipalmitoyl-3-trimethylammonium-propane (DPTAP) and large unilamellar vesicles (LUVs) of 1,2-Dioleoyl-sn-Glycero-3-Phosphocholine (DOPC) lipid bilayers serve as simplified models for the complex multilipid bilayer of the cell membrane. (6,5)-SWNTs with an average length of 250 nm were made water-soluble by adhering single-stranded DNA (ssDNA). We employ vibrational sum-frequency generation (SFG) spectroscopy to directly probe the conformation and orientation of the lipids and water, and the changes therein upon nanotube adsorption. Ad-

ditionally, we performed surface tension measurements to investigate the thermodynamics of the lipid monolayer-SWNT interaction and membrane leakage experiments to investigate the occurrence of membrane rupture resulting from SWNT-phospholipid bilayer interaction.
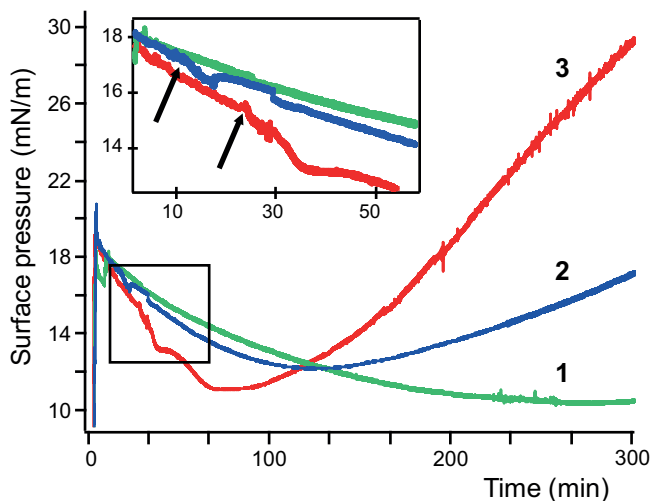

Figure 7.1. Surface pressure of DPTAP monolayers as a function of time. Trace 1: DPTAP is added to a buffered water-air interface to reach a surface pressure of 19 mN/m at t=∼5 minutes. Trace 2: DPTAP monolayer, DNA-SWNT solution is injected underneath the monolayer at the arrow-marked point to reach a SWNT concentration of the subphase of 40 pM. Trace 3: DPTAP monolayer, DNA-SWNT solution is injected at the arrow marked point to reach a SWNT concentration of the subphase of 160 pM.

Tensiometry. All measurements were performed at a temperature of 23±1°C, and an initial monolayer surface pressure of 19 mN/m. Figure 7.1 shows the time evolution of the surface pressure of a DPTAP monolayer during and after the injection of DNA-SWNTs into the sub-phase containing PBS buffer. The reference measurement (no SWNTs added; marked *1*), shows a slow decrease in surface pressure after adding the lipids to the water surface. This decrease is due to evaporation of water from the surface. The behavior is different when DNA-SWNTs are injected beneath the lipid monolayer (marked by arrows in Figure 7.1): minutes after injection of SWNTs underneath the monolayer, a small, concentration dependent dip in the surface pressure of the monolayer occurs. This dip is not observed after the injection of an equal amount of pure PBS buffer underneath a DPTAP monolayer (data not shown), indicating that it is due to the interaction between the lipid monolayer and the DNA-SWNTs. Moreover, at longer times the pressure *increases*, starting ∼100 minutes after SWNTs are added to the subphase.

The SWNT-induced decrease in surface pressure can be understood by the

local induction of gelled patches in the lipid monolayer through interactions
with the negatively charged DNA covering the SWNT. The formation of gelled
patches as a result of charged polystyrene nanoparticles interacting with DPPC
and DOPC vesicles was recently shown by Wang *et al.* [46] The presence of high-
density, immobilized patches will leave the monolayer area between the patches
less condensed, thereby decreasing the overall surface pressure. The subsequent
increase in surface pressure occurring after one or two hours (depending on the
precise SWNT concentration) must indicate a new stage in the interaction of the
DNA-SWNTs with the monolayer. As demonstrated below, a likely explanation
is the partial insertion of SWNTs into the monolayer.

Vibrational sum-frequency generation spectroscopy. SFG spec-
tra, normalized to a quartz reference, obtained after injecting DNA-wrapped
SWNTs in the buffered heavy water (D_2O) subphase are shown in figure 6.2a.
Heavy water was used for clearer separation of the different OD and CH reso-
nances, i.e. to circumvent complications in analysis due to overlap of the OH
and CH-stretch resonances.

The most prominent change in the spectra of figure 7.2a after adding
SWNTs is the decrease of the OD stretch intensity between 2000-2700 cm^{-1},
for convenience further referred to as two resonances ODν1 centered at $\sim$2350
cm^{-1} and ODν2 centered at $\sim$2500 cm^{-1}. Furthermore, the CH stretch re-
sponses are changing in time as well: first the CH$_3$ symmetric stretch (2880
cm^{-1}) and the CH$_3$ Fermi Resonance (2940 cm^{-1} intensities grow, while at later
times these decrease again. Simultaneously and in parallel the CH$_2$ symmetric
stretch (2850 cm^{-1}) intensity increases. Finally, around 2720 cm^{-1} a broad,
low intensity peak emerges.

To quantify the observed spectral changes, the SFG spectra were fitted by
assigning Lorentzian lineshapes to the CH modes and Voigt profiles to the water
bands [25, 63]. The relative intensity $I_{SF,n}$ of the nth Lorentzian resonance is
proportional to the square of the peak area A_n. Figure 7.2b shows this quantity
for the ODν1 and ODν2 OD stretch resonances of interfacial water at the
DPTAP monolayer. After adding DNA-SWNTs, the OD stretch resonances
decrease in time. Two effects may contribute to this decrease. Firstly, the pres-
ence of the negative charge at the interface disrupts the collective alignment
of resonant transition dipole moments induced by the positive headgroups of
DPTAP [34, 53, 167]. Such alignment increases the SFG response, as the SFG
selection rule requires that symmetry must be broken. The alignment caused
by this electrostatic interaction can be cancelled by the presence of the negative
charges on the ssDNA. Secondly, DNA-SWNTs at the interface displace water
molecules just underneath the monolayer, thereby effectively reducing the
number of water molecules contributing to the SFG response. While one might
expect the SWNT volume concentration at the interface to be low (given the
low bulk concentration), the observation that both the intensity *and* the shape
of the OD stretch resonances change in time (figure 7.2a) shows that both ef-
fects are operative here, since an overall decrease in alignment would only affect
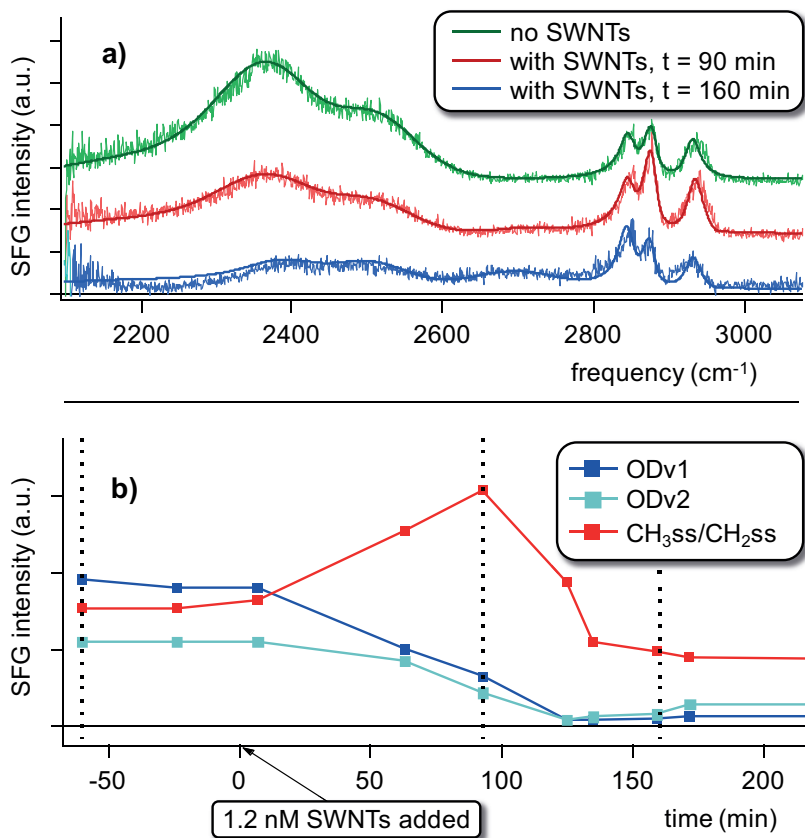
FIGURE 7.2. a) SFG spectra of a DPTAP monolayer (surface pressure 19 mN/m) before and at indicated times after injection of DNA-SWNTs in the subphase. Spectra have been offset for clarity. Solid curves are fits through the data. b) Time-dependent intensity of the two OD stretch peaks and the order parameter (I_{CH_3}/I_{CH_2}). The three vertical dashed lines correspond to the spectra shown in figure 7.2a.

the intensity. The shape change is reflected most notably in the appearance of a new OD peak around 2720 cm^{-1} after addition of DNA-SWNTs, as well as a blueshift of the ODν1 stretch peak. These results are reminiscent of earlier SFG studies concerning the interaction of lambda-phage DNA with DPTAP monolayers [53,54] and therefore illustrate the direct contact of DNA adsorbed on the SWNT surface with the lipid headgroups.

The conformation of lipids in the monolayer can be inferred from the CH peak intensity ratio in the SFG spectrum. A fully ordered monolayer, with all-trans CH$_2$ groups, has a practically centrosymmetric region of CH$_2$ bonds, and therefore these vibrations are not SFG active. However, the CH$_3$ end groups of the lipid tails in an ordered monolayer form a non-symmetric layer

along the surface normal, and, when the CH_3 groups are collectively aligned, these are highly SFG active. The ratio of the symmetric stretch intensities (I_{CH_3}/I_{CH_2}) therefore directly reflects the order in the alkyl chain of the lipid monolayer [18]. This order parameter is plotted in figure 7.2b as a function of time. Adding SWNTs underneath a DPTAP monolayer leads to an increase in order of the DPTAP monolayer during the first stage of the interaction. Remarkably, $\sim$100 minutes after the injection of DNA-SWNTs the lipid order decreases again, eventually to a value that is even lower than that before the addition of the nanotubes.

The initial increase in the order parameter implies that the interaction with the SWNTs cause the monolayer to become more condensed, without adding more lipids to the surface. This observation is in agreement with the formation of local condensed patches concluded from tensiometry measurements. Since the relative contribution of well-ordered lipids to the SFG signal is high (since the lipid molecules in these ordered patched are better mutually aligned), the existence of more condensed patches raises the overall order parameter. The monolayer was found to be spatially homogeneous, suggesting that condensed patches are small compared to the $\sim$100 μm diameter of the laser beam spot on the sample surface. This is in line with the notion that the condensed patches are only present at the DNA-SWNT-lipid interaction site, as postulated by Wang *et al.* [46]

The subsequent ($t \geq 100\ min$) decrease of the order parameter (I_{CH_3}/I_{CH_2}) towards a value lower than the original value (figure 7.2b) implies that the lipid monolayer becomes less ordered, despite the observed increase in surface pressure at these interaction times. The increase in surface pressure may be traced to either electrostatic interactions of the DNA-SWNTs with the lipid head groups or to DNA-SWNTs (partly) inserting into the hydrophobic region of the monolayer [130]. The observation that the OD stretch intensities ODν1 and ODν2 remain small and unchanged on this timescale (figure 7.2b), shows that the electrostatic interaction of the lipid head group with the DNA remains unchanged. Hence the likely explanation for the slow changes in both lipid structure and surface pressure are insertion of the SWNTs into the monolayer. This insertion into the environment of hydrophobic lipid tails requires the strongly hydrophobic surface of the SWNTs to be exposed. The long timescale is therefore attributed to the process of DNA uncovering the SWNTs . Every hydrophilic $(GT)_{16}$DNA strand possesses 32 sites to attach to the SWNT's surface through π-stacking interactions. Because of the numerous binding sides of DNA strands to the nanotube, the loosening of DNA molecules from the SWNT's surface is a slow process, even on the long timescales of the current study [168]. However, uncovering the SWNT surface does not require desorption of DNA from the SWNT. Given that only about 20% of the SWNTs is covered by DNA [160], a non-directional diffusive motion of DNA along the SWNT surface will be a much faster process, given the shallow potential energy surface at such an interface. We therefore suggest that an irreversible, stepwise

insertion into the hydrophobic alkyl chain region of the lipid monolayer occurs, with the SWNTs inserting a bit further every time a part their surface is bared by the random movement of the DNA strands. The observed interruption of the ordering of the monolayer through its CH vibrations in the SFG spectra is then likely explained by direct contact between the bare SWNT surface and the alkyl chains. The decrease in free energy that drives this process can be observed from the increase in surface pressure in the tensiometric measurements. In this picture loose DNA and parts of the SWNTs remain present just underneath the monolayer, thereby still suppressing the OD stretch intensities ODν1 and ODν2.
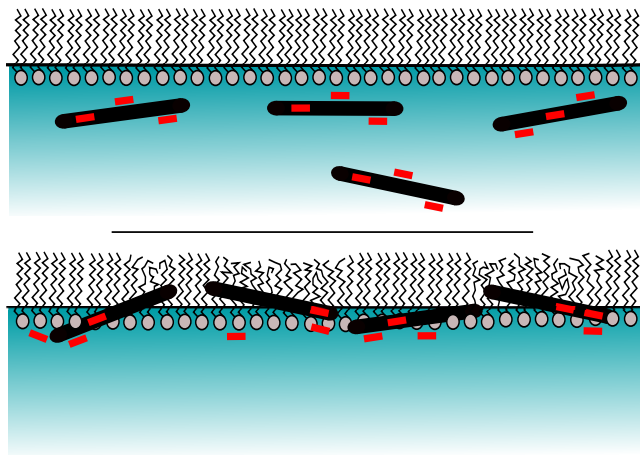

Figure 7.3. Schematic representation of the interaction of DNA-SWNTs (black rods covered with grey dashes) with a lipid monolayer (grey circles and chains). Two stages can be identified: first the interaction is mediated through DNA (upper panel), while at later times diffusion of DNA bares more of the SNWTs' surface which allows them to partially nestle within the lipids' hydrophobic alkyl chain region (lower panel).

Summarizing the long term effects, injection of DNA-SWNTs underneath a DPTAP monolayer leads to an increased surface pressure after several hours. The order of the lipid tails in the monolayer is disturbed and no significantly aligned water layer is detectable underneath the monolayer. A picture in which the gradual baring of the SWNT's surface of adsorbed DNA strands allows it to partially penetrate the monolayer explains all of these observations. The charged DNA strands are left below the hydrophobic alkyl chains, electrostatically bound to the monolayer in a manner similar to that previously described by Campen *et al.* [54] Figure 7.3 shows a schematic representation of the two stages of the interaction.

Binding and dissociation model. For further quantitative analysis, a model to describe the dynamical behavior observed in the SFG measurements is applied. To this end, we use the model that was originally developed for endocytosis of DNA-SWNTs [119]. While this may appear to be an entirely different

process, the dynamics can be described by equivalent parameters, as shown in
the following. The binding of the SWNTs to the membrane, promoted by elec-
trostatics in our experiments, is given by the rate k_a. Some of this binding may
be reversed at a dissociation rate k_r. At the same time, the endocytosis model
describes that the number of bound DNA-SWNT-receptor compounds disap-
pears and reappears through endocytosis and cellular expulsion at a rate k_e and
k_{rec}, respectively. While in our Langmuir monolayer system no endocytosis can
take place, the analogy is that nanotubes insert into the alkyl chain region of
the monolayer in a process that can be expected to be similar [160]. Hence, the
uptake of the bared SWNTs into hydrophobic region of the monolayer and the
possible expulsion from the hydrophobic region is described by the parameters
k_e and k_{rec}, respectively. We may then compose the following set of differential
equations for the concentration of SWNTs in the subphase $L(t)$, the number of
SWNTs bound to the monolayer $C_s(t)$, and the number of SWNTs embedded
in the monolayer $Ci(t)$:

$$\frac{\mathrm{d}L(t)}{\mathrm{d}t} = -k_a L(t) + k_r C_s(t) \tag{7.1}$$

$$\frac{\mathrm{d}C_s(t)}{\mathrm{d}t} = k_a L(t) - (k_r + k_e)C_s(t) + k_{rec}C_i(t) \tag{7.2}$$

$$\frac{\mathrm{d}C_i(t)}{\mathrm{d}t} = k_e C_s(t) - k_{rec}C_i(t) \tag{7.3}$$

We simplify the system by assigning an ingrowing constant concentration
to $L(t)$, which is reasonable given a) the observation from the SFG data that
the system reaches a steady state and b) the assumption that only a fraction
of the SWNTs interacts with the lipid membrane, as is known from similar
studies. [119, 159] A more detailed description can be found in the Supporting
Information. The parameters in this model can be related directly to the results
of the SFG measurements: firstly, the change in the total water signal (ODν1 +
ODν2) should be proportional to the square of the sum of the SWNT density at
the monolayer the density of bound SWNTs $C_s(t)$ and the number of SWNTs
embedded in the monolayer $C_i(t)$ since the DNA from these SWNTs is located
at the interface (note that, due to the coherent nature of the SFG approach,
the SFG intensity scales with the square of the interfacial number density).
Secondly, the order parameter (I_{CH_3}/I_{CH_2}) should increase with the square of
$C_s(t)$ because of lipid templating, but drop with the square of $C_i(t)$ because of
the disordering effect caused by SWNTs nestled in the alkyl chains. Equation
2 and 3 were solved numerically and fitted to our SFG data. Figure 7.4 shows
that this simple model provides a good description of the time-dependent SFG
intensities for the water and the methyl/methylene order parameter, with val-
ues for the rate parameters k_a , k_r, k_e and k_{rec} of 7.00×10^{-4}, 0.340, 0.100, and
9.68×10^{-2} per minute, respectively. For the first two of these parameters the
exact same values were used as in the studies by Jin et al., while the other two
were within a factor 3 to those used to describe endocytosis for DNA-SWNTs
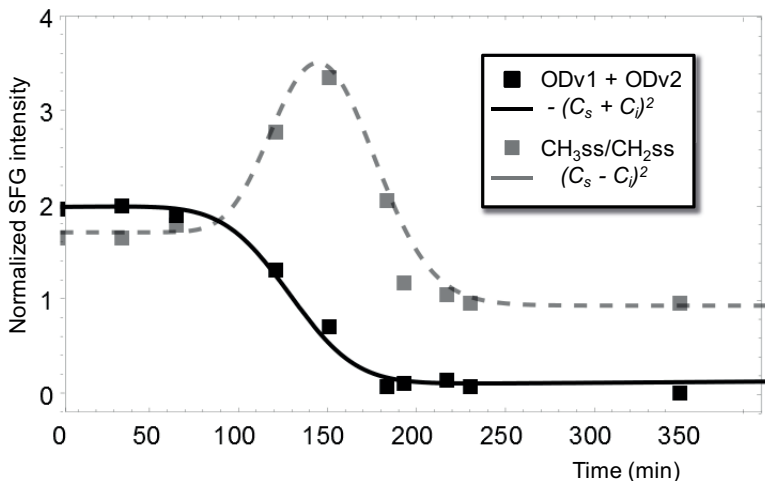
of equal size at similar concentration [119].

Figure 7.4. The data points of figure 7.2 fitted by the binding-dissociation model. Grey squares give the CH order parameter, black squares the water ODv1 + ODv2 peak.

From the model, further quantitative conclusions can be drawn. For instance, it predicts that $C_s(t)$ and $C_i(t)$ become equal at long time scales. This is consistent with the baring of the SWNT surface of DNA, since in that case the binding factor $C_s(t)$ would describe the DNA bound to the lipid head groups, and $C_i(t)$ a corresponding number of SWNTs nestled in the alkyl chain region. Furthermore, the model predicts that at this concentration 0.2 percent of the total DNA-SWNTs interact with the monolayer.

Membrane leakage experiment. The proposed insertion of SWNTs into the lipid monolayer can be expected to severely compromise the model membrane's integrity. Extrapolating this result to an in vivo system, such an interaction may damage the cell membrane to a point of rupture and leakage, as has been demonstrated before for antimicrobial peptides [130].

To check whether rearrangement of the lipid membrane by DNA-SWNTs disturbs it severely, a membrane leakage experiment was performed. Ideally, the vesicles used in this experiment would have been made of DPTAP for maximal consistency between experiments. However, due to the gel to liquid phase transition temperature of DPTAP of $\sim 45\,^\circ$C [169] it is not possible to form vesicles at 23 °C. To circumvent this complication, vesicles were prepared from DOPC, which has a comparable alkyl chain size to DPTAP, while its gel to liquid phase transition temperature of -12 °C [170] enables the formation of stable vesicles at room temperature. While DOPC is zwitterionic and DPTAP

cationic, the resulting decreased electrostatic interaction between DNA-SWNTs and the DOPC bilayer can be compensated by using a higher concentration of SWNTs [54].

DNA-wrapped SWNTs were added to a suspension of 200 nm diameter large unilamellar vesicles (LUVs) containing calcein, a fluorescent dye. Large unilamellar vesicles (LUVs) were produced through the protocol described by Engel *et al.* [166] Inside the vesicles, the calcein concentration is high, thereby quenching the fluorescence intensity [171]. If DNA-SWNTs induce membrane rupture, calcein molecules leak out of the vesicle's interior. The resulting dilution of the calcein solution then reduces self-quenching, and the observed macroscopic fluorescence increases.

Rather than finding the fluorescence increase associated with membrane rupture, the first observation after adding SWNTs to the suspension of DOPC vesicles is actually a two-step decrease of the fluorescence. An instantaneous, trivial decrease is present due to the linear absorption of (both exciting and fluorescence) radiation by the SWNTs. This factor is readily corrected for by calibrating the total fluorescence intensity to that observed after adding the surfactant Triton X-100 at the end of each measurement. This surfactant efficiently dissolves all LUVs, negating the self-quenching and causing a sharp increase in fluorescence. The correction factors are quantitatively consistent with a Lambert-Beer-like extinction behavior expected for a homogeneous suspension of nanotubes.
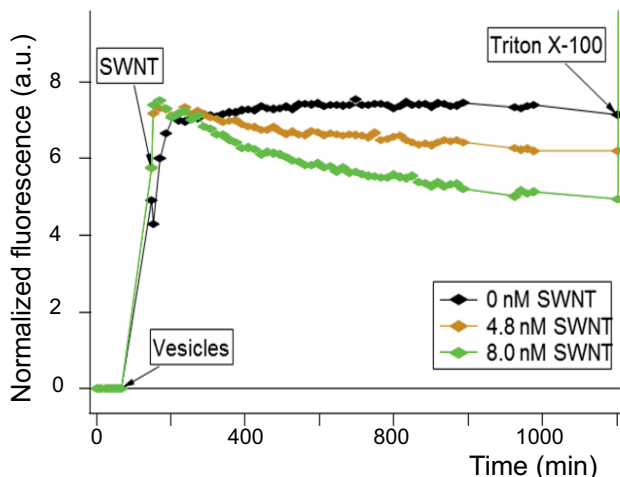

Figure 7.5. Results of membrane leakage experiment, normalized to maximal fluorescence = 1 for each sample. Arrows mark the addition of vesicles, SWNTs and Triton X-100. Solid lines are added for clarity.

More interesting is the slow decrease over ∼100's of minutes, which is faster and more pronounced at higher SWNT concentrations (7.5). This decrease in

fluorescence has to be caused by an interaction between LUVs and SWNTs, and can be explained in two ways. Firstly, SWNTs attaching to the vesicles will cause quenching of the excitation light due to co-localization of the semiconducting SWNTs and the trapped calcein. Energy transfer between carbon nanotubes and calcein could take place radiatively or through other intermolecular energy transfer pathways, given the nanometer-scale distance of donor and acceptor molecules. Secondly, the decrease in fluorescence may be explained by the transfer of phospholipids from the vesicle's membrane onto the SWNT surface. Lipids diffusing away from the vesicles' membrane along the SWNT would cause the vesicles to shrink, thus increasing the self-quenching effect and lowering the overall fluorescence. In either case, the SWNT induced decrease in fluorescence is testimony of the interaction of the SWNTs with the vesicle's membrane. It is evident that, despite this interaction, the LUVs remain intact, since the large fluorescence intensity increase associated with membrane rupture is clearly absent.

7.4   CONCLUSION

Adsorption of DNA-wrapped SWNTs to the surface of a DPTAP monolayer on a time scale of minutes was shown by tensiometry and Vibrational Sum Frequency spectroscopy. This interaction initiates the formation of local condensed patches within the DPTAP monolayer, as is shown by a decrease in surface pressure and an increase in the order of the lipids' alkyl chains through the order parameter extracted from the SFG spectra. Additionally, the interaction is accompanied by a strong perturbation of water molecules directly underneath the monolayer, indicating the presence of the DNA-SWNTs within the top few molecular layers of water.

On a longer timescale (hours), the injected SWNTs increase the surface pressure, while SFG shows a disordering of the alkyl chains. These observations are explained by (partial) penetration of SWNTs into the DPTAP monolayer. The results suggest that the DNA strands on the SWNTs are rearranged or loosened in a slow thermodynamic equilibration process that bares more and more of the SWNTs hydrophobic surface. The total free energy at the interfacial system decreases when parts of SWNTs' surface interact with the lipids' alkyl chains. The negatively charged DNA remains electrostatically bound to the positively charged lipid headgroup, as can be inferred from the persisting lowered water signal in the SFG spectra. A simple model of reversible adsorption and insertion into the lipid hydrophobic region reproduces the observed kinetics very well, with parameters that are remarkably similar to those inferred previously for specific interactions. This result shows that for this system specific interactions are not necessarily stronger than unspecific ones.

The possible rupture of a model membrane through this interaction was probed by adsorbing DNA-SWNTs to DOPC vesicles containing fluorescent molecules. While significant interaction between the DNA-SWNTs and the vesicles was apparent by the SWNT-induced quenching of fluorescence, the

membrane remained intact.

Our results provide a solid base for further quantitative research regarding the interaction of SWNTs and lipids, focusing both on the molecular-scale interactions and their emerging macroscopic phenomena.

7.5   Supporting information

The model described by solving equations 1−3 describes the process of DNA-SWNTs binding to the lipid membrane, and the subsequent uptake of SWNTs into the membrane, each governed by rate constants k that represent the probability of binding or dissociation taking place in. As such, $L(t)$, $C_s(t)$, and $C_i(t)$ are dimensionless while the rate constants are given in units of min^{-1}. In the study by Jin *et al.* where this model was applied to describe the endocytosis of DNA-SWNTs, $L(t)$ was chosen to have a Gaussian time profile, corresponding for the growth and decay of the SWNT concentration in a perfusion experiment. However, in this study the SWNTs are injected into a non-flowing subphase and stirred, an ingrowing constant, i.e. sigmoid function is more suited. To describe the ingrowth, which is governed by both non-directional diffusion and electrostatic attraction of the DNA-SWNTs towards the cationic lipid monolayer, we choose a Gauss error function that is commonly applied in statistical distributions:

$$L(t) = L_0 \left(1 + \text{erf}(Dt)\right) \tag{7.4}$$

with L_0 the equilibrium concentration and the prefactor $D = 0.033$ a diffusion constant found through fitting determining the ingrowth rate, and with

$$\text{erf}(x) = \frac{2}{\sqrt{\pi}} \int_0^x e^{-y^2} dy \tag{7.5}$$

Having thus defined $L(t)$, we can numerically solve equations 2 and 3 to find $C_s(t)$ and $C_i(t)$ with boundary conditions $C_s(0) = C_i(0) = 0$.
In this study, the model is used to described the dynamics of the order parameter R deduced from the fitted SFG intensities. Since these intensities are observed to change in time, we can define $R(t)$ as

$$R(t) = \frac{I_{CH_3}(t)}{I_{CH_2}(t)} \tag{7.6}$$

As discussed in the main text, the binding and dissociation model describes the dynamics of $R(t)$ through the relation

$$R(t) = R_0 + A\sqrt{C_s(t)} - B\sqrt{C_i(t)}, \tag{7.7}$$

Where R_0 is the order parameter of the lipid monolayer before adding SWNTs, and A and B are scaling factors describing the relative effect of DNA-SWNT binding and SWNT nestling on the order parameter $R(t)$. We found the model to fit the data for $A = B$, implying that binding and nestling of a single nanotube have an equal but opposite effect in the order of the alkyl chains.

Bibliography

1. The electromagnetic spectrum. Image available from: http://www.windowimage.sg/images/electromagnetic-spectrum.png.

2. P. A. Franken, A. E. Hill, C. W. Peters, and G. Weinreich. Generation of optical harmonics. *Physical Review Letters*, 7(4):118–119, 1961.

3. K. E. Rieckhoff and W. L. Peticolas. Optical second-harmonic generation in crystalline amino acids. *Science (New York, N.Y.)*, 147(3658):610–1, 1965.

4. A. J. Demaria, D. A. Stetser, and Jr. Glenn, W. H. Ultrashort light pulses. *Science (New York, N.Y.)*, 156(3782):1557–68, 1967.

5. S. Fine and W. P. Hansen. Optical second harmonic generation in biological systems. *Applied optics*, 10(10):2350–3, 1971.

6. J. D. Victor, R. M. Shapley, and B. W. Knight. Nonlinear analysis of cat retinal ganglion cells in the frequency domain. *Proceedings of the National Academy of Sciences of the United States of America*, 74(7):3068–72, 1977.

7. C. K. Chen, A. R. de Castro, and Y. R. Shen. Coherent second-harmonic generation by counterpropagating surface plasmons. *Optics Letters*, 4(12):393–393, 1979.

8. W. Jamroz, P. E. Larocque, and B. P. Stoicheff. Resonantly enhanced second-harmonic generation in zinc vapor. *Optics Letters*, 7(4):148–50, 1982.

9. M. De Micheli, J. Botineau, S. Neveu, P. Sibillot, D. B. Ostrowsky, and M. Papuchon. Extension of second-harmonic phase-matching range in lithium niobate guides. *Optics Letters*, 8(2):116–8, 1983.

10. T. Y. Fan, C. E. Huang, B. Q. Hu, R. C. Eckardt, Y. X. Fan, R. L. Byer, and R. S. Feigelson. Second harmonic generation and accurate index of refraction measurements in flux-grown ktiopo(4). *Applied optics*, 26(12):2390–4, 1987.

11. U. Osterberg and W. Margulis. Experimental studies on efficient frequency doubling in glass optical fibers. *Optics Letters*, 12(1):57–9, 1987.

12. J. S. Schildkraut, T. L. Penner, C. S. Willand, and A. Ulman. Absorption and 2nd-harmonic generation of monomer and aggregate hemicyanine dye in langmuir-blodgett films. *Optics Letters*, 13(2):134–136, 1988.

13. G. T. Boyd, Y. R. Shen, and T. W. Hansch. Continuous-wave second-harmonic generation as a surface microprobe. *Optics Letters*, 11(2):97, 1986.

14. Y. R. Shen. Surface-properties probed by 2nd-harmonic and sum-frequency generation. *Nature*, 337(6207):519–525, 1989.

15. Q. Hu, J. S. Dam, C. Pedersen, and P. Tidemand-Lichtenberg. High-resolution mid-ir spectrometer based on frequency upconversion. *Optics Letters*, 37(24):5232–5234, 2012.

16. P. Guyotsionnest, R. Superfine, J. H. Hunt, and Y. R. Shen. Vibrational spectroscopy of a silane monolayer at air solid and liquid solid interfaces using sum-frequency generation. *Chemical Physics Letters*, 144(1):1–5, 1988.

17. R. Superfine, J. Y. Huang, and Y. R. Shen. Nonlinear optical studies of the pure liquid vapor interface - vibrational-spectra and polar ordering. *Physical Review Letters*, 66(8):1066–1069, 1991.

18. R. A. Walker, J. A. Gruetzmacher, and G. L. Richmond. Phosphatidyl-choline monolayer structure at a liquid-liquid interface. *Journal of the American Chemical Society*, 120(28):6991–7003, 1998.

19. Mikhail Vinaykin and Alexander V. Benderskii. Vibrational sum-frequency spectrum of the water bend at the air/water interface. *Journal of Physical Chemistry Letters*, 3(22):3348–3352, 2012.

20. Ran-ran Feng, Yuan Guo, Rong Lue, Luis Velarde, and Hong-fei Wang. Consistency in the sum frequency generation intensity and phase vibrational spectra of the air/neat water interface. *Journal of Physical Chemistry A*, 115(23):6015–6027, 2011.

21. J. Noah-Vanhoucke, J. D. Smith, and P. L. Geissler. Toward a simple molecular understanding of sum frequency generation at air-water interfaces. *Journal of Physical Chemistry B*, 113(13):4065–4074, 2009.

22. W. Gan, D. Wu, Z. Zhang, Y. Guo, and H. F. Wang. Orientation and motion of water molecules at air/water interface. *Chinese Journal of Chemical Physics*, 19(1):20–24, 2006.

23. Satoshi Nihonyanagi, Tatsuya Ishiyama, Touk-kwan Lee, Shoichi Yamaguchi, Mischa Bonn, Akihiro Morita, and Tahei Tahara. Unified molecular view of the air/water interface based on experimental and theoretical chi2 spectra of an isotopically diluted water surface. *Journal of the American Chemical Society*, 133(42):16875–16880, 2011.

24. M. Sovago, R. K. Campen, G. W. H. Wurpel, M. Muller, H. J. Bakker, and M. Bonn. Vibrational response of hydrogen-bonded interfacial water is dominated by intramolecular coupling. *Physical Review Letters*, 100(17), 2008.

25. Q. Du, R. Superfine, E. Freysz, and Y. R. Shen. Vibrational spectroscopy of water at the vapor/water interface. *Physical Review Letters*, 70(15):2313, 1993.

26. P. B. Miranda and Y. R. Shen. Liquid interfaces: A study by sum-frequency vibrational spectroscopy. *Journal of Physical Chemistry B*, 103(17):3292–3307, 1999.

27. F. Vidal and A. Tadjeddine. Sum-firequency generation spectroscopy of interfaces. *Reports on Progress in Physics*, 68(5):1095–1127, 2005.

28. Adam J. Hopkins, Cathryn L. McFearin, and Geraldine L. Richmond. Investigations of the solid-aqueous interface with vibrational sum-frequency spectroscopy. *Current Opinion in Solid State and Materials Science*, 9(1-2):19–27, 2005.

29. J. F. D. Liljeblad and E. Tyrode. Vibrational sum frequency spectroscopy studies at solid/liquid interfaces: Influence of the experimental geometry in the spectral shape and enhancement. *Journal of Physical Chemistry C*, 116(43):22893–22903, 2012.

30. W. Sung, D. Kim, and Y. R. Shen. Sum-frequency vibrational spectroscopic studies of langmuir monolayers. *Current Applied Physics*, 13(4):619–632, 2013.

31. W. Gan, D. Wu, Z. Zhang, R. R. Feng, and H. F. Wang. Polarization and experimental configuration analyses of sum frequency generation vibrational spectra, structure, and orientational motion of the air/water interface. *Journal of Chemical Physics*, 124(11), 2006.

32. Y. R. Shen and V. Ostroverkhov. Sum-frequency vibrational spectroscopy on water interfaces: Polar orientation of water molecules at interfaces. *Chemical Reviews*, 106(4):1140–1154, 2006.

33. I. V. Stiopkin, H. D. Jayathilake, A. N. Bordenyuk, and A. V. Benderskii. Heterodyne-detected vibrational sum frequency generation spectroscopy. *Journal of the American Chemical Society*, 130(7):2271–2275, 2008.

34. Satoshi Nihonyanagi, Shoichi Yamaguchi, and Tahei Tahara. Direct evidence for orientational flip-flop of water molecules at charged interfaces: A heterodyne-detected vibrational sum frequency generation study. *Journal of Chemical Physics*, 130(20):204704–1–5, 2009.

35. Xiangke Chen, Wei Hua, Zishuai Huang, and Heather C. Allen. Interfacial water structure associated with phospholipid membranes studied by phase-sensitive vibrational sum frequency generation spectroscopy. *Journal of the American Chemical Society*, 132(32):11336–11342, 2010.

36. Jahur A. Mondal, Satoshi Nihonyanagi, Shoichi Yamaguchi, and Tahei Tahara. Structure and orientation of water at charged lipid monolayer/water interfaces probed by heterodyne-detected vibrational sum frequency generation spectroscopy. *Journal of the American Chemical Society*, 132(31):10656–10657, 2010.

37. Avishek Ghosh, Marc Smits, Jens Bredenbeck, Niels Dijkhuizen, and Mischa Bonn. Femtosecond time-resolved and two-dimensional vibrational sum frequency spectroscopic instrumentation to study structural dynamics at interfaces. *Review of Scientific Instruments*, 79(9), 2008.

38. Yi Rao, Daohua Song, Nicholas J. Turro, and Kenneth B. Eisenthal. Orientational motions of vibrational chromophores in molecules at the air/water interface with time-resolved sum frequency generation. *Journal of Physical Chemistry B*, 112(43):13572–13576, 2008.

39. Grace Y. Stokes, Avram M. Buchbinder, Julianne M. Gibbs-Davis, Karl A. Scheidt, and Franz M. Geiger. Chemically diverse environmental interfaces and their reactions with ozone studied by sum frequency generation. *Vibrational Spectroscopy*, 50(1):86–98, 2009.

40. Heike Arnolds and Mischa Bonn. Ultrafast surface vibrational dynamics. *Surface Science Reports*, 65(2):45–66, 2010.

41. Ali Eftekhari-Bafrooei and Eric Borguet. Effect of hydrogen-bond strength on the vibrational relaxation of interfacial water. *Journal of the American Chemical Society*, 132(11):3756–3761, 2010.

42. Jennifer E. Laaser, Wei Xiong, and Martin T. Zanni. Time-domain sfg spectroscopy using mid-ir pulse shaping: Practical and intrinsic advantages. *Journal of Physical Chemistry B*, 115(11):2536–2546, 2011.

43. Zhen Zhang, Lukasz Piatkowski, Huib J. Bakker, and Mischa Bonn. Communication: Interfacial water structure revealed by ultrafast two-dimensional surface vibrational spectroscopy. *Journal of Chemical Physics*, 135(2), 2011.

44. Zhen Zhang, Lukasz Piatkowski, Huib J. Bakker, and Mischa Bonn. Ultrafast vibrational energy transfer at the water/air interface revealed by two-dimensional surface vibrational spectroscopy. *Nature Chemistry*, 3(11):888–893, 2011.

45. Prashant Chandra Singh, Satoshi Nihonyanagi, Shoichi Yamaguchi, and Tahei Tahara. Ultrafast vibrational dynamics of water at a charged interface revealed by two-dimensional heterodyne-detected vibrational sum frequency generation. *Journal of Chemical Physics*, 137(9), 2012.

46. B. Wang, L. F. Zhang, S. C. Bae, and S. Granick. Nanoparticle-induced surface reconstruction of phospholipid membranes. *Proceedings*

of the National Academy of Sciences of the United States of America, 105(47):18171–18175, 2008.

47. Karen M. Callahan, Nadia N. Casillas-Ituarte, Man Xu, Martina Roeselova, Heather C. Allen, and Douglas J. Tobias. Effect of magnesium cation on the interfacial properties of aqueous salt solutions. *Journal of Physical Chemistry A*, 114(32):8359–8368, 2010.

48. Wei Hua, Xiangke Chen, and Heather C. Allen. Phase-sensitive sum frequency revealing accommodation of bicarbonate ions, and charge separation of sodium and carbonate ions within the air/water interface. *Journal of Physical Chemistry A*, 115(23):6233–6238, 2011.

49. Yi Rao, Mahamud Subir, Eric A. McArthur, Nicholas J. Turro, and Kenneth B. Eisenthal. Organic ions at the air/water interface. *Chemical Physics Letters*, 477(4-6):241–244, 2009.

50. M. J. Shultz, C. Schnitzer, D. Simonelli, and S. Baldelli. Sum frequency generation spectroscopy of the aqueous interface: ionic and soluble molecular solutions. *International Reviews in Physical Chemistry*, 19(1):123–153, 2000.

51. Maria Sovago, George W. H. Wurpel, Marc Smits, Michiel Muller, and Mischa Bonn. Calcium-induced phospholipid ordering depends on surface pressure. *Journal of the American Chemical Society*, 129(36):11079–11084, 2007.

52. Nadia N. Casillas-Ituarte, Xiangke Chen, Hardy Castada, and Heather C. Allen. Na+ and ca2+ effect on the hydration and orientation of the phosphate group of dppc at air-water and air-hydrated silica interfaces. *Journal of Physical Chemistry B*, 114(29):9485–9495, 2010.

53. George W. H. Wurpel, Maria Sovago, and Mischa Bonn. Sensitive probing of dna binding to a cationic lipid monolayer. *Journal of the American Chemical Society*, 129(27):8420–+, 2007.

54. R. Kramer Campen, Thuy T. M. Ngo, Maria Sovago, Jean-Marie Ruysschaert, and Mischa Bonn. Molecular restructuring of water and lipids upon the interaction of dna with lipid monolayers. *Journal of the American Chemical Society*, 132(23):8037–8047, 2010.

55. Xiaoyun Chen and Zhan Chen. Sfg studies on interactions between antimicrobial peptides and supported lipid bilayers. *Biochimica Et Biophysica Acta-Biomembranes*, 1758(9):1257–1273, 2006.

56. X. Y. Chen, M. L. Clarke, J. Wang, and Z. Chen. Sum frequency generation vibrational spectroscopy studies on molecular conformation and orientation of biological molecules at interfaces. *International Journal of Modern Physics B*, 19(4):691–713, 2005.

57. J. Wang, M. A. Even, X. Y. Chen, A. H. Schmaier, J. H. Waite, and Z. Chen. Detection of amide i signals of interfacial proteins in situ using sfg. *Journal of the American Chemical Society*, 125(33):9914–9915, 2003.

58. J. Kim and G. A. Somorjai. Molecular packing of lysozyme, fibrinogen, and bovine serum albumin on hydrophilic and hydrophobic surfaces studied by infrared-visible sum frequency generation and fluorescence microscopy. *Journal of the American Chemical Society*, 125(10):3150–3158, 2003.

59. O. Mermut, D. C. Phillips, R. L. York, K. R. McCrea, R. S. Ward, and G. A. Somorjai. In situ adsorption studies of a 14-amino acid leucine-lysine peptide onto hydrophobic polystyrene and hydrophilic silica surfaces using quartz crystal microbalance, atomic force microscopy, and sum frequency generation vibrational spectroscopy. *Journal of the American Chemical Society*, 128(11):3598–3607, 2006.

60. C. Buzea, II Pacheco, and K. Robbie. Nanomaterials and nanoparticles: Sources and toxicity. *Biointerphases*, 2(4):MR17–MR71, 2007.

61. A. Verma, O. Uzun, Y. H. Hu, Y. Hu, H. S. Han, N. Watson, S. L. Chen, D. J. Irvine, and F. Stellacci. Surface-structure-regulated cell-membrane penetration by monolayer-protected nanoparticles. *Nature Materials*, 7(7):588–595, 2008.

62. W. Cheung, F. Pontoriero, O. Taratula, A. M. Chen, and H. X. He. Dna and carbon nanotubes as medicine. *Advanced Drug Delivery Reviews*, 62(6):633–649, 2010.

63. A. G. Lambert, P. B. Davies, and D. J. Neivandt. Implementing the theory of sum frequency generation vibrational spectroscopy: A tutorial review. *Applied Spectroscopy Reviews*, 40(2):103–145, 2005.

64. R. W. Boyd. *Nonlinear Optics*. Academic Press, San Diego, 3rd edition, 2008.

65. Y. R. Shen. *The Principles of Nonlinear Optics*. Wiley, New York, 1st edition, 1984.

66. C. Hirose, N. Akamatsu, and K. Domen. Formulas for the analysis of the surface sfg spectrum and transformation coefficients of cartesian sfg tensor components. *Applied Spectroscopy*, 46(6):1051–1072, 1992.

67. M. Sovago, E. Vartiainen, and M. Bonn. Determining absolute molecular orientation at interfaces: A phase retrieval approach for sum frequency generation spectroscopy. *Journal of Physical Chemistry C*, 113(15):6100–6106, 2009.

68. P. Hamm, R. A. Kaindl, and J. Stenger. Noise suppression in femtosecond mid-infrared light sources. *Optics Letters*, 25(24):1798–1800, 2000.

69. Ellen H. G. Backus, Daniel Bonn, Sophie Cantin, Sylvie Roke, and Mischa Bonn. Laser-heating-induced displacement of surfactants on the water surface. *The Journal of Physical Chemistry B*, 116(9):2703–2712, 2012.

70. M. Smits, M. Sovago, G. W. H. Wurpel, D. Kim, M. Mller, and M. Bonn. Polarization-resolved broad-bandwidth sum-frequency generation spectroscopy of monolayer relaxation. *Journal of Physical Chemistry C*, 111(25):8878–8883, 2007.

71. Y. S. Badyal, D. L. Price, M. L. Saboungi, D. R. Haeffner, and S. D. Shastri. Quantum effects on the structure of water at constant temperature and constant atomic density. *Journal of Chemical Physics*, 116(24):10833–10837, 2002.

72. H. A. Stern and B. J. Berne. Quantum effects in liquid water: Path-integral simulations of a flexible and polarizable ab initio model. *Journal of Chemical Physics*, 115(16):7622–7628, 2001.

73. B. Chen, I. Ivanov, M. L. Klein, and M. Parrinello. Hydrogen bonding in water. *Physical Review Letters*, 91(21), 2003.

74. Y. M. Efimova, S. Haemers, B. Wierczinski, W. Norde, and A. A. van Well. Stability of globular proteins in H_2O and D_2O. *Biopolymers*, 85(3):264–273, 2007.

75. B. Pamuk, J. M. Soler, R. Ramirez, C. P. Herrero, P. W. Stephens, P. B. Allen, and M. V. Fernandez-Serra. Anomalous nuclear quantum effects in ice. *Physical Review Letters*, 108(19), 2012.

76. Francesco Paesani and Gregory A. Voth. The properties of water: Insights from quantum simulations. *Journal of Physical Chemistry B*, 113(17):5702–5719, 2009.

77. E. A. Raymond, T. L. Tarbuck, M. G. Brown, and G. L. Richmond. Hydrogen-bonding interactions at the vapor/water interface investigated by vibrational sum-frequency spectroscopy of $HOD/H_2O/D_2O$ mixtures and molecular dynamics simulations. *Journal of Physical Chemistry B*, 107(2):546–556, 2003.

78. Chuan-Shan Tian and Y. Ron Shen. Isotopic dilution study of the water/vapor interface by phase-sensitive sum-frequency vibrational spectroscopy. *Journal of the American Chemical Society*, 131(8):2790–+, 2009.

79. Piotr A. Pieniazek, Craig J. Tainter, and James L. Skinner. Surface of liquid water: Three-body interactions and vibrational sum-frequency spectroscopy. *Journal of the American Chemical Society*, 133(27):10360–10363, 2011.

80. Igor V. Stiopkin, Champika Weeraman, Piotr A. Pieniazek, Fadel Y. Shalhout, James L. Skinner, and Alexander V. Benderskii. Hydrogen bonding at the water surface revealed by isotopic dilution spectroscopy. *Nature*, 474(7350):192–195, 2011.

81. David Chandler and Peter G. Wolynes. Exploiting the isomorphism between quantum theory and classical statistical mechanics of polyatomic fluids. *The Journal of Chemical Physics*, 74(7):4078–4095, 1981.

82. Michele Ceriotti, Michele Parrinello, Thomas E. Markland, and David E. Manolopoulos. Efficient stochastic thermostatting of path integral molecular dynamics. *Journal of Chemical Physics*, 133(12), 2010.

83. Tatsuya Ishiyama and Akihiro Morita. Molecular dynamics study of gas-liquid aqueous sodium halide interfaces. i. flexible and polarizable molecular modeling and interfacial properties. *Journal of Physical Chemistry C*, 111(2):721–737, 2007.

84. I. F. W. Kuo and C. J. Mundy. An ab initio molecular dynamics study of the aqueous liquid-vapor interface. *Science*, 303(5658):658–660, 2004.

85. Thomas E. Markland and B. J. Berne. Unraveling quantum mechanical effects in water using isotopic fractionation. *Proceedings of the National Academy of Sciences of the United States of America*, 109(21):7988–7991, 2012.

86. A. K. Soper and C. J. Benmore. Quantum differences between heavy and light water. *Physical Review Letters*, 101(6), 2008.

87. U. Bergmann, D. Nordlund, Ph Wernet, M. Odelius, L. G. M. Pettersson, and A. Nilsson. Isotope effects in liquid water probed by x-ray raman spectroscopy. *Physical Review B*, 76(2), 2007.

88. F. O. Libnau, A. A. Christy, and O. M. Kvalheim. Determination of the equilibrium-constant and resolution of the hod spectrum by alternating least-squares and infrared-analysis. *Applied Spectroscopy*, 49(10):1431–1437, 1995.

89. R. P. Feynman. Space-time approach to non-relativistic quantum mechanics. *Reviews of Modern Physics*, 20(2):367–387, 1948.

90. B. M. Auer and J. L. Skinner. Vibrational sum-frequency spectroscopy of the liquid/vapor interface for dilute hod in d(2)o. *Journal of Chemical Physics*, 129(21), 2008.

91. A. Morita and J. T. Hynes. A theoretical analysis of the sum frequency generation spectrum of the water surface. *Chemical Physics*, 258(2-3):371–390, 2000.

92. Dave S. Walker, Dennis K. Hore, and Geraldine L. Richmond. Understanding the population, coordination, and orientation of water species contributing to the nonlinear optical spectroscopy of the vapor-water interface through molecular dynamics simulations. *Journal of Physical Chemistry B*, 110(41):20451–20459, 2006.

93. Marc Smits, Avishek Ghosh, Martin Sterrer, Michiel Muller, and Mischa Bonn. Ultrafast vibrational energy transfer between surface and bulk water at the air-water interface. *Physical Review Letters*, 98(9), 2007.

94. N. Ji, V. Ostroverkhov, C. S. Tian, and Y. R. Shen. Characterization of vibrational resonances of water-vapor interfaces by phase-sensitive sum-frequency spectroscopy. *Physical Review Letters*, 100(9), 2008.

95. L. Piatkowski, K. B. Eisenthal, and H. J. Bakker. Ultrafast intermolecular energy transfer in heavy water. *Physical Chemistry Chemical Physics*, 11(40):9033–9038, 2009.

96. K. B. Eisenthal. Liquid interfaces probed by second-harmonic and sum-frequency spectroscopy. *Chemical Reviews*, 96(4):1343–1360, 1996.

97. Y. R. Shen. Wave mixing spectroscopy for surface studies. *Solid State Communications*, 102(2-3):221–229, 1997.

98. H. C. Allen, E. A. Raymond, and G. L. Richmond. Non-linear vibrational sum frequency spectroscopy of atmospherically relevant molecules at aqueous solution surfaces. *Current Opinion in Colloid and Interface Science*, 5(1-2):74–80, 2000.

99. S. Gopalakrishnan, D. Liu, H. C. Allen, M. Kuo, and M. J. Shultz. Vibrational spectroscopic studies of aqueous interfaces: Salts, acids, bases, and nanodrops. *Chemical Reviews*, 106(4):1155–1175, 2006.

100. C. Aliaga, C. S. Santos, and S. Baldelli. Surface chemistry of room-temperature ionic liquids. *Physical Chemistry Chemical Physics*, 9(28):3683–3700, 2007.

101. S. Yamaguchi and T. Tahara. Novel interface-selective even-order nonlinear spectroscopy. *Laser and Photonics Reviews*, 2(1-2):74–82, 2008.

102. G. A. Somorjai, H. Frei, and J. Y. Park. Advancing the frontiers in nanocatalysis, biointerfaces, and renewable energy conversion by innovations of surface techniques. *Journal of the American Chemical Society*, 131(46):16589–16605, 2009.

103. V. Ostroverkhov, G. A. Waychunas, and Y. R. Shen. New information on water interfacial structure revealed by phase-sensitive surface spectroscopy. *Physical Review Letters*, 94(4), 2005.

104. N. Bloembergen and P. S. Pershan. Light waves at the boundary of non-linear media. *Physical Review*, 128(2):606–622, 1962.

105. K. Kemnitz, K. Bhattacharyya, J. M. Hicks, G. R. Pinto, B. Eisenthal, and T. F. Heinz. The phase of second-harmonic light generated at an interface and its relation to absolute molecular orientation. *Chemical Physics Letters*, 131(4-5):285–290, 1986.

106. R. Lu, Y. Rao, W. K. Zhang, and H. F. Wang. Phase measurement in nonlinear optics of molecules at air/water interface with femtosecond laser pulses. In *Proceedings of SPIE - The International Society for Optical Engineering*, volume 4812, pages 115–124, 2002.

107. B. M. Auer and J. L. Skinner. Vibrational sum-frequency spectroscopy of the water liquid/vapor interface. *Journal of Physical Chemistry B*, 113(13):4125–4130, 2009.

108. L. S. Jung, C. T. Campbell, T. M. Chinowsky, M. N. Mar, and S. S. Yee. Quantitative interpretation of the response of surface plasmon resonance sensors to adsorbed films. *Langmuir*, 14(19):5636–5648, 1998.

109. David J Griffiths. *Introduction to Electrodynamics*. Prentice Hall, NJ, Upper Saddle River, 3rd edition, 1999.

110. Marvin R Querry, David M Wieliczka, and David J Segelstein. *Handbook of Optical Constants of Solids*, volume 2. Academic Press, Waltham, MA, 1st edition, 1991.

111. M. R. Watry, T. L. Tarbuck, and G. I. Richmond. Vibrational sum-frequency studies of a series of phospholipid monolayers and the associated water structure at the vapor/water interface. *Journal of Physical Chemistry B*, 107(2):512–518, 2003.

112. K. Watanabe, K. Inoue, I. F. Nakai, and Y. Matsumoto. Nonadiabatic coupling between c-o stretching and pt substrate electrons enhanced by frustrated mode excitations. *Physical Review B*, 81(24):4, 2010.

113. J. I. Dadap, J. Shan, A. S. Weling, J. A. Misewich, and T. F. Heinz. Homodyne detection of second-harmonic generation as a probe of electric fields. *Applied Physics B-Lasers and Optics*, 68(3):333–341, 1999.

114. S. Mitragotri and J. Lahann. Physical approaches to biomaterial design. *Nature Materials*, 8(1):15–23, 2009.

115. J. A. Hubbell. Enhancing drug function. *Science*, 300(5619):595–596, 2003.

116. A. Nel, T. Xia, L. Madler, and N. Li. Toxic potential of materials at the nanolevel. *Science*, 311(5761):622–627, 2006.

117. A. Albanese, P. S. Tang, and W. C. W. Chan. *The Effect of Nanoparticle Size, Shape, and Surface Chemistry on Biological Systems*, volume 14 of *Annual Review of Biomedical Engineering*, pages 1–16. Annual Reviews, Palo Alto, 2012.

118. F. Rueckerl, J. A. Kaes, and C. Selle. Diffusion of nanoparticles in mono-layers is modulated by domain size. *Langmuir*, 24(7):3365–3369, 2008.

119. Hong Jin, Daniel A. Heller, Richa Sharma, and Michael S. Strano. Size-dependent cellular uptake and expulsion of single-walled carbon nan-otubes: Single particle tracking and a generic uptake model for nanopar-ticles. *Acs Nano*, 3(1):149–158, 2009.

120. L. F. Zhang and S. Granick. Dynamical heterogeneity in supported lipid bilayers. *Mrs Bulletin*, 31(7):527–531, 2006.

121. Y. Li and N. Gu. Thermodynamics of charged nanoparticle adsorption on charge-neutral membranes: A simulation study. *Journal of Physical Chemistry B*, 114(8):2749–2754, 2010.

122. G. Ma and H. C. Allen. Dppc langmuir monolayer at the air-water in-terface: Probing the tail and head groups by vibrational sum frequency generation spectroscopy. *Langmuir*, 22(12):5341–5349, 2006.

123. Bengt Kasemo. Biological surface science. *Surface Science*, 500(1-3):656–677, 2002.

124. J. A. Mondal, S. Nihonyanagi, S. Yamaguchi, and T. Tahara. Three dis-tinct water structures at a zwitterionic lipid/water interface revealed by heterodyne-detected vibrational sum frequency generation. *Journal of the American Chemical Society*, 134(18):7842–7850, 2012.

125. R. Wstneck, J. Perez-Gil, N. Wstneck, A. Cruz, V. B. Fainerman, and U. Pison. Interfacial properties of pulmonary surfactant layers. *Advances in Colloid and Interface Science*, 117(13):33–58, 2005.

126. Yi Y. Zuo, Ruud A. W. Veldhuizen, A. Wilhelm Neumann, Nils O. Pe-tersen, and Fred Possmayer. Current perspectives in pulmonary surfactant inhibition, enhancement and evaluation. *Biochimica et Biophysica Acta (BBA) - Biomembranes*, 1778(10):1947–1977, 2008.

127. D. Grillo, M. O. de la Cruz, and I. Szleifer. Theoretical studies of the phase behavior of dppc bilayers in the presence of macroions. *Soft Matter*, 7(10):4672–4679, 2011.

128. J. P. P. Ramalho, P. Gkeka, and L. Sarkisov. Structure and phase trans-formations of dppc lipid bilayers in the presence of nanoparticles: In-sights from coarse-grained molecular dynamics simulations. *Langmuir*, 27(7):3723–3730, 2011.

129. Chiranjeevi Peetla and Vinod Labhasetwar. Effect of molecular structure of cationic surfactants on biophysical interactions of surfactant-modified nanoparticles with a model membrane and cellular uptake. *Langmuir*, 25(4):2369–2377, 2009.

130. L. J. Zhang, A. Rozek, and R. E. W. Hancock. Interaction of cationic antimicrobial peptides with model membranes. *Journal of Biological Chemistry*, 276(38):35714–35722, 2001.

131. Alex G. F. de Beer and Sylvie Roke. Sum frequency generation scattering from the interface of an isotropic particle: Geometrical and chiral effects. *Physical Review B*, 75(24), 2007.

132. Mischa Bonn, Huib J. Bakker, Yujin Tong, and Ellen H. G. Backus. No ice-like water at aqueous biological interfaces. *Biointerphases*, 7(1-4), 2012.

133. J. C. Conboy, M. C. Messmer, and G. L. Richmond. Investigation of surfactant conformation and order at the liquid-liquid interface by total internal reflection sum-frequency vibrational spectroscopy. *Journal of Physical Chemistry*, 100(18):7617–7622, 1996.

134. V. A. Ermoshin, D. Bougeard, A. K. Kazanskii, and K. S. Smirnov. Fermi resonance between the vibrations of the hydrogen atom adsorbed at the (111) face of the diamond surface. *Optics and Spectroscopy*, 86(3):339–345, 1999.

135. Kailash C. Jena, Paul A. Covert, and Dennis K. Hore. The effect of salt on the water structure at a charged solid surface: Differentiating second- and third-order nonlinear contributions. *Journal of Physical Chemistry Letters*, 2(9):1056–1061, 2011.

136. A. G. F. de Beer, R. K. Campen, and S. Roke. Separating surface structure and surface charge with second-harmonic and sum-frequency scattering. *Physical Review B*, 82(23), 2010.

137. P. A. Gurnev and S. M. Bezrukov. Inversion of membrane surface charge by trivalent cations probed with a cation-selective channel. *Langmuir*, 28(45):15824–15830, 2012.

138. Anna Kubickova, Tomas Krizek, Pavel Coufal, Mario Vazdar, Erik Wernersson, Jan Heyda, and Pavel Jungwirth. Overcharging in biological systems: Reversal of electrophoretic mobility of aqueous polyaspartate by multivalent cations. *Physical Review Letters*, 108(18), 2012.

139. J. Pittler, W. Bu, D. Vaknin, A. Travesset, D. J. McGillivray, and M. Loesche. Charge inversion at minute electrolyte concentrations. *Physical Review Letters*, 97(4), 2006.

140. K. Besteman, K. Van Eijk, and S. G. Lemay. Charge inversion accompanies dna condensation by multivalent ions. *Nature Physics*, 3(9):641–644, 2007.

141. K. Besteman, M. A. G. Zevenbergen, H. A. Heering, and S. G. Lemay. Direct observation of charge inversion by multivalent ions as a universal electrostatic phenomenon. *Physical Review Letters*, 93(17), 2004.

142. P. Kekicheff, S. Marcelja, T. J. Senden, and V. E. Shubin. Charge reversal seen in electrical double-layer interaction of surfaces immersed in 2-1 calcium electrolyte. *Journal of Chemical Physics*, 99(8):6098–6113, 1993.

143. Jeannine Milhaud. New insights into waterphospholipid model membrane interactions. *Biochimica et Biophysica Acta (BBA) - Biomembranes*, 1663(12):19–51, 2004.

144. Siewert Jan Marrink, Max Berkowitz, and Herman J. C. Berendsen. Molecular dynamics simulation of a membrane/water interface: the ordering of water and its relation to the hydration force. *Langmuir*, 9(11):3122–3131, 1993.

145. Feng Zhou and Klaus Schulten. Molecular dynamics study of a membrane-water interface. *The Journal of Physical Chemistry*, 99(7):2194–2207, 1995.

146. Pl Jedlovszky and Mihaly Mezei. Orientational order of the water molecules across a fully hydrated dmpc bilayer: a monte carlo simulation study. *The Journal of Physical Chemistry B*, 105(17):3614–3623, 2001.

147. R. J. Mashl, H. L. Scott, S. Subramaniam, and E. Jakobsson. Molecular simulation of dioleoylphosphatidylcholine lipid bilayers at differing levels of hydration. *Biophysical Journal*, 81(6):3005–3015, 2001.

148. Xubo Lin, Changling Wang, Meng Wang, Kun Fang, and Ning Gu. Computer simulation of the effects of nanoparticles' adsorption on the properties of supported lipid bilayer. *Journal of Physical Chemistry C*, 116(33):17960–17968, 2012.

149. Seoktae Kang, Mathieu Pinault, Lisa D. Pfefferle, and Menachem Elimelech. Single-walled carbon nanotubes exhibit strong antimicrobial activity. *Langmuir*, 23(17):8670–8673, 2007.

150. N. W. S. Kam and H. J. Dai. Single walled carbon nanotubes for transport and delivery of biological cargos. *Physica Status Solidi B-Basic Solid State Physics*, 243(13):3561–3566, 2006.

151. S. R. Ji, C. Liu, B. Zhang, F. Yang, J. Xu, J. A. Long, C. Jin, D. L. Fu, Q. X. Ni, and X. J. Yu. Carbon nanotubes in cancer diagnosis and therapy. *Biochimica Et Biophysica Acta-Reviews on Cancer*, 1806(1):29–35, 2010.

152. A. Nimmagadda, K. Thurston, M. U. Nollert, and P. S. F. McFetridge. Chemical modification of swnt alters in vitro cell-swnt interactions. *Journal of Biomedical Materials Research Part A*, 76A(3):614–625, 2006.

153. N. W. S. Kam, M. O'Connell, J. A. Wisdom, and H. J. Dai. Carbon nanotubes as multifunctional biological transporters and near-infrared agents for selective cancer cell destruction. *Proceedings of the National Academy of Sciences of the United States of America*, 102(33):11600–11605, 2005.

154. Lin Sijie, G. Keskar, Y. Wu, Wang Xi, A. S. Mount, S. J. Klaine, J. M. Moore, A. M. Rao, and Ke Pu Chun. Detection of phospholipid-carbon nanotube translocation using fluorescence energy transfer. *Applied Physics Letters*, 89(14):143118–1–3, 2006.

155. D. Pantarotto, J. P. Briand, M. Prato, and A. Bianco. Translocation of bioactive peptides across cell membranes by carbon nanotubes. *Chemical Communications*, (1):16–17, 2004.

156. Yeonju Lee and Kurt E. Geckeler. Carbon nanotubes in the biological interphase: The relevance of noncovalence. *Advanced Materials*, 22(36):4076–4083, 2010.

157. Matthew L. Becker, Jeffrey A. Fagan, Nathan D. Gallant, Barry J. Bauer, Vardan Bajpai, Erik K. Hobbie, Silvia H. Lacerda, Kalman B. Migler, and John P. Jakupciak. Length-dependent uptake of dna-wrapped single-walled carbon nanotubes. *Advanced Materials*, 19(7):939–945, 2007.

158. T. Kirchhausen. Three ways to make a vesicle. *Nature Reviews Molecular Cell Biology*, 1(3):187–198, 2000.

159. S. Mukherjee, R. N. Ghosh, and F. R. Maxfield. Endocytosis. *Physiological Reviews*, 77(3):759–803, 1997.

160. Siegfried Hoefinger, Manuel Melle-Franco, Tommaso Gallo, Andrea Cantelli, Matteo Calvaresi, Jose A. N. F. Gomes, and Francesco Zerbetto. A computational analysis of the insertion of carbon nanotubes into cellular membranes. *Biomaterials*, 32(29):7079–7085, 2011.

161. P. Decuzzi and M. Ferrari. The role of specific and non-specific interactions in receptor-mediated endocytosis of nanoparticles. *Biomaterials*, 28(18):2915–2922, 2007.

162. D. Zhang, J. Gutow, and K. B. Eisenthal. Vibrational spectra, orientations, and phase transitions in long-chain amphiphiles at the air/water interface: Probing the head and tail groups by sum frequency generation. *Journal of Physical Chemistry*, 98(51):13729–13734.

163. Sylvie Roke, Juleon Schins, Michiel Mller, and Mischa Bonn. Vibrational spectroscopic investigation of the phase diagram of a biomimetic lipid monolayer. *Physical Review Letters*, 90(12):128101, 2003.

164. Tilman C. Hain, Kristin Kroeker, Dominik G. Stich, and Tobias Hertel. Influence of dna conformation on the dispersion of swnts: single-strand dna vs. hairpin dna. *Soft Matter*, 8(10):2820–2823, 2012.

165. M. Zheng, A. Jagota, E. D. Semke, B. A. Diner, R. S. McLean, S. R. Lustig, R. E. Richardson, and N. G. Tassi. Dna-assisted dispersion and separation of carbon nanotubes. *Nature Materials*, 2(5):338–342, 2003.

166. Maarten F. M. Engel, Lucie Khemtemourian, Cecile C. Kleijer, Hans J. D. Meeldijk, Jet Jacobs, Arie J. Verkleij, Ben de Kruijff, J. Antoinette Killian, and Jo W. M. Hoeppener. Membrane damage by human islet amyloid polypeptide through fibril growth at the membrane. *Proceedings of the National Academy of Sciences of the United States of America*, 105(16):6033–6038, 2008.

167. R.E. Pool, J. Versluis, E.H.G. Backus, and M. Bonn. Comparative study of direct and phase-specific vibrational sum-frequency generation spectroscopy: Advantages and limitations. *Journal of Physical Chemistry B*, 115(51):1536215369, 2011.

168. Fernando Albertorio, Mary E. Hughes, Jene A. Golovchenko, and Daniel Branton. Base dependent dna-carbon nanotube interactions: activation enthalpies and assembly-disassembly control. *Nanotechnology*, 20(39):395101–1–9, 2009.

169. A. E. McKiernan, T. V. Ratto, and M. L. Longo. Domain growth, shapes, and topology in cationic lipid bilayers on mica by fluorescence and atomic force microscopy. *Biophysical Journal*, 79(5):2605–2615, 2000.

170. D. Hoekstra. *Cell Lipids*. Academic Press, New York, 1994.

171. S. Hamann, J. F. Kiilgaard, T. Litman, F. J. Alvarez-Leefmans, B. R. Winther, and T. Zeuthen. Measurement of cell volume changes by fluorescence self-quenching. *Journal of Fluorescence*, 12(2):139–145, 2002.

Summary

Interfaces—the boundary surfaces and, as such, the interaction sites between materials—are of high interest in the scientific community. This fact may seem trivial, a straightforward consequence of their ubiquity in every regime of the physical world. This does not imply, however, that interfacial systems are easily studied. In many cases, the arrangement of atoms or molecules at an interface is different from that in the continuous 'bulk' material, and as a consequence processes unfold in a different way at interfaces than they would in the bulk. This distinctive interfacial region may be arbitrarily small, down to a single molecular or atomic layer in size. The observables of interfacial phenomena are thus at risk of being lost in their bulk background. For a thin water layer of one millimeter thickness, for example, only one in a million water molecules can be considered to be part of the interface.

In this thesis, several experiments are described to study interfacial systems by means of vibrational sum-frequency generation (SFG) spectroscopy. This technique makes use of an infrared (IR) laser source to excite the vibrational modes of a molecule. A second laser beam, typically of near-infrared frequency and not resonant with any optical transition in the sample, is combined with the IR beam to create an SFG signal with a frequency equal to the sum of the two incident beams. The main advantage that SFG has over traditional IR or Raman techniques in the study of interfaces is its surface specificity. Being a two-photon process, the generation of the sum-frequency signal only occurs in materials that have a broken symmetry. For most materials, symmetry is only broken at the interface, making SFG an ideal tool to focus on just the interfacial properties.

In the first three chapters of this thesis, the theoretical and experimental background of SFG spectroscopy is described, starting with a historical overview of its development. In this overview a range of possible applications was presented, leading to the introduction of the lipid interfaces that are central to the experiments described in the last three chapters of this work. Chapter 1 continues by describing how the spectral information of an SFG measurement can be used to obtain insight into the molecular structure of the interfacial system.

Chapter 2 provides a selection of the physical principles that are fundamental to the occurrence of the sum-frequency signal. This theoretical context is presented to provide the reader with a better understanding of the possibilities and limitations of SFG spectroscopy. From the theoretical description of the SFG response we move on to discuss the model that is used to perform quantitative analysis of the SFG data.

The experimental setup is described in chapter 3, highlighting the princi-

ple of IR generation through optical parametric amplification and providing a description the of sample preparation protocol.

Isotopic dilution at the air-water interface. The first experiment described in this thesis explores the most common aqueous interface, that between pure water and air. The SFG spectrum of this interface consists of two spectral features: a broad peak associated with the hydrogen-bonded water, behaving much like bulk water, and a narrow feature at higher frequency arising from OH bonds sticking into the air. Since these bonds are not hydrogen bonded, we often refer to them as the 'free OH'.

In the introduction we mentioned that it is common practice to replace water (H_2O) by heavy water (D_2O) to move the water's resonances into a more accessible spectral region. When doing so, it is assumed that the molecular organization and superstructure within the sample is not affected by this exchange. Chapter 4 shows that calculations that include the quantum mechanical properties of H_2O and D_2O indicate that this assumption is not correct: when mixing water and heavy water, significantly more free OH bonds exist than free OD bonds. This prediction is derived from path integral calculations that describe the effect of the uncertainty principle for the position of an atom on the trajectory that it describes. The D atom, being significantly heavier than the H atom, has a more well-defined position. The calculations indicate that this localization effect results in stronger hydrogen-bonding of the D atom than of the H atom. Because of this asymmetry, an HOD molecule at the interface will have a higher probability to be hydrogen-bonded to the D atom and having a free OH bond than vice versa.

This theoretical prediction is confirmed experimentally by recording the SFG spectra of a range of isotopic mixtures of H_2O and D_2O in both the OH and OD spectral region and carefully fitting the data. The ratio between free OH and free OD formation is in quantitative agreement with the calculated values, indicating a difference of up to 10%.

Comparison of direct and phase-sensitive SFG spectroscopy. After this look into the fundamental behavior of the deuterated water interface, we proceed with a discussion of a technical aspect of SFG spectroscopy. In recent years, several groups have implemented an interference-based ('heterodyning') technique to extract the absolute sign of the resonances featured in the SFG spectrum. Whereas in a typical, direct SFG measurement the squared electric field is detected, interference with a nonresonant reference medium introduces linear terms in the SFG signal intensity that can have both positive and negative spectral features. This sign, or *phase* of the complex signal indicates if the molecular bond that it originates from is pointing up or down, and thus provides additional insight into the molecular structure of the studied interfacial system. Chapter 5 provides a thorough theoretical description of the methodology of this phase-sensitive SFG (PS-SFG), deriving the mathematical principles that it is based upon and acting as a step-by-step guide for data analysis. As a case study the water below monolayers constituted of the negatively charged

phospholipid DMPS and the positively charged lipid DPTAP is probed by both traditional (direct) SFG and PS-SFG. The sign of the detected PS-SFG water signal is positive for DMPS and negative for DPTAP, corresponding to the expected alignment of the water dipole along the interfacial electrostatic field. We show that to compare the PS-SFG spectrum to the direct SFG measurement one need not only square the signal, but also correct it for the IR radiation lost when reflecting off the sample surface. By considering the complex refractive index of the sample, in this case approximating it by that of just heavy water, we were able to neatly overlap our direct and PS-SFG data. This quantitative comparability supports a better understanding of PS-SFG, a field of research that is both powerful and growing in application, but still contains uncertainties and would benefit from more standardization across scientific groups.

Chapter 5 is concluded by a comparison of the signal-to-noise (SNR) ratio that is achievable with direct SFG and PS-SFG techniques. We present a simple analysis to show that PS-SFG has a higher sensitivity, giving a better SNR for very weak signals, but performs equally to or slightly worse than direct SFG for high signal intensities.

THE INTERACTION OF CHARGED LATEX NANOPARTICLES WITH A MODEL MEM-BRANE. In chapter 6, the interaction of nanoparticles (NPs) with a model membrane is studied by tracking the changes induced in the SFG spectrum. As a model membrane, monolayers consisting of phospholipids with only positive, negative or zwitterionic charges in their head groups were chosen. The NPs were 30 nm polystyrene latex spheres functionalized with either positive or negative charge groups.

The interaction between NPs and the lipid monolayer is clearly identifiable with SFG spectroscopy through changes in the spectral features of the OD and CH stretch vibrations of (heavy) water and lipids, respectively. The spectral changes induced by adding charged NPs to monolayers of opposite charge are significant, while equal charged NPs and monolayers show only minor effects. This result indicates, in agreement with intuition, that the interaction is dominated by electrostatics. Scanning electron microscopy (SEM) images of the deposited system confirmed this finding: a high density of NPs (> 100 per μm^2) was found for the oppositely charged NP/monolayer combination, and almost none (< 1 per μm^2) for equal charges. From the SFG data, details of the molecular superstructure at the interaction site could be deduced. Negative NPs are shown to bind tightly to the positively charged (DPTAP) monolayer so effectively that charge inversion occurs, as can be observed by a phase change of the water signal. Binding is accompanied by an increase in alkyl chain order. The system with charges reversed, positive NPs binding to negatively charged (DPPG) monolayers, looks very similar in the SEM images. The SFG spectra, however, reveal several interesting differences: the binding of the positive NPs to a negative monolayer induces neither charge inversion nor an increase in alkyl chain order. An explanation for both these differences is presented based on how the lipids' chemical structure may influence the interfacial molecular organization.

Both positively and negatively charged NPs were observed to interact with a zwitterionic phospholipid (DPPC) monolayer. Although the monolayer has no net charge, the dipole consisting of the two charges in the lipids head group aligns the interfacial water. All changes in the SFG spectra induced by the charged NPs could be ascribed to changes in the angle of the dipolar head group with respect to the surface. All in all, a coherent interpretation of the SFG spectra is formulated for each of the six NP-lipid combinations.

The interaction of DNA-covered single-walled carbon nanotubes with a model membrane. In chapter 7, we continue with the study of another synthetic nanomaterial interacting with lipid monolayers. Here, we examine single-wall carbon nanotubes (SWNTs), made soluble in an aqueous environment by the addition of short strands of DNA. These DNA-SWNT complexes are of interest as candidate carriers for drug delivery, and as such knowledge of the nature of their interaction with the lipids of the cell membrane is important.

Through a combination of tensiometry and SFG spectroscopy we were able to observe the nonspecific interaction between lipid monolayers and DNA-SWNTs. We identify two separate stages in the interaction dynamics: in the first stage, the nanotubes bind to the lipid monolayer electrostatically, mediated by the DNA molecules, and in doing so change the interfacial water structure, as can been deduced from spectral changes in the SFG water signal. In the second stage, part of the nanotube's surface is bared of DNA and embedded into the hydrophobic region of the monolayer, reflected in changes in the lipid alkyl chain organization.

A binding and dissociation model previously developed for endocytosis was used to fit the time dependence of our data. This model is able to accurately reproduce the observed dynamics of the two stages, revealing that the time constants of this nonspecific process are similar to those observed for endocytosis. From this parallel, we conclude that cell-level observations may not distinguish between different cell entry mechanisms, while different molecular pathways may lead to comparable emergent macroscopic states. The strong SWNT-monolayer interaction observed in SFG spectroscopy and tensiometry suggests that the SWNTs may severely disrupt and damage a lipid-based membrane. Nevertheless, vesicle leakage experiments reveal no rupture of the lipid membranes of vesicles in the presence of SWNTs.

This chapter, by providing a combination of fitted SFG data and a model describing the dynamics observed there, introduces a quantitative way of looking at the nonspecific interactions between SWNTs and highly simplified model membranes. Such a controllable experimental approach has the potential to serve as a bridge between molecular dynamics simulations, which tend to be remote from experimental approaches due to necessary oversimplification, and in vivo systems, which tend to be too complex to allow for quantitative understanding of the observed phenomena.

Samenvatting

Met de Engelse term 'interfaces' uit de titel van dit proefschrift worden de oppervlakken bedoeld die de raakvlakken vormen tussen verschillende materialen. Omdat het aan deze raakvlakken is dat reacties en interacties plaatsvinden, zijn zij van groot belang in de wetenschappelijke gemeenschap. Dit feit lijkt misschien triviaal, een eenvoudig gevolg van hun alomtegenwoordigheid: raakvlakken vinden we tenslotte overal. Dit betekent echter niet dat grensvlaksystemen gemakkelijk te begrijpen zijn. In veel gevallen is de rangschikking van atomen of moleculen aan een oppervlak anders dan in de continue masse van het materiaal, waardoor fysische en chemische processen zich op een andere manier ontvouwen aan grensvlakken dan in de massa. Dit afwijkende grensvlakgebied kan extreem klein zijn, tot een enkele moleculaire of atomaire laag groot. De observabelen van fenomenen aan deze oppervlakken lopen hierdoor het risico verloren te gaan de achtergrond van de grote massa. Om een voorbeeld te geven: zelfs in een dunne waterlaag van een millimeter dikte kan maar één op een miljoen watermoleculen worden beschouwd als deel van het wateroppervlak.

In dit proefschrift worden verschillende experimenten beschreven die de moleculaire vibraties aan grensvlaksystemen bestuderen door middel van sumfrequenty generation (SFG) spectroscopie. Deze techniek maakt gebruik van een infrarode (IR) laserbron die de trillingtoestanden van moleculen aanslaat. Een tweede laserbundel, typisch van een nabije IR-frequentie en niet resonant met enige optische overgang in het monster, wordt gecombineerd met de IR-straal om zo een SFG-signaal te creren met een frequentie gelijk aan de som van de twee invallende bundels. Het belangrijkste voordeel van SFG spectroscopie bij de studie van raakvlakken ten opzichte van traditionele IR- of Raman-technieken is de oppervlaktespecificiteit. Omdat SFG een twee-foton proces is kan het SFG-signaal alleen ontstaan in materialen met een gebroken symmetrie. Voor de meeste materialen geldt dat symmetrie alleen gebroken wordt aan het grensvlak, waardoor SFG-spectroscopie een ideale techniek voor onderzoek dat specifiek is gericht op de grensvlakeigenschappen.

In de eerste drie hoofdstukken van dit proefschrift wordt de theoretische en experimentele achtergrond van SFG-spectroscopie beschreven, te beginnen met een historisch overzicht van de ontwikkeling ervan. In dit overzicht worden mogelijke toepassingen gepresenteerd, en wordt de nadruk gelegd op de lipidelagen die centraal staan in de experimenten die beschreven worden in de laatste drie hoofdstukken van dit werk. In hoofdstuk 1 wordt vervolgens uitgelegd hoe de spectrale informatie van een SFG-meting gebruikt kan worden om inzicht te krijgen in de moleculaire structuur van het grensvlaksysteem.

Hoofdstuk 2 geeft een selectie van de fysische principes die ten grondslag liggen aan het ontstaan van het SFG-signaal. Deze theoretische context dient om de lezer meer begrip te bieden over de mogelijkheden en beperkingen van SFG-spectroscopie. Vanuit deze theoretische beschrijving van SFG introduceren we het model dat wordt gebruikt voor de kwantitatieve analyse van het SFG-signaal.

De experimentele opstelling wordt beschreven in hoofdstuk 3, waarbij de nadruk ligt op het opwekken van IR-straling door middel van een optische parametrische versterker. Ook wordt de procedure van de preparatie van het monster omschreven.

Isotope verdunning aan het lucht/water-oppervlak. Het eerste experiment dat beschreven staat in dit proefschrift verkent één van de meest voorkomende oppervlakken ter wereld, dat tussen zuiver water en lucht. Het SFG-spectrum van het wateroppervlak bevat twee spectrale kenmerken: een brede piek ten gevolge van het waterstofgebonden water, dat zich gedraagt als water in de massa, en een smalle piek bij een hogere frequentie, die voortkomt uit OH-verbindingen die de lucht in steken. Omdat deze verbindingen niet waterstofgebonden zijn noemen we ze ook wel de 'vrije OH'.

In de inleiding hebben we al eens genoemd dat het gebruikelijk is om water (H_2O) te vervangen door zwaar water (D_2O) om resonanties te verplaatsen naar een meer toegankelijk spectraal gebied. Daarbij wordt aangenomen dat de moleculaire organisatie en opbouw aan het wateroppervlak niet wordt beïnvloed door deze vervanging. Hoofdstuk 4 laat zien dat berekeningen die de kwantum-mechanische eigenschappen van H_2O en D_2O in overweging nemen aangeven dat deze veronderstelling niet juist is: wanneer we water en zwaar water mengen blijkt er aanzienlijk meer vrije OH voor te komen dan vrije OD. Deze voorspelling is afgeleid uit berekeningen van de 'padintegraal' die het effect van het onzekerheidsbeginsel op het traject van een atoom beschrijven. Het D-atoom, dat beduidend zwaarder is dan het H-atoom, heeft een goed gedefinieerde positie. De berekeningen geven aan dat dit lokalisatie-effect zorgt voor een sterkere 'waterstof'-binding van het D-atoom dan van het H-atoom. Door deze asymmetrie zal een HOD-molecuul aan het wateroppervlak een grotere kans hebben om waterstofgebonden te zijn aan het D-atoom en een vrije OH-verbinding te hebben dan vice versa.

Deze theoretische voorspelling wordt experimenteel bevestigd door het meten van de SFG-spectra van verschillende isotoop verdunde mengsels van H_2O en D_2O in het spectrale gebied van zowel de vrije OH als de vrije OD, en deze gegevens zorgvuldig te modelleren. De verhouding tussen de gemeten vrije OH en vrije OD komt kwantitatief overeen met de berekende waarden, waarbij deze verschillen opliepen tot maximaal 10%.

Een vergelijking van directe en fasegevoelige SFG-spectroscopie. Na deze blik op het fundamentele gedrag van (zware) wateroppervlak gaan door we met het bespreken van een technisch aspect van SFG-spectroscopie. Gedurende de laatste jaren hebben verschillende groepen gebruik gemaakt van

een ('heterodyne') interferentietechniek om het absolute teken van de reso-
nanties in het SFG-spectrum te vinden. Een beperking van traditionele, di-
recte SFG-metingen is dat het kwadraat van het SFG-veld wordt gedetecteerd,
waardoor het teken van het signaal verloren gaat. Met de nieuwe methodiek
introduceert interferentie met een niet-resonant referentiemedium lineaire ter-
men in het SFG-intensiteitssignaal die zowel positieve als negatieve spectrale
kenmerken kunnen vertonen. Dit teken, ook wel de 'fase' van het complexe sig-
naal genoemd, geeft aan of de moleculaire binding waarvandaan het afkomstig
is omhoog of omlaag wijst, en biedt daarmee extra inzicht in de moleculaire
structuur van het bestudeerde oppervlak. Hoofdstuk 5 geeft een grondige the-
oretische beschrijving van de methodologie van deze fase-gevoelige SFG (PS-
SFG) door de wiskundige principes waarop zij is gebaseerd af te leiden. Tevens
is het hoofdstuk te gebruiken als handleiding die stap voor stap de aanpak van
analyse van de PS-SFG-data omschrijft. Als praktisch voorbeeld wordt het wa-
ter onder monolagen van de negatief geladen fosfolipide DMPS en de positief
geladen lipide DPTAP bestudeerd met zowel traditionele (directe) SFG en PS-
SFG. Het teken van het gedetecteerde PS-SFG water signaal is positief voor
DMPS en negatief voor DPTAP, overeenkomend met de verwachte oriëntatie
die de dipool van het water aanneemt door toedoen van het elektrisch veld onder
de monolaag.

We laten zien dat wanneer men het PS-SFG-spectrum gelijk wil maken aan
de directe SFG-meting het niet voldoende is om het signaal te kwadrateren,
maar dat er ook een correctie moet worden toegepast voor de IR-straling die
verloren gaat bij reflectie vanaf het oppervlak van het monster. Door rekening te
houden met de complexe brekingsindex van het monster, in dit geval benaderd
het door die van zwaar water, waren we in staat om onze directe en PS-SFG data
nauwkeurig te laten overlappen. Deze kwantitatieve vergelijkbaarheid helpt bij
het beter begrijpen van PS-SFG, een onderzoeksgebied dat veel potentieel heeft
en steeds meer wordt toegepast, maar nog altijd onzekerheden bevat en baat
zou hebben bij het invoeren van meer standaardisatie onder de verschillende
wetenschappelijke groepen.

Hoofdstuk 5 wordt afgesloten met een vergelijking van de signaal-
ruisverhouding die kan worden bereikt met directe en PS-SFG. We presenteren
een eenvoudige analyse waaruit blijkt dat PS-SFG een hogere gevoeligheid
heeft, waardoor een betere signaal-ruisverhouding kan worden verkregen voor
zeer zwakke signalen, maar dat het iets slechter dan directe SFG presteert voor
hoge signaalintensiteiten.

DE INTERACTIE VAN GELADEN LATEX NANODEELTJES MET EEN MODELMEM-
BRAAN. In hoofdstuk 6 bespreken we de interactie van nanodeeltjes (NPs) met
een modelmembraan, bestudeerd door het volgen van de veranderingen die het
injecteren van de NPs teweegbrengt in het SFG-spectrum. Als modelmembraan
werden monolagen van fosfolipiden met enkel positieve, negatieve of zwitter-
ionische lading in hun kopgroepen gekozen. De NPs waren 30 nm polystyreen
latex bolletjes gefunctionaliseerd met positieve of negatieve ladingsgroepen.

De interactie tussen deze NPs en de lipide monolaag is duidelijk te identi-

ficeren met SFG spectroscopie door middel van veranderingen in de spectrale kenmerken van de OD en CH strek vibraties van respectievelijk (zwaar) water en lipiden. De spectrale veranderingen die worden veroorzaakt door het toevoegen van NPs aan monolagen van tegengestelde lading zijn significant, terwijl gelijk geladen NPs en monolagen slechts geringe effecten vertonen. Dit resultaat geeft aan dat de interactie wordt gedomineerd door elektrostatica. Beelden verkregen met scanning-elektronenmicroscopie (SEM) van het op goud gedeponeerde systeem bevestigen dit: een hoge dichtheid NPs (> 100 per μm^2) werd gevonden voor de tegengesteld geladen NP/monolaag combinatie, en bijna geen deeltjes (<1 per μm^2) voor gelijke ladingen. Uit de SFG-data kunnen we de moleculaire structuur rond de interactieplaats afleiden. Negatieve NPs bleken zo nauw en zo massaal te binden aan de positief geladen (DPTAP) lipiden dat er ladinginversie optreedt, zoals kan worden waargenomen door een faseverandering van het watersignaal. Dit binden gaat gepaard met een toename van de geordendheid van de hydrofobe alkylketens van de lipiden. Het systeem met de tegenovergestelde ladingen, positieve NPs met negatief geladen (DPPG) monolagen, lijkt in de SEM-afbeeldingen erg op negatieve NPs met DPTAP. In de SFG-spectra zie we echter een paar interessante verschillen: de binding van de positieve NPs aan een negatieve monolaag leidt niet tot ladinginversie, noch tot een toename in de geordendheid van de alkylketens. Er wordt een verklaring voor beide verschillen gepresenteerd op basis van de chemische structuur van de lipiden, waarbij we beredeneren hoe deze structuur de moleculaire organisatie aan het oppervlak zou kunnen beïnvloeden.

Voor zowel positief als negatief geladen NPs wordt een interactie waargenomen met een zwitterionisch geladen fosfolipide (DPPC) monolaag. Hoewel de monolaag geen netto lading heeft zorgt de dipool gevormd door de twee ladingen in de kopgroep van de lipiden ervoor dat het omringende water zich ordent. Alle veranderingen die we observeren in de SFG-spectra na injectie van de geladen NPs kunnen worden toegeschreven aan variaties in de hoek die de dipolaire kopgroep maakt met het oppervlak. Het hoofdstuk wordt afgesloten met een coherente interpretatie van de SFG-spectra voor elk van de zes NP-lipidecombinaties.

DE INTERACTIE VAN MET DNA BEDEKTE ENKELWANDIGE KOOLSTOF-NANOBUIZEN MET EEN MODELMEMBRAAN. In hoofdstuk 7 bestuderen we de interactie van een ander synthetisch nanomateriaal met lipide monolagen. Hier onderzoeken wij enkelwandige koolstofnanobuizen (SWNTs), oplosbaar gemaakt in water door de toevoeging van korte DNA-strengen. Deze DNA-SWNT complexen zouden goede dragers van geneesmiddelen kunnen zijn voor de plaatselijke afgifte ervan in zieke cellen. Om ze effectief toe te passen in deze functie is kennis van de aard van hun interactie met de lipiden van het celmembraan essentieel.

Door een combinatie van tensiometrie en SFG-spectroscopie waren we in staat om de niet-specifieke interactie tussen een lipide monolaag en DNA-SWNTs te observeren. We identificeren twee verschillende fasen in het verloop van de interactie: in de eerste fase binden de nanobuisjes aan de lipide mono-

laag via het negatief geladen DNA, dat electrostatisch wordt aangetrokken tot de positief geladen (DPTAP) lipidelaag. De aanwezigheid van de DNA-SWNTs beïnvloedt de waterstructuur aan het oppervlak, zoals afgeleid kan worden uit veranderingen in het SFG-spectrum. In de tweede fase verdwijnt een deel van het DNA van het oppervlak van de nanobuizen, waardoor de buizen zich kunnen nestelen tussen de hydrofobe alkylketens in de monolaag. Dit is te zien in de SFG-spectra aan veranderingen in de CH-resonanties.

Een eerder ontwikkeld bindings- en dissociatiemodel wordt gebruikt om de tijdsafhankelijkheid van onze data te omschrijven. Dit model is in staat om de waargenomen twee fasen uit onze data nauwkeurig weer te geven, waaruit blijkt dat de tijdconstanten van dit niet-specifieke proces vergelijkbaar zijn met die van endocytose. Uit deze overeenkomst concluderen we dat waarnemingen op celniveau niet altijd uitsluitsel kunnen geven over het mechanisme van opname in de cel, terwijl verschillende moleculaire mechanismen kunnen leiden tot het ontstaan van vergelijkbare macroscopische toestanden. De sterke interactie tussen SWNTs en monolaag die we waarnemen met SFG-spectroscopie en tensiometrie doet vermoeden dat de SWNTs het membraan misschien beschadigen. Toch bleek uit experimenten met vesikelen geen lekkage te ontstaan na binding van de SWNTs aan het vesikelmembraan.

Door middel van een combinatie van SFG-spectroscopie en een model dat de spectrale informatie omschrijft, introduceert dit hoofdstuk een kwantitatieve manier van kijken naar de niet-specifieke interacties tussen SWNTs en sterk vereenvoudigde modelmembranen. Een dergelijke, beheersbare experimentele benadering kan dienen als een brug tussen simulaties van moleculaire dynamica, die vaak niet te rijmen zijn met experimentele benaderingen door noodzakelijke oversimplificatie, en in vivo systemen, die vaak te ingewikkeld zijn voor kwantitatief begrip van de waargenomen verschijnselen.

Acknowledgements

we'll keep in touch! The same goes for all the great people I have worked with in the PV: Michel, Ernst Jan, James, Tomek, Wiet, Ioana and Sarah.

There are and were many more who I would like to thank for their help and good company. In random and chaotic order: Alex (the best German Zwarte Piet ever), Simon, Huib, Sietse, Simona, Klaas-Jan, Lukasz, Stephan, Yves, Avi, Maaike, James, Lutz, Wing Kiu, Ymkje, Marjon, Nienke, Megan, Gijs, Ivana, Rutger, Christian, Mohamed, Marjolein, Grace, Chris, Andrej, Nuria, Sophie and Felipe.

Een zeer belangrijk onderdeel van het plezier en succes had ik bij AMOLF had werd mogelijk gemaakt door de uitstekende steun van de werkplaats, de tekenkamer, de ICT- en electronika-afdeling, en de vriendelijke en behulpzame mensen bij de administratie, receptie, bibliotheek, kantine en het magazijn. Het is niet alleen heel prettig om zoveel hulp te krijgen, maar ook heel motiverend om te weten dat zulke capabele en aardige mensen hun best voor je doen.

Next, I would like to thank my wonderful colleagues at the Max Planck Institute for Polymer Research in Mainz. Alejandra, for all the fun, her good taste in music and for letting me stay at the Michael-Müller-Ring after she moved in. The same goes for Zoltan. I will never forget his gentle craziness and interesting knowledge of food and martial arts. Then there are the others that made me feel more at home in Mainz: Hai, Francesco, Ravindra, Johannes, Will, Kamila, Maria, Ruth, Samet, Vasileios and Masanari, I enjoyed our lunches, drinks and adventures. At the institute, I enjoyed conversations with Johannes, Lars, Michael, Denise, Erik, Tobias, Joe, Dan, Sapun, Dimitry, Zhen, Victor, Charlotte, Bernhard and Christoph.

In the shady region that overlaps both my professional and my private life we find Tibert and Steven, my dearly appreciated paranymphs. I would like to thank Tibert for making my master studies and my PhD much more enjoyable, for his sensible opinions and advice, and simply for the good times we've had. Steven was a great help getting to know and to enjoy AMOLF; I remember feeling like naughty children walking through the old AMOLF building together looking for new things to discover and new people to meet.

There are many others that I am thankful to. My friends from school, Attila, Eylard, Guido, Jannes, and Rogier, who have proven time and time again that I will never get rid of them. My magical friends Erik Seyferth and Hans van Schie, my former band members Jason and Marc, my 'oldest' friend Benno, Susanne, Daan, TThomas, Nikki, Tonnie, Jan-Willem, Floor & Evelien, my former flat mates Sebastian, Alberto and Anne, and my cousin Gemma.

Ik wil graag mijn lieve ouders, Frouwke en Eric, mijn zus Renske, en mijn oma bedanken voor de warme ontvangst die zij me altijd bieden als ik langskom. Wanneer ik gestrest was verdween dat als sneeuw voor de zon na een avond met een van hun heerlijke maaltijden, Renske's gezellige geklets, koffie, en goede gesprekken.

Ten slot wil ik mijn lieve vriendin Gusta bedanken voor van alles, veel te veel om op te noemen.